

The Effects of Local Structure on Thermal Transport in Carbon Nanotube Networks

A Dissertation

Presented to
the faculty of the School of Engineering and Applied Science
University of Virginia

in partial fulfillment
of the requirements for the degree

Doctor of Philosophy

by

Richard N. Salaway

August

2014

APPROVAL SHEET

The dissertation
is submitted in partial fulfillment of the requirements
for the degree of
Doctor of Philosophy


AUTHOR

The dissertation has been read and approved by the examining committee:

Dr. Leonid Zhigilei

Advisor

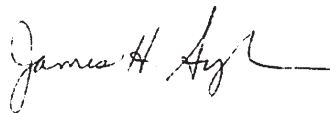
Dr. Pamela Norris

Dr. Patrick Hopkins

Dr. Harsha Chelliah

Dr. Mikail Povarnitsyn

Accepted for the School of Engineering and Applied Science:



Dean, School of Engineering and Applied Science

August
2014

Abstract

Carbon nanotubes (CNTs) have gained a significant amount of research interest for use in thermal management applications. Measurements have shown an exceptionally high intrinsic thermal conductivity, k , of individual CNTs. However, when the CNTs are formed into structures or incorporated into a polymer matrix, the collective thermal conductivity through the CNT network or nanocomposite material is found to be orders of magnitude lower than the conductivity of the constituent CNTs. Two major factors may be responsible for the low conductivity of the CNT structures: the reduction of the intrinsic conductivity of individual CNTs due to inter-tube interactions, and low thermal conductance at CNT-CNT contacts that may be sensitive to the surrounding environment.

To investigate the effects of local structure on the intrinsic conductivity of individual CNTs and the thermal conductance across CNT-CNT interfaces, non-equilibrium molecular dynamics (MD) simulations are performed for different parameters of CNT junctions (e.g., contact area, contact angle, etc.) and local structural environments characteristic of CNT network materials (e.g., CNT length, distance to nearest neighboring junction, etc.). The results of MD simulations suggest that (1) contrary to the widespread notion of strongly reduced conductivity of individual CNTs in bundles as compared to the conductivity of isolated CNTs, the van der Waals interactions between defect-free well-aligned CNTs in a bundle have negligible effect on the intrinsic conductivity of the CNTs, (2) the effect of neighboring junctions on the conductance at CNT-CNT junctions is weak and only present when the junction separation distance is within the range of direct van der Waals interactions, (3) the conductance through the overlap region between neighboring parallel

CNTs is linearly dependent on the length of the overlap for CNTs and CNT-CNT overlaps longer than several tens of nanometers, and (4) the linear dependence of conductance on the overlap area is found to break down for non-parallel configurations with small contact areas.

In addition, the effect of variation in parameters of MD simulations (e.g., interatomic potential, thermal bath region length, etc.) on the prediction of CNT thermal properties is systematically investigated. Discrepancy in non-equilibrium MD predictions of CNT conductivity found in the literature is shown to be partially caused by erroneous assumptions about how conductivity is affected by the location and length of the regions where the thermal flux is imparted. A more accurate convention for defining the configuration of the computational cell is presented. Based on the results of the MD simulations, a general description of the conductance at CNT-CNT contacts is designed for an arbitrary configuration. Agreement in predicted values of CNT-CNT conductance between this general model and MD simulations is demonstrated. Overall, the results presented here help elucidate the sensitivity of the intrinsic CNT conductivity and CNT-CNT conductance to structural parameters which are relevant for the optimization of the thermal performance of CNT materials.

Acknowledgments

I am extremely grateful for the assistance, mentoring, and example provided by my co-advisor, Dr. Leonid Zhigilei. His impressive combination of intellect, drive, and patience is humbling. He is truly a mentor to each member of a large research group, overseeing a broad range of research topics. Many times I have been amazed to visit his office for the first time in many weeks and find that not only can he remember exactly where we left off before, but that he can also recite from memory a list of publications I should review to address the new issue I am facing. His tenacious commitment to the scientific method is exceptional. By his patient and pragmatic approach, I have learned to be the most critical reviewer of my own work. I believe his mentorship has made me a better scholar as well as a better thinker.

I would also like to offer my sincere gratitude to my co-advisor Dr. Pamela Norris. Dr. Norris is largely to thank for my returning to UVa for a PhD. I am not sure how serious she was when she made the suggestion in passing, but I know how committed she became when I took her up on it months later. Fitting of her personality, I was confused by her offer to assist me academically and/or financially even before her formal role was determined. I will always be grateful for her trust, encouragement, and guidance. Dr. Norris has the unique ability to treat every student both as a scholar and as a human being. I am grateful for both the professional and the personal examples she has set for me. They, no doubt, will continue to shape my career.

I am very grateful to the members of my dissertation committee; Dr. Patrick Hopkins, Dr. Harsha Chelliah, and Dr. Mikail Povarnitsyn. I had the honor of working with Dr.

Hopkins while he was a graduate student at UVa. I am thankful for the example he has set. His deep expertise and patience has helped me throughout my graduate career. I value his guidance almost as much as I value his friendship. Dr. Chelliah has taught me much about thermomechanics through courses and discussion. His challenging inquiries have given me a deeper appreciation for the complexities of nanoscale heat transfer. Dr. Povarnitsyn was very kind in agreeing to be on my committee during his short visit to UVa. I am thankful for the insightful comments he offered, despite having such little time available.

I would like to thank all former fellow lab members with whom I have had the privilege to work. In particular, I would like to thank Dr. Alexey Volkov and Dr. John Duda. Dr. Volkov has been an inexhaustible source of knowledge. His guidance and attention to detail significantly facilitated my acclimation to a new area of research. Dr. Duda's extensive understanding and patience have been evident in his assistance. His expertise in the more specialized areas of my research has proven beneficial many times. His support of a friend has been invaluable. I would also like to thank all my current fellow lab members; Dr. Chengping Wu, Eaman Karim, Marshall Tabetah, Bernard Wittmaack, Cheng-Yu Shih, Maxim Shugayev, Miao He, and Anna Greene. I greatly appreciate the positive, scholarly, and supportive environment created in the lab by the efforts of each member.

Like most, I have had successes and failures, often confusing one for the other. Through them all there has been one constant. A steady beacon I run around while chasing things. Silently reminding me of the beginning. The three of us there, eating dinner on a card table. I am more than grateful to have been introduced to this world by the two of you. And I am more than grateful for my sister, who brought family to me when I couldn't be with family. You made a tough transition easy, and turned a beautiful state into home. To my wife, what can I say? You are the words that have allowed me to write this document. And yes, words are fine for expressing concepts such as these which this work contains. Here I offer a few insufficient words of gratitude. The rest will have to be expressed through our life together. 5 ways.

Contents

List of Figures	ix
List of Tables	x
Nomenclature	xi
1 Introduction	1
1.1 Motivation	1
1.1.1 Thermal Applications of CNT-based Materials	4
1.1.2 Molecular Dynamics Simulations	5
1.2 Objectives and Outline	6
2 Molecular Dynamics Simulations	9
2.1 Background	9
2.2 Interatomic Potentials	10
2.2.1 Lennard-Jones Potential	11
2.2.2 Tersoff Potential	13
2.2.3 Brenner-II Potential	14
2.3 LAMMPS	15
3 CNT Thermal Conductivity	17
3.1 Background	17
3.1.1 Background on the Effect of CNT Length	19
3.1.2 Background on the Effect of Atomistic Simulation Parameters	21
3.1.3 Background on the Effect of Inter-Tube Interactions in Bundles	24
3.2 Computational Results	26
3.2.1 General Computational Procedure	26
3.2.2 Effect of CNT Length	30
3.2.3 Effect of Atomistic Simulation Parameters	32
3.2.3.1 Heat Bath Length	32
3.2.3.2 Computational Configuration	41
3.2.3.3 Interatomic Potential	44
3.2.4 Effect of Inter-Tube Interactions in Bundles	47
3.3 Summary	50

4	CNT-CNT Thermal Conductance	53
4.1	Background	53
4.1.1	Background on the Effect of CNT Length	54
4.1.2	Background on the Effect of Contact Density	56
4.1.3	Background on the Effect of Contact Area	58
4.2	Computational Results	59
4.2.1	Effect of CNT Length	60
4.2.2	Effect of Contact Density	66
4.2.3	Effect of Contact Area between Parallel CNTs	69
4.2.4	CNT-CNT Contacts of Arbitrary Configuration	75
4.3	Summary	85
5	Thermal Conductance between Two-Dimensional Lennard-Jones Materials	87
5.1	Background	87
5.2	General Computational Procedure	88
5.3	Computational Results	93
5.3.1	Effect of Temperature	93
5.3.2	Effect of Density of Interatomic Interfacial Interactions	95
5.3.3	Effect of Interaction Energy	100
5.3.4	Analysis of Vibrational Spectrum	102
5.4	Summary	108
6	General Description of CNT-CNT Conductance	111
6.1	Background	111
6.2	Predictive Model	112
6.3	Comparison with Computational Results	117
6.4	Summary	121
7	Summary, Relevance, and Future Direction	125
7.1	Summary of Major Results	125
7.2	Relevance to Application Areas	128
7.3	Future Directions	129
	Publications and Presentations	135
	Appendix A	138
	Bibliography	150

List of Figures

- 3.1 A representative steady-state temperature profile obtained in a simulation performed for a 630 nm long (10,10) CNT. The data points are calculated for ~ 24.2 nm segments along the CNT. The line is a linear fit that is used in the calculation of the temperature gradient. The fit excludes the data points that correspond to the heat bath regions and first points adjacent to the heat bath regions. 27
- 3.2 A representative plot of the time evolution of thermal conductivity, k , calculated from temperature profiles averaged over a moving 100 ps temporal window in a simulation of heat flow through a 630 nm long (10,10) CNT. The steady state is deemed to be reached by the time of 3250 ps (marked by the vertical line) and the final value of k is determined by averaging all data obtained within the time interval indicated by the horizontal arrow. . . 29
- 3.3 Thermal conductivity, k , of (10,10) CNTs as a function of sample length, L_C , defined as the distance between the hot and cold heat bath regions. For comparison, the length dependencies of thermal conductivity reported by Lukes and Zhong [1], Thomas et al. [2], Shiomi and Maruyama [3], and Padgett and Brenner [4] are also plotted. While quantitative discrepancies are present, all sets of data exhibit a consistent trend of strong length dependence for short CNTs transforming to weaker increase for CNTs that are longer than ~ 200 nm, thus signifying the transition from the ballistic to diffusive-ballistic heat transport regimes. 31
- 3.4 A schematic of a computational setup used in NEMD simulations of thermal conductivity of CNTs and the definitions of the length parameters. Two heat bath regions of length L_B are separated by a central tube region of length L_C 33

- 3.5 Thermal conductivity, k , as a function of the length of the heat bath regions, L_B . The results are shown for two series of NEMD simulations performed with fixed distance between the heat bath regions: in Series 1 (green triangles) $L_C = 50$ nm and in Series 2 (red squares) $L_C = 97$ nm. The error bars show the estimates of the standard error of the mean, with some error bars obscured by the width of the data points. The solid green and dashed red lines mark the values of k predicted in simulations of Series 1 with $L_B = L_C = 50$ nm and Series 2 with $L_C \approx L_B = 100$ nm, respectively. The consistent trend of increasing thermal conductivity for $L_B > L_C$ contradicts the notion that the sensitivity of the results to L_B is due to the thermal boundary resistance at the boundaries of the heat bath regions. 35
- 3.6 Thermal conductivity, k , as a function of (a) length of the central part of the CNT, L_C , and (b) the total length of the CNT, L_{Sys} . The results are shown for three series of NEMD simulations: in Series 1 (green triangles) CNTs have fixed $L_C = 50$ nm and varied L_B , in Series 2 (red squares) CNTs have fixed $L_C = 97$ nm and varied L_B , and in Series 3 (blue circles) CNTs have fixed $L_B = 0.5$ nm and varied L_C . While it is common to use L_C as a measure of the effective CNT length in NEMD simulations of thermal conductivity, plotting k versus L_{Sys} in (b) provides a more consistent representation of the length dependence of k across all series of simulations, regardless of whether the length is added to the central region (Series 3) or the bath regions (Series 1 and 2) of the nanotube. 37
- 3.7 Schematics of computational setups with bi-directional heat flux implementations used in NEMD simulations of thermal conductivity of CNTs. The two setups are shown for free (a) and periodic (b) boundary conditions. In the case of free boundary conditions, the CNTs are covered by hemispherical fullerene caps that are not included in the heat bath regions. 43
- 3.8 Thermal conductivity, k , predicted in NEMD simulations performed with four different interatomic potentials for identical CNTs under identical computational conditions. 46
- 3.9 A schematic representation (not to scale) of the three aligned CNT bundles (a) and representative temperature profiles obtained in the simulations performed for (10,10) CNTs of length $L_T = 160$ nm (b). Thermal flux is applied to each CNT individually and the values of thermal conductivity are obtained from the steady-state temperature profiles. All simulations are performed for capped CNTs with the cylindrical part of length L_T . The temperature profiles in panel (b) for 2- and 7-CNT systems are obtained by averaging the profiles calculated for individual CNTs in the bundles. 49
- 4.1 A comparison of the values of CNT-CNT conductance predicted for different overlap lengths in two studies by Zhong and Lukes [5] and Xu and Buehler [6]. The values have been manipulated from the original reference to reflect conductance per overlap length, and are normalized with respect to the highest value found in the respective studies. Both works show an inverse relationship between conductance per area and contact area. 59

- 4.2 A schematic of a configuration employed to investigate the effect of CNT length on CNT-CNT conductance. Energy is uniformly added to Tube 1 and uniformly removed from Tube 2 at a rate of Q_{HB} . The lengths of both tubes, L_T , are identical and varied between simulations. 60
- 4.3 Calculations of CNT-CNT conductance, G , as a function of CNT length, L_T , obtained from this work (red circles) and a less extensive work by Evans et al. [7] (blue squares). The uncertainty in the final calculations of this work is represented by one sample standard deviation of all sequential G calculations obtained after achievement of a steady state. This value can vary between simulations as it is dependent on the statistical noise associated with the calculation of the temperature of each tube and the temperature difference between tubes, ΔT_{12} , both of which vary between simulations. The present study and the calculations by Evans et al. predict similar values of G for CNT lengths $L_T \leq 10$ nm. For longer CNT lengths, Evans et al. predict an abrupt deviation from the trend and a lower saturation limit. 63
- 4.4 Inverse of conductance, G , plotted with respect to the inverse of CNT length, L_T . The linear extrapolation technique allows for prediction of conductance between two infinitely long CNTs. 65
- 4.5 A schematic of the configuration employed to investigate the effect of contact density on CNT-CNT conductance. Energy is uniformly added to Tube 1 and uniformly removed from Tubes 2 and 3 at a rate of $2Q_{HB}$. The lengths of all tubes, L_T , is 100 nm and the distance between the centers of Tube 2 and Tube 3, d , is varied between simulations. 67
- 4.6 Conductance, G , per junction plotted with respect to distance between junctions, d . The uncertainty is represented by one sample standard deviation of all sequential G calculations obtained after achievement of a steady state. There is no statistically significant effect from the presence of neighboring junctions, except for the case when $d \approx 0.314$ nm, the equilibrium separation distance, which demonstrates a $\sim 10\%$ reduction. This contradicts findings by Prasher et al. [8] who predict a reduction by approximately one order of magnitude. 68
- 4.7 Computational setup used in MD simulations of the conductance through overlap regions between parallel CNTs. Block arrows indicate the directions of the heat flow. The flux across the overlap regions is created by adding energy at a constant rate Q_{HB} in the heat bath region in the center of Tube 1 and removing it from the heat bath region in the center of Tube 2. Each of the heat bath regions has length of 2 nm. Periodic boundary conditions are applied in the axial direction. 70
- 4.8 A representative temperature distribution in the overlapping Tubes 1 (red curve) and 2 (blue curve) obtained by averaging data over 6.7 ns in the steady-state regime of a simulation performed for (10,10) CNTs with length $L_T = 200$ nm and overlap length $\Delta x_{12} = 40$ nm. The temperature drop at the inter-tube contact, ΔT_{12} , is calculated as the difference of the average temperatures of the overlapping CNT segments. 71

4.9	Comparison of the temperature distributions in the vicinity of the overlap region obtained from the predictions of an analytical solution (thick light curve) and the MD simulation (black dots). The temperature profile corresponding to predictions of the MD simulation was obtained by averaging data over 6.7 ns in the steady-state regime.	72
4.10	Inter-tube conductance per unit length, σ_T , versus overlap length, Δx_{12} , obtained in MD simulations for two parallel partially overlapping (10,10) CNTs of 100 nm (blue squares) and 200 nm (red circles) length. The computational setup used in the simulations is shown in Fig. 4.7. The error bars show one sample standard deviation calculated for “instantaneous” values of inter-tube conductance collected during the steady-state part of the simulation.	73
4.11	A schematic of the computational setup employed to investigate the effect of contact area on conductance at a CNT-CNT junction. Energy is uniformly added to Tube 1 and uniformly removed from Tube 2 at a rate of Q_{HB} . The lengths of both tubes are fixed at 100 nm and the angle θ is varied between simulations.	76
4.12	A representative plot of atomic positions recorded during the constant flux implementation for the configuration where initial $\theta = 20^\circ$. The central region of each CNT deforms to minimize the inter-tube interaction energy, thus altering the local configuration at the junction. A spring force with spring constant $K_{Spr} = 0.01 \text{ eV } \text{\AA}^{-2}$ is applied to the 150 atoms in the ends of each CNT to prevent complete alignment of the CNTs.	78
4.13	Predicted values of G are plotted with respect to the total number of interatomic interactions between CNTs, N . Error bars represent one sample standard deviation of the sample set of predictions of G and are provided as a measure of uncertainty. Total conductance is observed to increase with increasing N	81
4.14	Values of the average conductance per inter-tube interaction, G/N , plotted with respect to the total number of interatomic interactions between CNTs, N . The ranges of the error bars are determined by dividing the sample standard deviations of G predictions by the values of N for each configuration and are provided as a measure of uncertainty. The data consist of two distinct groups, with configurations with relatively low values of N (i.e., initial $\theta \geq 35^\circ$) having values of G/N which are all similar to each other and higher than the values of G/N for configurations with higher values of N (i.e., initial $\theta = 20^\circ$ and 0°), which are also similar to each other.	82

- 4.15 Predicted values of the average conductance per inter-tube interaction, G/N , are plotted with respect to the average number of inter-tube interactions per atom in the contact region, M . The ranges of the error bars are determined by dividing the sample standard deviations of G values by the values of N for each configuration and are provided as a measure of uncertainty. The data form two distinct groups, with configurations with initial $\theta \geq 35^\circ$ having relatively lower values of M due to a greater proportion of atoms in the contact regions being located in the periphery of the contact. Greater predicted values of G/N are observed for configurations with relatively lower values of M , suggesting conductance per interaction is greater in areas with less inter-tube interactions. 83
- 5.1 A representative steady-state temperature profile obtained in the reference simulation. The temperature profiles for Material 1 and Material 2 are shown in blue and red circles, respectively. The black curves are independent linear fits that are used to define the temperatures of Material 1 and Material 2 adjacent to the interface, T_L and T_H respectively. The fit excludes the data points that correspond to the heat bath regions and the first five segments adjacent to either the heat bath regions or the interface. The interfacial temperature, T_{int} , is determined by the mean of T_L and T_H and the temperature drop across the interface, ΔT , is determined by $T_H - T_L$. 91
- 5.2 The time evolution of interfacial conductance, G , calculated from the temperature profiles and temperature drop, ΔT , averaged over a moving temporal window in a simulation of heat flow through the reference sample. The steady state is deemed to be reached by the time of $t = 7500$ (marked by the vertical line). The final value of G is determined by averaging all data obtained after achievement of the steady state indicated by the horizontal arrow. 92
- 5.3 Values of interfacial thermal conductance, G , between two 2D LJ materials plotted as a function of the temperature drop across the interface, ΔT , resulting from variations in the implemented heat flow rate, Q_{HB} . The values of G are determined by the mean of 10 sample calculations taken in the steady state and the ranges of the error bars are determined from the estimate of the standard error of the mean. No statistically significant variation in G values is observed, suggesting G is independent of Q_{HB} over the range studied. 94
- 5.4 Values of interfacial thermal conductance, G , between two 2D LJ materials plotted as a function of the interfacial temperature, T_{int} . The values of G are observed to increase with increasing T_{int} . This result is expected due to the contribution of inelastic phonon scattering processes to interfacial thermal transport, which increases with temperature [9]. 95

- 5.5 Values of interfacial thermal conductance across Interface 1-2, G , plotted as a function of the total number of interfaces in the system, I . The unique computational setup is designed such that Material 1 forms multiple interfaces with multiple identical materials which do not interact with each other. Thus, an increase in the value I corresponds to an increase in the number of interatomic interfacial interactions experienced by Material 1, but does not affect the interfacial area or the number of interatomic interfacial interactions contributing to interfacial conductance for Interface 1-2. The results suggest conductance per interatomic interfacial interaction decreases with increasing density of interatomic interfacial interactions. . . . 98
- 5.6 Calculations of the normalized PSD for the Type 1 and Type 2 atoms adjacent to Interface 1-2 are represented by blue and red curves, respectively, for the single interface, 3-interface, 6-interface, and special case systems. The area of overlap between the two normalized PSD curves, the value of which is provided in the legend and is visually represented by the gray shaded area in each plot, is a measure of the similarity between the normalized PSD curves. The normalized PSD for Type 1 atoms is shifted to higher frequencies for increasing number of interfaces, which indicates less similarity between the local occupied DOS of the two atom types adjacent to the interface, and corresponds to a decrease in the value of G . The interaction energy experienced by Type 1 atoms adjacent to the interface is equal in both the 3-interface and special case systems. However, the value of the area of overlap in the 3-interface system is less than the value of the area of overlap in the special case system, suggesting an additional effect caused by the incoherent trajectories of the atoms adjacent to each of the multiple interfaces in the 3-interface system. 104
- 5.7 Calculations of the normalized PSD for the Type 1 and Type 2 atoms adjacent to Interface 1-2 are plotted for the 3-interface and special case systems. The normalized PSD for Type 1 atoms in the 3-interface and special case systems are represented by blue and black curves, respectively. The normalized PSD for Type 2 atoms in the 3-interface and special case systems are represented by solid red and dashed red curves, respectively, and show very little variation between systems. These two curves are intentionally chosen to have the same color to demonstrate the nearly indistinguishable difference between them. The value of overlap area for frequencies below Frequency = 3 is greater in the special case system than in the 3-interface system, and the difference between the two values is visually represented by the gray shaded area. Variation between the normalized PSD for Type 1 atoms in the 3-interface and special case systems suggest the presence an additional effect caused by the incoherent trajectories of the atoms adjacent to each of the multiple interfaces in the 3-interface system. 106

- 6.1 The scaling factor, n , which is described by Eq. 6.1 and scales the contribution of each inter-tube atomic pair to the total “effective” number of interatomic inter-tube interactions, N_{eff} , based on the separation distance between each atomic pair, r_{ij} . All inter-tube atomic pairs with r_{ij} less than the equilibrium separation distance of the LJ potential, r_m , are counted as one interaction, with r_{ij} greater than the LJ cutoff distance, r_c , are not counted, and with $r_m \leq r_{ij} \leq r_c$ are scaled by the absolute value of the LJ potential for the given r_{ij} , and normalized such that $|U_{ij}^{LJ}(r_m)| = 1$ 113
- 6.2 The conductance per total “effective” number of interatomic inter-tube interactions, G/N_{eff} , plotted as a function of the average number of “effective” interatomic inter-tube interactions per atom in the contact region, M_{eff} . Values of G/N_{eff} are calculated from the results of MD simulations and represented by red circles. The error bars represent the division of the standard deviation of the instantaneous values of G by the final mean value of N_{eff} , for each simulation. The blue curve represents the function $g(M_{eff})$, which is defined by Eq. 6.5, empirically fit to the results of the MD simulations, and incorporated into the final predictive model, $G(N_{eff}, M_{eff})$, given by Eq. 6.6. 116
- 6.3 The values of conductance, G , obtained by the MD method, represented by red circles, and by the predictive model, represented by blue and black crosses, plotted with respect to the total “effective” number of interatomic inter-tube interactions, N_{eff} . Error bars represent one sample standard deviation of the sample set of calculations of G by the MD method and the predictive model. Blue crosses represent the results of the predictive model for configurations of partially overlapping parallel CNTs, and black crosses represent the results of the predictive model for configurations similar to the ones described in Section 4.2.4 and a special case configuration of two parallel 100 nm CNTs with overlap length $\Delta x_{12} = 10$ nm and free boundary conditions in all directions. The results of predictive model and the MD method show the least amount of agreement for the case of two CNTs forming a junction with initial $\theta = 20^\circ$. Inconsistencies with the results of this configuration simulation and the results of the other simulations are discussed in detail in the text. The results of the predictive model show good agreement with the MD results for all other configurations. 120

List of Tables

3.1	A sample of the values of CNT thermal conductivity predicted in MD studies reported in the literature. All values are for (10,10) single-walled CNTs at ~ 300 K. The system length is defined as the total length of the computational system used in the simulations. The nomenclature for the names of the interatomic potentials is explained in the text.	18
3.2	Sample data taken from Fig. 3.6. Overall system length, L_{sys} , which includes the heat bath regions, is found to be a better predictor of conductivity than the distance between the heat bath regions, L_C	38
3.3	The upper saturation limit of conductivity, k_∞ , and phonon mean free path, l_∞ , predicted by fitting the results of NEMD simulations to Eq. 3.5. The values of L_C and L_B correspond to systems extrapolated to infinite overall length, L_{sys} , by following the procedures of the three series of simulations. Series 3 provides the most realistic representation of the true system of interest, with length added to the central region of the nanotube. Despite length being added to the heat bath regions while L_C is kept constant, Series 1 and 2 provide estimates of k_∞ that are surprisingly close to the more realistic prediction of Series 3.	40
3.4	Thermal conductivity of (10,10) CNTs, k , predicted in NEMD simulations performed with bi-directional and uni-directional heat flux implementations. The predictions of the two types of simulations are reconciled when the results are compared for the same effective length defined as $L_C + 2L_B$	44
3.5	Thermal conductivities of a (10,10) CNT, k , and the corresponding standard deviations from the mean values predicted in MD simulations performed for a single CNT, a pair of parallel interacting CNTs, and a bundle of 7 CNTs, as shown in Fig. 3.9a, for the CNT length $L_T = 160$ and 300 nm. In multi-tube simulations, the conductivity reported is the mean of all conductivity calculations for the 2 or 7 CNTs in the corresponding configurations. The measure of uncertainty presented is one sample standard deviation of all sequential k calculations obtained after achievement of a steady state. The values of k in all configurations with $L_T = \text{const}$ are within the standard deviations of each other, suggesting that the effect of the inter-tube coupling on the intrinsic thermal conductivity of CNTs is statistically insignificant.	48

Nomenclature

A	Fitting parameter
B	Fitting parameter
	Tersoff bond order function
C	Fitting parameter
c	Phonon heat capacity per unit volume
d	Distance
F	Force
f	Tersoff potential cutoff function
G	Thermal conductance
	Tersoff potential function term
g	Tersoff potential function term
	Predictive model term
h	Tersoff potential function term
I	Number of interfaces
K	Spring constant
k	Thermal conductivity
	Boltzmann constant
	Sample calculation
L	Length
l	Phonon mean free path
M	Average number of interfacial interatomic interactions per atom adjacent to the interface
	Number of calculations in a sample set
m	Atomic mass

N	Number of interfacial interatomic interactions Number of atoms Number of estimations of a value
n	Scaling factor
Q	Energy per unit time
q	Energy flux
R	Radius
r	Distance
S	Sample standard deviation
T	Temperature
t	Time
U	Potential energy
v	Atomic velocity Average phonon velocity
x	Position

Greek Symbols

Δ	Difference
δ	Wall thickness Dirac delta distribution
Δx	Overlap length
ε	Lennard-Jones energy parameter
Φ	Tersoff potential pair-wise function
σ	Lennard-Jones distance parameter Thermal conductance per unit overlap length
θ	Angle
Ω	Cross-sectional area

Superscripts

$*$	Lennard-Jones reduced units
T	Tersoff
LJ	Lennard-Jones

Subscripts

1	Index
2	Index
3	Index
<i>B</i>	Bath
	Boltzmann
<i>C</i>	Central
	Cutoff
<i>eff</i>	Effective
<i>HB</i>	Heat bath
<i>H</i>	High
<i>i</i>	Index
<i>int</i>	Interface
<i>j</i>	Index
<i>k</i>	Index
<i>L</i>	Low
<i>loc</i>	Local
<i>m</i>	Minimum
<i>max</i>	Maximum
<i>S</i>	Segment
<i>Spr</i>	Spring
<i>Sys, sys</i>	System
<i>T</i>	Tube
<i>x</i>	Position
	Index
<i>y</i>	Index

Chapter 1

Introduction

1.1 Motivation

Carbon nanotubes (CNTs) have gained a significant amount of research interest for use in thermal management applications due to exceptionally high values of the intrinsic CNT thermal conductivity, k , reported in experiments [10–17] and computational studies [1–4, 18–34]. However, when these CNTs are formed into structures or incorporated into materials, the collective thermal conductivity through the structure or material is found to be orders of magnitude lower than the values of measurements of individual CNT thermal conductivity [8, 35–41]. Two major factors may be responsible for the low conductivity of the CNT structures: the reduction of the intrinsic conductivity of individual CNTs due to the inter-tube interactions, and low thermal conductance at CNT-CNT contacts that may be sensitive to the geometry of the contact and the local contact density.

Few experiments have been conducted to measure the thermal conductance at CNT-CNT contacts. Cola et al. extrapolated a value for the interfacial thermal resistance between multiwalled CNTs from the resistance measured between two interfacing CNT arrays by the photoacoustic technique [42]. They reported a value that corresponds to an interfacial conductance of roughly $\sim 4.8 \times 10^5 \text{ Wm}^{-2}\text{K}^{-1}$. Yang et al. measured the total thermal resistance of an intersection of two suspended multiwalled CNTs [43]. They extrapolated a value for the interfacial thermal resistance at the CNT-CNT contact by subtracting a value

of resistance for each multiwalled CNT, which was calculated by interpolation of resistance measurements of multiwalled CNTs with different diameters. Their reported values correspond to interfacial conductance of roughly $\sim 8.3 \times 10^7$ and $\sim 8.2 \times 10^8 \text{ Wm}^{-2}\text{K}^{-1}$ for the cases when the CNTs form an aligned contact and cross contact, respectively. To date, there has been no direct measurement of the thermal conductance between single-walled carbon nanotubes.

Thermal conduction between CNTs is achieved through relatively weak, non-bonded van der Waal's forces. Typical dimensions of CNT materials and structures are much longer than their constituent CNTs. Therefore, thermal transport in these devices may be limited by the relatively weak thermal coupling between CNTs [5–8, 43–47]. Any measures that can improve inter-tube conductance will directly improve the thermal performance of the CNT structure as well. Therefore, it is important to determine what structural parameters affect thermal transport across CNT-CNT junctions. Further background information and a systematic study designed to investigate the effects of structural parameters on CNT-CNT conductance are discussed in Chapter 4 of this dissertation.

In most CNT-based materials and structures, individual CNTs arrange and form networks of bundles due to the attractive van der Waal's forces between individual nanotubes [14, 48–52]. It has been previously suggested that the low conductivity of CNT structures is due to the reduction of the intrinsic conductivity of individual CNTs via inter-tube interactions [53–55]. If this is true, the overall thermal transport through CNT-based materials may be improved by optimizing the configuration of the underlying CNT network to limit the reduction in CNT conductivity. However, this suggested effect of inter-tube interactions is only a conjecture extrapolated from a comparison of computational predictions of the thermal conductivity of a graphene monolayer and graphite [18]. A more thorough investigation is needed to evaluate the sensitivity of individual CNT k to inter-tube interactions. Further background information on the effects of inter-tube interaction on CNT k is included in Section 3.1.3 and the results of a systematic study to investigate these effects

are discussed in Section 3.2.4 of this dissertation.

Individual CNTs have diameters of only a few nanometers and are difficult to isolate and experimentally study in the absence of environmental effects. Direct experimental measurement of the thermal properties of individual CNTs has been hampered by technical challenges related to the small size of the individual nanotubes and their propensity to form bundles and aggregate into intertwined structures. These challenges have led to variability of the results of experimental measurements of thermal conductivity of individual CNTs [10–17, 56]. With wide variation among experimental measurements, experimental investigation to determine which factors affect CNT conductivity or CNT-CNT conductance becomes difficult. Molecular dynamics (MD) simulations have become a popular method for studying the fundamental properties of CNTs, as the simulated environment can be controlled completely, eliminating any ambiguity about the physical system being studied. The only input needed is a definition of the interatomic potential function. Equations of motion are then solved to find the atomic trajectories, *i.e.*, atomic positions and velocities as a function of time. Allowing complete control of the simulated environment while requiring minimal input, the MD simulation method is a promising tool for the systematic investigation of the variables that may affect CNT k or CNT-CNT conductance.

Despite the simplicity of the basic idea behind the MD simulations, there has been a significant divergence in published results of CNT k obtained by MD simulation. This variability may be caused by two fundamentally different factors: True variation in intrinsic CNT conductivity due to variability in the local environment such as CNT length, and variation of k due to the difference between simulation setups employed in the different works such as computational procedure or interatomic potential. The effects of these two factors must be better understood and accounted for if the MD simulation method is to be used for systematic investigation of CNT k or CNT-CNT conductance. Additional background information and the results of MD studies designed to investigate the sensitivity of MD predictions of CNT k to CNT length and variation in simulation setups are discussed

in Chapter 3 of this dissertation.

Some examples of thermal applications of CNT-based materials and the motivation for implementing the MD simulation method are provided in the remainder of this section. The major objectives and outline of the remainder of this dissertation are summarized in Section 1.2.

1.1.1 Thermal Applications of CNT-based Materials

As simultaneous reduction in size and enhancement in power levels of microelectronic devices generate higher levels of heat density, development of advanced thermal management systems becomes critical [57]. Due to high values of measured CNT conductivity, there is much interest in the use of CNTs and CNT-based materials for thermal management applications. One potential solution is the use of CNTs to enhance the efficiency of heat sinks and heat dissipation to the surrounding environment. Specific examples of this implementation include efficient cooling of silicon chips by CNT microfin structures [58], the filling of microchannels in microelectronic devices with CNTs [59], and the use of CNT bumps in high-frequency, high-power, flip-chip amplifiers [60].

Another possible solution is the incorporation of CNTs into thermal interface materials (TIMs) to enhance the thermal contact between a heat source and a heat sink. TIMs that incorporate CNTs have been made in the form of thermal pastes [61] and coatings based on CNT arrays [62–68]. These coatings, consisting of vertically aligned arrays of CNTs (or CNT forests) immersed into a polymer matrix, exploit the high thermal conductivity of individual CNTs for the direct heat transfer.

In addition to the thermal management in microelectronic devices, the unique thermal properties of CNTs and CNT-based materials lead to additional thermal applications. For example, in contrast to high reported values of thermal conductivity of anisotropic CNT materials in the direction of preferred alignment of CNTs, the thermal conductivity of CNT thin films in the direction perpendicular to the surface of the film is found to

be orders of magnitude lower (e.g. $\sim 2 \text{ Wm}^{-1}\text{K}^{-1}$ [37]). This suggests that CNT structures may be designed to produce materials with highly anisotropic thermal conductivity, with applications such as thermal wave-guides, switches, and pumps [69]. There is interest in producing CNT-based thin film transistors for use in macroelectronic circuits, due to their combination of thermal and mechanical properties [70]. CNTs show promise for improving performance of fire retardant materials as well. Gasification tests performed for Poly(methyl methacrylate) (PMMA), a common shatter-resistant alternative to glass, reinforced by 0.5 wt.% of CNTs revealed a threefold decrease in the heat release rate compared to pure PMMA [71].

1.1.2 Molecular Dynamics Simulations

The variability of the results of experimental measurements of CNT conductivity and CNT-CNT conductance reflects difficulties in obtaining accurate quantitative measurements. A systematic experimental investigation of the dependencies of CNT conductivity and CNT-CNT conductance on the geometrical and structural parameters of CNTs (length, diameter, chirality, curvature, presence of defects) and external conditions (temperature, thermal contact resistance, interactions with other CNTs and/or substrate) would also be hampered by these difficulties. However, a better understanding of these dependencies is necessary for the design and optimization of CNT-based materials for thermal applications.

MD simulations allow for complete control over the size and structure of the CNTs and have been used in investigations of the dependence of the thermal conductivity on CNT length [1–4, 21–23, 26, 28–30, 33, 34, 72–76], diameter [2, 3, 20–22, 26, 29, 30, 32–34, 75, 77], elastic deformation [31, 78–80], buckling [81–83], as well as presence of isotope dopants [26, 28, 30, 75], crystal defects [19, 28, 75], or chemisorbed molecules [4]. With complete characterization of the physical system being studied, the MD simulation method allows for a systematic study of the dependencies of CNT conductivity and CNT-CNT conductance on parameters that may be modified to optimize the thermal properties

of CNT-based materials.

Here an important distinction is made between qualitative and quantitative investigations. Due to the variability of experimental results, it is difficult to quantify the accuracy of the values obtained from MD predictions. As noted above, there has also been a significant divergence in published results of CNT k obtained by MD simulation. In fact, resolving some of the discrepancies among MD results is one of the major objectives of this work. However, the motivation for the application of the MD simulation method is to investigate the effects of the surrounding environment and physical configuration on the thermal properties of CNTs and CNT structures in the absence of any ambiguity about the physical system. The goal is a better understanding of these qualitative effects rather than quantitative accuracy of the predicted thermal properties. Given that there remains variability of the quantitative results of experimental measurements, MD simulations provide a useful tool in the efforts to meet that goal and optimize CNT-based materials for thermal applications.

1.2 Objectives and Outline

The main objectives of the study reported in this dissertation is as follows:

- *Objective 1:* Evaluate the effects of common variations in computational parameters adopted in different MD studies, which may contribute to discrepancies in predicted values of CNT thermal conductivity.
- *Objective 2:* Examine the sensitivity of the intrinsic thermal conductivity of CNTs to inter-tube interactions in CNT bundles.
- *Objective 3:* Examine the sensitivity of conductance at CNT-CNT contacts to characteristics of the physical configuration and surrounding environment such as CNT length, density of contacts, and contact area.

- *Objective 4:* Develop an empirical model capable of describing the conductance at CNT-CNT contacts for an arbitrary configuration of CNTs.

The material covered in the remaining part of this dissertation is outlined below:

- *Chapter 2, Molecular Dynamics Simulations:* An introduction to the classical molecular dynamics simulation method is provided. Background information on several relevant interatomic potentials is provided. The large-scale atomic/molecular massively parallel simulator (LAMMPS) package, which is used for molecular dynamics simulations in this work, is described.
- *Chapter 3, CNT Thermal Conductivity:* This chapter addresses both Objectives 1 and 2. First, relevant background information on CNT thermal conductivity is provided, followed by results and discussion of MD simulations performed to investigate CNT conductivity.
 - *Section 3.1, Background:* Background information on the variation of CNT conductivity values predicted by MD simulations is provided. Common variations in the computational setups adopted in different studies are discussed.
 - *Section 3.2, Computational Results:* MD simulations are performed to investigate factors that affect MD predictions of CNT conductivity. The dependence of the intrinsic CNT conductivity on CNT length and inter-tube interactions is explored. The variation of the computational predictions of CNT conductivity due to variability of computational procedures and interatomic potentials is also explored. The results are summarized and discussed.
- *Chapter 4, CNT-CNT Thermal Conductance:* This chapter addresses Objective 3. First, relevant background information on CNT-CNT conductance is provided, followed by results and discussion of MD simulations performed to investigate CNT-CNT conductance.

- *Section 4.1, Background:* Background information on the conductance at CNT-CNT contacts is provided. Factors that may affect predictions of MD calculations of CNT-CNT conductance, such as CNT length, contact density, and contact area, are considered.
 - *Section 4.2, Computational Results:* MD simulations are performed to investigate the effects of CNT length, contact density, and contact area on CNT-CNT conductance. The results are summarized and discussed.
- *Chapter 5, Thermal Conductance between Two-Dimensional Lennard-Jones Materials:* Thermal conductance across a 2-dimensional interface is investigated by MD simulations employing the Lennard-Jones interatomic potential. The sensitivity of interfacial conductance to the local density of non-bonded van der Waal's interactions is explored. The implications of the results of this study for the design of the general model for CNT-CNT conductance are discussed.
- *Chapter 6, General Description of CNT-CNT Conductance:* This chapter addresses Objective 4. A general description of the conductance at CNT-CNT contacts is designed for an arbitrary configuration, based on the results of Chapters 4 and 5. Agreement in predicted values of CNT-CNT conductance between this model and MD simulations is demonstrated.
- *Chapter 7, Summary, Relevance, and Future Direction:* The major results of this work are summarized and successful completion of all major objectives is demonstrated. The significance of the results is discussed in the context of the stated motivations. Ideas for future research directions are suggested.

Chapter 2

Molecular Dynamics Simulations

2.1 Background

The molecular dynamics (MD) simulation method is a computational method that solves Newton's equations of motion to predict the time-evolution of the positions and velocities of atoms in a computational domain. The local temperature of a region of the simulated system can be calculated from the average kinetic energy of the atoms in the region of interest,

$$T_{loc} = \frac{1}{3k_B N_{loc}} \sum_{i \in loc} m_i v_i^2, \quad (2.1)$$

where T_{loc} is the local temperature of the region, N_{loc} is the number of atoms in the region, v_i is the instantaneous velocity of atom i , m_i is the atomic mass, k_B is the Boltzmann constant, and the summation is performed over all atoms in region loc .

Thermal properties of the modeled material may be studied through the application of Eq. 2.1 to the MD simulation output. In the non-equilibrium molecular dynamics (NEMD) method, a thermal flux is created between “heat bath” regions defined in the system by removing kinetic energy from a cold heat bath region and adding the same amount of energy to a hot heat bath region through a scaling of atomic velocities. All results presented in this work were obtained from MD simulations employing the NEMD method. More detailed descriptions of the NEMD method and specific computational procedure used are provided with the introduction of each simulation series throughout this dissertation.

There are two major inputs for any MD simulation: Definition of the computational domain which includes the mass, initial position, and initial velocity of each atom, and definition of the interatomic potential which describes the interactions between atoms. Choice of interatomic potential is dependent on the material being modeled. Three interatomic potentials commonly implemented in the investigation of CNTs are summarized in Section 2.2. The majority of MD simulations performed for this work employ at least one of the interatomic potentials outlined there. All MD simulations performed for this dissertation utilized the Large-scale Atomic/Molecular Massively Parallel Simulator (LAMMPS) package which is discussed in Section 2.3.

2.2 Interatomic Potentials

The interatomic potential that defines the interaction forces between atoms in a simulated system is a key ingredient of any MD model. The choice of interatomic potential has direct effect on any quantitative prediction of MD simulations, including prediction of thermal properties. When MD simulations are employed to model CNTs, an interatomic potential must be chosen to define the chemically bonded interactions between carbon atoms within the same CNT. In addition, a second interatomic potential may be chosen to model non-bonded van der Waal's interactions between either carbon atoms within the same CNT that do not share a chemical bond, or carbon atoms belonging to neighboring, interacting CNTs. While this second interatomic potential must be defined to model intertube interactions, it is not always employed in studies where the MD simulation method is used to investigate a single CNT in isolation.

The choice of interatomic potential used to study thermal properties of CNTs varies among MD studies. The sensitivity of MD predictions of the value of CNT thermal conductivity to the choice of interatomic potential is discussed further in Chapter 3. The remainder of this sub-section briefly introduces some of the common interatomic potentials

employed in MD investigations of thermal properties of CNTs. The interatomic potentials summarized in this sub-section neither represent a complete list of all possible potentials available for modeling thermal properties of CNTs, nor represent the potentials expected to produce the most quantitatively accurate predictions. The majority of simulations described in this work employ at least one of these interatomic potentials, thus some brief background information is provided for each.

2.2.1 Lennard-Jones Potential

One of the most mathematically simple and earliest forms of interatomic potential was proposed by Lennard-Jones [84]. In the 12-6 form of the Lennard-Jones (LJ) potential, the interaction energy between two atoms i and j is given as,

$$U_{ij}^{LJ} = 4\epsilon \left[\left(\frac{\sigma}{r_{ij}} \right)^{12} - \left(\frac{\sigma}{r_{ij}} \right)^6 \right], \quad (2.2)$$

where r_{ij} is the separation distance between atoms i and j , ϵ is the energy parameter which defines the minimum value of the potential, and σ is the distance parameter which defines the separation distance at which the repulsive side of the potential equals zero. These parameters can be adjusted and optimized to model a system of interest [85]. For the sake of computational efficiency, a cutoff function is typically applied which ensures either a smooth or sharp transition of the LJ potential to zero by some separation distance at which the atoms are considered to be non-interacting [86–88].

The LJ potential was originally developed to model the non-bonded van der Waal's interactions in Argon gas [84]. Non-bonded van der Waal's interactions are also responsible for thermal conductance between CNTs. Formulations of the LJ potential have been parameterized for non-bonded interactions between carbon-based structures [87, 89, 90] and used in MD studies investigating CNT-CNT conductance [7, 91, 92]. MD simulations employing the LJ potential to model van der Waal's interactions between CNTs were per-

formed for this dissertation to predict CNT-CNT conductance and the results are discussed in Section 4.2.

The simplicity of the LJ potential makes it an attractive choice when modeling the qualitative physics of a system is more important than quantitative accuracy of the prediction of material specific properties [93]. This simplicity can facilitate the investigation of phenomena that may be obscured in more complex systems [94]. Without loss of generality, simplistic “toy” models allow for qualitative and controlled investigation of physical trends in systems that are not material specific. The LJ potential has been used to model a wide range of “toy” systems with varying characteristics [88, 93–98]. A series of MD simulations employing the LJ potential to investigate the thermal conductance across an interface between two-dimensional (2D) Lennard-Jones materials was performed for this dissertation. The motivation for this work and results are discussed in Chapter 5.

The generality of “toy” models can be extended by presenting results with non-dimensional units that are normalized by the LJ potential parameters. The LJ reduced units are denoted by “*” and related to the corresponding real units by

$$\begin{aligned}
 r^* &= r/\sigma, \\
 E^* &= E/\varepsilon, \\
 m^* &= m, \\
 T^* &= Tk_B/\varepsilon, \\
 t^* &= t\sqrt{\varepsilon/(m\sigma^2)},
 \end{aligned}
 \tag{2.3}$$

for distance r , energy E , mass m , temperature T , and time t , where k_B is the Boltzmann constant. Here, σ and ε are the LJ distance and energy parameters respectively. LJ reduced units allow predictions of the properties of one LJ material to be extrapolated from the results of simulations of another LJ material possessing different LJ potential parameters. This allows full generalization of results predicted from “toy” models.

2.2.2 Tersoff Potential

The Tersoff potential is a bond order potential with an original functional form and parameterization defined by Tersoff in 1988 [99, 100]. A bond order potential differs from the pair-wise LJ potential in that the strength of a bond between two atoms is dependent on the bonds those atoms share with other atoms [101]. The Tersoff potential for a bond ij between atoms i and j is given as,

$$U_{ij}^T = f_C(r_{ij})[\Phi_R(r_{ij}) + B_{ij}(G_{ij})\Phi_A(r_{ij})], \quad (2.4)$$

where Φ_R and Φ_A are the repulsive and attractive pair-wise potentials respectively, and are functions of the bond length, r_{ij} . The cutoff function is represented by f_C and transitions from 1 to 0 over a small range of bond lengths close to the first nearest-neighbor distance. The bond order function B_{ij} is used to adjust the strength of bond ij and is a function of G_{ij} which takes the form,

$$G_{ij} = \sum_{k \neq i, j} f_C(r_{ik})g(\theta_{ijk})h_D(r_{ij} - r_{ik}), \quad (2.5)$$

where g is a function of θ_{ijk} , the bond angle between bonds ij and ik , and h_D is a function of the difference between bond length r_{ij} and bond length r_{ik} . Here the index k is run over the neighboring atoms of atoms i and j .

Total bond energy of the system is calculated as half of the sum of U_{ij}^T over all atoms i and j in the system. Only half of the sum is taken to account for double evaluation of each bond energy when indices i and j are switched. Due to the cutoff function f_C , the bond energy is only non-zero for bonds between first nearest-neighbors. Inclusion of the function B_{ij} causes the bond energy to be dependent on characteristics of the local environment such as bond angle, bond length, and number of bonds each atom shares with other neighboring atoms. These properties make the Tersoff potential suitable for modeling materials with

strong covalent bonding [99, 101]. Indeed, one of the earliest parameterizations of the potential offered by Tersoff was for carbon-based materials [100]. Parameters were chosen by fitting to the cohesive energies of carbon systems, as well as the lattice constant and bulk modulus of diamond. The Tersoff potential has been employed to model covalent bonding within CNTs in MD investigations of the intrinsic thermal conductivity of CNTs [18, 28] and thermal conductance at CNT-CNT contacts [7, 91, 92].

Given that thermal conductance between CNTs is achieved through non-bonded van der Waal's interactions, MD studies employing the Tersoff potential to investigate CNT-CNT conductance must also define a second potential to describe these interactions. The LJ potential is typically chosen for this second potential and the implementation of this method to study CNT-CNT conductance is discussed further in Chapter 4. MD simulations employing the Tersoff potential were performed for this dissertation to predict CNT conductivity and CNT-CNT conductance and results are discussed in Sections 3.2.3.3 and 4.2, respectively.

2.2.3 Brenner-II Potential

The original Brenner potential is a bond order potential based on the formulation of Tersoff [99, 100] and developed by Brenner in 1990 [102]. This potential was originally formulated to model hydrocarbons and diamond, and contains additional terms meant to correct the prediction of overbinding of free radicals observed with the Tersoff potential [102]. Brenner et al. made changes to the functional form and parameterization of the original Brenner potential to improve the accuracy of the description of hydrocarbon molecules and various properties of diamond in 2002 [103]. This potential is referred to as the Brenner-II potential throughout this dissertation to avoid confusion with the original formulation. The Brenner-II potential shares a similar functional form and the inclusion of a bond order parameter with the Tersoff potential. The detailed differences between the formulation of each potential can be revealed through comparison of Refs. [99, 100] with

Refs. [102, 103] for the Tersoff and Brenner-II potentials, respectively.

One of the earliest formulations and parameterizations of the Brenner-II potential was for the modeling of covalent carbon-carbon bonds [103]. This formulation was able to describe properties of hydrocarbons and diamond with better accuracy than the original Brenner formulation. However, both the Tersoff and Brenner-II potentials have been found to show limited accuracy in describing the elastic constants [104] and phonon dispersion curves [104, 105] of graphene. The Brenner-II potential has been employed to model covalent bonding within CNTs in MD investigations of the intrinsic thermal conductivity of CNTs [1, 2, 4, 75, 77] and thermal conductance at CNT-CNT contacts [5, 106]. As described in Section 2.2.2, investigation of CNT-CNT conductance requires consideration of the non-bonded van der Waal's interactions between CNTs, which is typically described by the LJ potential. MD simulations employing the Brenner-II potential were performed for this dissertation to predict CNT conductivity. Details of the computational procedure and results are discussed in Chapter 3.

2.3 LAMMPS

The duration of time necessary to perform MD simulations on a given computational resource increases with the number of atoms in the computational domain, which increases with the size of the domain for a constant homogeneous atomic density. As described in Section 2.2, interatomic potentials typically employ a cutoff function which limits the evaluation of interactions for each atom i to some localized region around atom i . While the total number of atomic interactions increases with the size of the sample domain, interactions for each atom i remain spatially localized. Parallelization of MD computational routines exploits this feature by distributing localized calculations of interatomic interactions across multiple central processing units (CPUs), thus decreasing the overall duration of time necessary.

The Large-scale Atomic/Molecular Massively Parallel Simulator (LAMMPS) package is an open-source MD code capable of modeling large numbers of atoms over many CPUs without significant loss of efficiency [107]. LAMMPS uses spatial-decomposition techniques that partition the computational domain into smaller subdomains, each of which has its own dedicated CPU and passes information to other CPUs through the message passing interface (MPI) [108]. The LAMMPS executable is a compiled set of subroutines written in the C++ programming language. Users design unique simulation routines by writing input scripts which load available subroutines and define the required input parameters or variables for computational output. The source code for subroutines may be modified or additional subroutines may be written and implemented by users to allow for customization of the LAMMPS package. The LAMMPS package also contains input files with parameter definitions for the standard formulation of many common interatomic potentials.

The LAMMPS package was used for all MD simulations performed for this dissertation. Each specific computational procedure employed is discussed in detail with the introduction of each simulation series throughout the dissertation. Most simulations used standard LAMMPS subroutines and LAMMPS potential parameter input files with no modification. Modifications were made to the LAMMPS formulation of some potentials in a series of simulations designed to investigate the effects of computational parameters on MD predictions of CNT thermal conductivity. These modifications and the results of this series of simulations are discussed further in Chapter 3.

Chapter 3

CNT Thermal Conductivity

3.1 Background

The thermal conductivity along the CNT axis has been reported to be well over 3000 $\text{Wm}^{-1}\text{K}^{-1}$ [13]. However, with diameters of only a few nanometers and a strong tendency to form bundles and aggregate into intertwined structures, individual CNTs are difficult to isolate and experimentally study in the absence of environmental effects. These difficulties are reflected in the wide discrepancy seen among the results of experimental measurements of individual CNT conductivity [10, 11, 13, 15, 17, 18, 56]. Molecular dynamics (MD) simulations have become a popular method for studying the fundamental properties of CNTs. The strength behind MD simulations is that the only input needed is a definition of the interatomic potential function. This allows the true physics of individual CNTs to be observed in isolation, with minimal assumptions. In addition, the simulated environment can be controlled completely, which eliminates any ambiguity about the physical system being studied.

In spite of the ability of MD simulations to fully control the simulated environment and to provide detailed atomic-level information on the mechanisms responsible for the heat transfer in CNTs, the values of thermal conductivity, k , predicted in different MD simulations exhibit surprisingly large divergence even when the simulated system is nominally the same. For example, a sample of MD results obtained for single-walled CNTs of chi-

Reference	k (Wm ⁻¹ K ⁻¹)	System Length (nm)	Potential	Method	Boundary Conditions
Lukes and Zhong [1]	~20 - 160	5 - 40	Brenner-II + LJ	EMD	periodic and non-periodic
Grujicic et al. [24]	~173 - 179	~2.5 - 40	AIREBO	EMD	periodic
Pan [77]	243	~29.4	Brenner-II	NEMD	periodic
Xu and Buehler [78]	301	49.26	AIREBO	NEMD	periodic
Wei et al. [79]	302	49.26	AIREBO	NEMD	periodic
Che et al. [19]	~240 - 305	~2.5 - 40	Brenner	EMD	periodic
Padgett and Brenner [4]	~35 - 350	~10 - 310	Brenner-II	NEMD	periodic
Thomas et al. [2]	~300 - 365	200 - 1000	Brenner-II	NEMD	non-periodic
Maruyama [21]	~275 - 390	6 - 404	Brenner	NEMD	non-periodic
Shiomi and Maruyama [3, 109]	~130 - 475	~14 - 425	simplified Brenner	NEMD	non-periodic
Feng et al. [75]	~50 - 590	6.52 - 34.77	Brenner-II	NEMD	non-periodic
Bi et al. [28]	~400 - 600	2.5 - 25	Tersoff	EMD	periodic
Cao and Qu [33]	1580	4800	optimized Tersoff	NEMD	periodic
Ren et al. [31]	~1430	~60	AIREBO	NEMD	non-periodic
Berber et al. [18]	~6600	~2.5	Tersoff	HNEMD	periodic

Table 3.1: A sample of the values of CNT thermal conductivity predicted in MD studies reported in the literature. All values are for (10,10) single-walled CNTs at ~300 K. The system length is defined as the total length of the computational system used in the simulations. The nomenclature for the names of the interatomic potentials is explained in the text.

rality (10,10) at ~300 K is listed in Table 3.1. The values of k exhibit variability by more than an order of magnitude, casting doubt on the ability of MD simulations to provide a reliable quantitative estimate of the thermal conductivity. It is important, therefore, to understand the reasons for the data variability across the published studies and, in particular, to evaluate the contributions of two fundamentally different factors: true variation of the intrinsic CNT conductivity due to the variation of length of the CNTs used in the simulations, and variation of k due to variability of computational procedures and interatomic potentials employed in different simulations.

In most CNT-based materials, such as CNT mats, films, buckypaper, and vertically-aligned arrays, the van der Waals attraction between individual nanotubes results in their arrangement into bundles that form entangled continuous networks [14, 48–52]. When CNTs are formed into structures or incorporated into a polymer matrix, the collective thermal conductivity through the CNT network or nanocomposite material is found to be orders

of magnitude lower than the conductivity of the constituent CNTs. It has been previously suggested that the low conductivity of CNT structures is due to the reduction of the intrinsic conductivity of individual CNTs via inter-tube interactions [53–55]. Therefore, a better understanding of the effect of inter-tube interactions on the intrinsic conductivity of individual CNTs is important for the development of CNT-based materials for thermal applications.

Factors that may affect either the intrinsic conductivity of individual CNTs or the value of conductivity predicted by MD simulations are discussed in this chapter. First, background information about these factors is provided in the remainder of Section 3.1. Background information about the sensitivity of CNT conductivity to sample length is presented in Section 3.1.1. A summary of the computational parameters commonly varied in past investigations is given in Section 3.1.2. Further discussion of the effect of inter-tube interactions on CNT conductivity is provided in Section 3.1.3.

Next, the results of a systematic computational evaluation of the sensitivities of the values of thermal conductivity predicted in NEMD simulations to the parameters of the computational setup are reported in Section 3.2. A description of the basic computational procedure is provided in Section 3.2.1, with any variations in the procedure made explicitly known when applicable. The effect of the CNT length is evaluated in Section 3.2.2. Analysis of the sensitivity of the computational predictions to the size and location of the heat bath regions and the choice of interatomic potential is provided in Section 3.2.3. Evaluation of the effect of inter-tube interactions in bundles on the intrinsic conductivity of a CNT is discussed in Section 3.2.4.

3.1.1 Background on the Effect of CNT Length

The length dependence of thermal conductivity of CNTs is commonly observed in MD simulations performed for nanotubes with length up to hundreds of nanometers [1–4, 19, 21, 23–26, 29, 30, 33, 34, 75]. There are two main reasons for this behavior.

First, when the sample length is less than or comparable to the phonon mean free path, phonons are capable of traveling ballistically through the sample without being impeded by phonon-phonon scattering. As the sample length increases, the effective length of this ballistic transport increases, which increases overall thermal transport and results in higher conductivity values. Second, the longest available phonon wavelength that can exist in a CNT is dictated by the sample length. Thus, as the sample length increases, the maximum allowable phonon wavelength increases. The additional long-wavelength phonons offer effective channels for thermal transport and can make a substantial contribution to the thermal conductivity [1, 33]. The CNT length that corresponds to the transition from the ballistic conduction regime, where the thermal conductivity increases with CNT length, to the diffusive regime, where the thermal conductivity approaches a constant value, is temperature dependent as the phonon mean free path decreases with increasing temperature. A recent review of room temperature experimental measurements performed for CNTs with length exceeding $0.5\ \mu\text{m}$ [110] suggests the diffusive regime of the heat transfer. At the same time, the results of MD simulations performed for CNTs with lengths of 10s to 100s of nm typically exhibit a pronounced increase of k with increasing CNT length, that is characteristic of the ballistic and transitional diffusive-ballistic phonon transport [1–4, 21, 23, 26, 29, 30, 33, 75]. The length dependences predicted in different MD studies, however, vary widely for the same (10,10) CNT, with the transition to the diffusive regime (saturation of k) predicted for as short CNTs as 10 nm in some of the investigations [19, 23–25, 34], while no saturation is observed for CNTs with length exceeding $1\ \mu\text{m}$ in other studies [3, 33]. In order to reconcile the diverging results on the CNT length dependence, the sensitivity of the predictions of MD simulations to the interatomic potential and computational procedures used in the calculations of thermal conductivity has to be systematically evaluated.

3.1.2 Background on the Effect of Atomistic Simulation Parameters

The interatomic potential that defines the interaction forces between atoms in the simulated system is a key ingredient of any MD model. The choice of interatomic potential has direct effect on any quantitative prediction of MD simulations, including prediction of the value of thermal conductivity. A sample of results obtained with the interatomic potentials commonly used in simulations of CNTs are listed in Table 3.1. Note that some of the potentials have been modified and different versions and generations of the same potential are concurrently used by different research groups. As a result, there can even be confusion as to the exact version of potential indicated by name in a published work.

For clarity, the following nomenclature convention is defined in this dissertation. The Tersoff potential is the early bond order potential that has the original functional form and parameterization defined by Tersoff in 1988 [99, 100]. The Brenner potential is the potential developed by Brenner in 1990 [102]. Stuart and colleagues modified the Brenner potential, added a description of torsional interactions for rotation about single bonds and developed an adaptive treatment of non-bonded van der Waals interactions within the bond order formalism of the Brenner potential. This potential, described by Stuart et al. in 2000 [111] is referred to as adaptive intermolecular reactive bond order (AIREBO) potential. In 2002, Brenner et al. made changes to the functional form and parameterization of the original Brenner potential to improve the accuracy of the description of hydrocarbon molecules and various properties of diamond [103]. This second-generation Brenner potential is referred to as Brenner-II in this work. A description of van der Waals interactions through simple addition of the Lennard-Jones (LJ) potential to the Tersoff, Brenner, and Brenner-II potentials has also been used in simulations that do not involve formation/dissociation of chemical bonds and do not require adaptive treatment of the intermolecular interactions [1, 74, 112]. These potentials can be denoted as Tersoff + LJ, Brenner + LJ, and Brenner-II + LJ, and a set of parameters ϵ and σ of the Lennard-Jones potential should be provided to define the combined potentials. New sets of parameters for the Tersoff and Brenner

potentials, optimized for the description of phonon thermal transport in carbon nanotubes and graphene, were recently suggested by Lindsay and Broido [105]. These potentials are referred to as optimized Tersoff and optimized Brenner in this work. Finally, Yamaguchi and Maruyama [113] used a simplified version of the original Brenner potential, in which the conjugate-compensation term is eliminated to facilitate the formation of poly-cyclic structures in simulations of fullerene formation process. This implementation was used by Shiomi and Maruyama [3] in simulations of thermal conductivity of CNTs and is referred to as simplified Brenner in this dissertation.

Another factor that may be responsible for the inconsistency of the computational predictions is the variability of the methods employed for the calculation of thermal conductivity in MD simulations. Two general types of methods are used in the analysis of thermal transport properties. In the equilibrium molecular dynamics (EMD) method, small fluctuations of heat current are monitored over time and Green-Kubo relation is used to determine the thermal conductivity from these perturbations from equilibrium [1, 19, 24, 28]. While periodic boundary conditions are often used in EMD calculations to represent an infinitely long CNT [18, 114], the results of the calculations show an increase in the conductivity with increasing length of the computational cell [1, 19, 24, 25, 34, 74].

In the non-equilibrium molecular dynamics (NEMD) method, a steady-state temperature gradient is created between “heat bath” regions defined in the system and the thermal conductivity is determined from the Fourier law. The heat flux can be applied directly or indirectly by prescribing either the energy flux or temperature gradient. The NEMD studies referenced in Table 3.1 provide examples of the different approaches to creating a temperature gradient. In particular, Thomas et al. [2] and Cao and Qu [33] directly applied an energy flux by removing a known amount of kinetic energy from a cold heat bath region in a CNT and adding it to a hot heat bath region to impart a flux between the two regions. Maruyama [21], Shiomi and Maruyama [3], Feng et al. [75], and Ren et al. [31] directly applied the temperature gradient by fixing the temperatures of the heat bath regions on both

sides of the CNT. Finally, Pan [29], Xu and Buehler [78], Wei et al. [79], and Padgett and Brenner [4] indirectly applied a heat flux by periodically exchanging the momenta between the slowest atom in the hot heat bath region and the fastest atom in the cold heat bath region. The boundary conditions applied at the ends of the computational system are also varied across NEMD simulations and include free boundary conditions applied to CNTs ends [26, 73], rigid boundary conditions with heat bath regions immediately adjacent to the fixed ends of the CNT [2, 75, 82] or separated from the fixed ends by an intermediate layer [31, 115], and periodic boundary conditions applied along the axis of the CNT [4, 20, 23, 30, 33, 77–79]. In the case of the periodic boundary conditions, the distance between the centers of the hot and cold heat bath regions has to be twice shorter than the total length of the computational domain to satisfy the requirement of periodicity of the temperature distribution.

The diversity of methods and types of boundary conditions results in the ambiguity of the definition of the CNT length. In the EMD method, there are no heat bath regions, and the computational cell can be considered to represent the actual CNT length if free boundary conditions are used [1] or an infinite CNT in the case of periodic boundary conditions, with longer cells providing a more accurate representation [25]. In the NEMD method, when the heat bath regions are employed, it is common to consider the CNT length to be the unperturbed length between the two heat bath regions [2, 3, 72, 80]. However, the thermally controlled regions can also be included in the definition of CNT length, particularly in works employing the NEMD method with periodic boundary conditions [4, 23, 33]. Furthermore, in the case when the periodic boundary conditions are used, the CNT length can be defined as the overall length of the computational cell [23, 29, 78] or the twice shorter distance between the centers of the heat bath regions [30, 33]. This variation in CNT length definitions is addressed in Section 3.2.3.2 in further detail. For the purposes of Table 3.1, the system length refers to the length of the entire computational domain for all works.

The brief review of computational work provided above suggests that the results of

the MD calculations of thermal conductivity are significantly affected by the choice of interatomic potential, computational method, boundary conditions, and definition of the effective CNT length. While the sensitivity of the predictions of MD simulations to the choice of the computational setup is generally recognized [1, 2, 33, 74, 79, 110], there has been no targeted studies aimed at systematic evaluation of the relative effect of various computational parameters on the CNT conductivity values. Understanding of the extent to which the computational parameters affect the predicted values of thermal conductivity is necessary not only for resolving the discrepancies in the reported results of MD studies, but also for investigation of any real effects of the CNT length or physical environment, in isolation of any artifacts of the computational setup.

3.1.3 Background on the Effect of Inter-Tube Interactions in Bundles

The experimental values of conductivity of CNT bundles span a discouragingly broad range, from less than $10 \text{ Wm}^{-1}\text{K}^{-1}$ (e.g., Refs. 116 and 117) up to more than a thousand of $\text{Wm}^{-1}\text{K}^{-1}$ (Ref. 118). The large variability of the experimental values may be attributed to the differences in the measurement techniques, thickness, packing density and structural parameters of the bundles, concentration of intrinsic defects in the CNTs and inter-CNT cross-links, as well as inclusions of graphitic fragments, residual solvent or catalyst nanoparticles. The lowest values of $3\text{--}9 \text{ Wm}^{-1}\text{K}^{-1}$ are reported for relatively thick (on the order of $100 \mu\text{m}$) “bundles” of multi-walled CNTs with packing density that is typical for vertically aligned arrays of CNTs [116, 117]. Higher thermal conductivity, up to $253 \text{ Wm}^{-1}\text{K}^{-1}$, is measured by a non-contact two-laser optical technique for thin (10–12 nm in diameter) bundles consisting of 4–7 single-walled CNTs [119, 120]. Similar room-temperature conductivity of $\sim 150 \text{ Wm}^{-1}\text{K}^{-1}$ is obtained for a 10 nm bundle of single-walled CNTs by contact measurements performed on a microfabricated device in Ref. 53, although a very low value of several $\text{Wm}^{-1}\text{K}^{-1}$ is reported in this work for a thicker bundle of 148 nm in diameter. The conductivity measured in Ref. 54 for dense

bundles consisting of tens to hundreds of well-aligned multi-walled CNTs (diameter of up to 200 nm), is found to drop from about 400 to 150 $\text{Wm}^{-1}\text{K}^{-1}$ as the size of the bundle increases. Even stronger thickness dependence is observed for bundles of multi-walled CNTs in Ref. 118, where the room-temperature thermal conductivity is reported to drop from $\sim 1200 \text{ Wm}^{-1}\text{K}^{-1}$ to $\sim 250 \text{ Wm}^{-1}\text{K}^{-1}$ as the bundle diameter increases from 80 to 200 nm.

The decrease of the thermal conductivity with increasing number of CNTs in the bundles [53, 54, 118] and, more generally, much lower thermal conductivity of bundles as compared to individual CNTs (experiments performed for suspended CNTs yield room temperature values that are ranging from 1400 $\text{Wm}^{-1}\text{K}^{-1}$ to 3000 $\text{Wm}^{-1}\text{K}^{-1}$ for multi-walled CNTs [11, 17, 66, 118] and are even higher values for single-walled CNTs [13, 17]) are commonly attributed to the van der Waals inter-tube interactions in the bundles and associated enhanced phonon scattering [36, 53–55, 120]. The reduction of the intrinsic thermal conductivity of CNTs and other carbon structures due to the non-bonding interactions in materials that consist of multiple structural elements was suggested by Berber *et al.* [18] based on the results of atomistic Green-Kubo calculations of thermal conductivity. This suggestion, however, while echoed in a number of works, e.g., Refs. 36, 53–55, 121, is only a conjecture extrapolated from the computational prediction on the difference between the thermal conductivity of a graphene monolayer and graphite. A notion of a weak effect of the interactions of perfect (defect-free) CNTs in a bundle on thermal conductivity, which can be substantially enhanced by structural defects, has been put forward in Ref. 122 based on the kinetic model calculations of thermal conductivity. Resolving any uncertainty regarding the effect of neighboring CNT interactions on the intrinsic conductivity of CNTs is important to understanding thermal transport in CNT based materials and is one of the objectives of the computational study reported in the next section.

3.2 Computational Results

The results of a systematic evaluation of the sensitivity of the values of thermal conductivity predicted in NEMD simulations to inter-tube interactions and the computational parameters commonly varied in past investigations are reported in this section. A description of the general computational procedure is provided in Section 3.2.1. Some modifications to this basic procedure were made for some of the simulations and are explicitly explained when applicable. The effect of the CNT length is evaluated in Section 3.2.2. Analysis of the sensitivity of the computational predictions to the size and location of the heat bath regions and the choice of interatomic potential is provided in Section 3.2.3. Evaluation of the effect of inter-tube interactions is discussed in Section 3.2.4.

3.2.1 General Computational Procedure

Simulations discussed in Sections 3.2.2 and 3.2.3 are designed to predict the thermal conductivity of individual (isolated) CNTs. While some procedures are varied across different series of simulations, the basic sample preparation and computational procedure are common to all of the simulations discussed in these sections and are outlined below in this section. Simulations discussed in Section 3.2.4 are designed to predict the thermal conductivity of individual CNTs in bundles. The computational procedure for these simulations differs somewhat from the procedure presented in this section and is discussed in detail in Section 3.2.4.

Simulations are performed for (10,10) CNTs covered by 110-atom caps at the ends, with one of the caps interfacing with the CNT by a 20-atom ring constituting a half of the nanotube's unit cell. Free (vacuum) boundary conditions are applied in all directions. Initially, all CNTs undergo relaxation for 25 to 100 ps in constant energy MD simulations. Next, the CNTs are gradually heated up to 300 K over the course of 20 to 50 ps using the Langevin thermostat method [123], while ensuring that the total linear and angular mo-

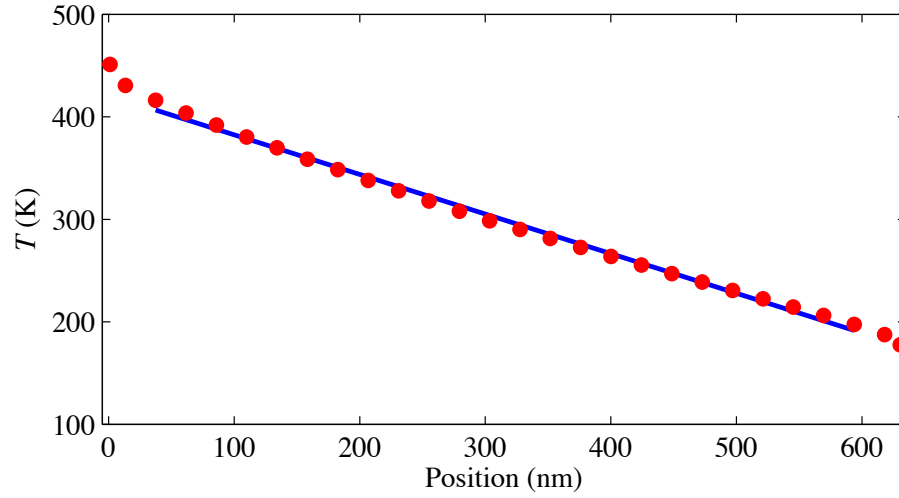


Figure 3.1: A representative steady-state temperature profile obtained in a simulation performed for a 630 nm long (10,10) CNT. The data points are calculated for ~ 24.2 nm segments along the CNT. The line is a linear fit that is used in the calculation of the temperature gradient. The fit excludes the data points that correspond to the heat bath regions and first points adjacent to the heat bath regions.

menta of the CNTs are zero [1]. After the heating process, an additional 20 ps relaxation in constant-energy free dynamic simulations is employed to monitor the CNT system coordinates and energies, and to verify that mechanical-vibrational equilibration is achieved after the temperature increase.

The thermal conductivity of CNTs is determined in NEMD simulations by generating constant heat flux between hot and cold bath regions defined in the CNTs. The heat flux is applied by adding a fixed amount of energy at a constant rate through scaling the velocities of atoms in the heat bath regions so that the same amount of energy, Q_{HB} , is added and removed per unit time in the hot and cold heat bath regions, respectively. This creates a constant one-dimensional heat flux, $q = Q_{HB}/\Omega$, between the heat bath regions, where Ω is the cross-sectional area of the CNT, defined in this work as $\Omega = 2\pi\delta_T R_T = 1.43 \text{ nm}^2$, $R_T = 0.67 \text{ nm}$ is the nanotube radius found in MD simulations as the average radial distance of carbon atoms from the axis of an isolated CNT equilibrated at 300 K, and $\delta_T = 0.34 \text{ nm}$ is the nominal thickness of the CNT wall taken to be equal to the interlayer spacing in graphite [21, 47, 83].

The applied flux creates a non-equilibrium temperature profile in the sample, which is determined by the flux and conductivity of the CNT. The temperature profile is obtained by dividing the nanotube into segments and calculating local temperature of each segment from the average kinetic energy of the corresponding atoms,

$$T_j = \frac{1}{3k_B N_S} \sum_{i \in S_j} m v_i^2, \quad (3.1)$$

where T_j is the temperature of segment j , N_S is the number of atoms in a segment, v_i is the instantaneous velocity of atom i , m is the atomic mass, k_B is the Boltzmann constant, and the summation is performed over atoms that belong to segment j . A representative temperature profile generated for a 630 nm CNT, divided into ~ 24.2 nm segments is shown in Fig. 3.1. The bath regions were 0.5 nm wide, and positioned ~ 1 nm from the extreme ends of the tube, to exclude the fullerene caps. The temperature gradient, dT/dx , is determined from a linear fit applied to the temperature profile, with non-linear parts of the temperature distribution adjacent to the heat bath regions excluded from the fitting procedure.

Once the temperature gradient is found, the CNT conductivity can be calculated from the Fourier law, $k = -q/(dT/dx)$. One of the most important requirements of the NEMD method is to ensure that the system has reached the steady state. During the time of the simulation with the flux implemented, the temperature gradient evolves from zero to the final steady-state value. Measuring the temperature gradient before steady-state temperature profile is established will result in an over-prediction of the CNT conductivity. To ensure the system has reached the steady state, a moving average of thermal conductivity over a fixed temporal window is monitored. Temperature profiles are averaged over the moving time window throughout the simulation and a moving temporal average of the conductivity is obtained. The evolution of the conductivity averaged over the moving time interval is used to determine when the steady-state temperature gradient is established in the system. All data for times after the steady state was reached are averaged in calculation of the final

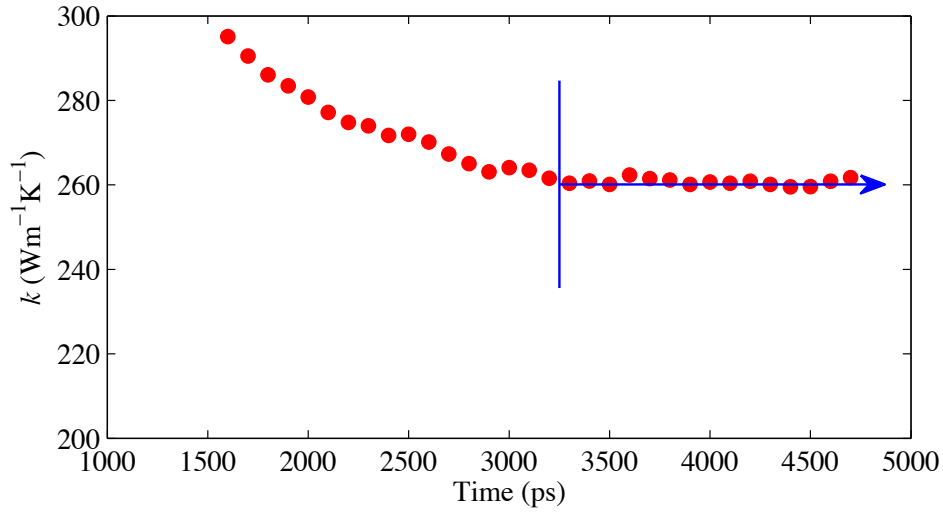


Figure 3.2: A representative plot of the time evolution of thermal conductivity, k , calculated from temperature profiles averaged over a moving 100 ps temporal window in a simulation of heat flow through a 630 nm long (10,10) CNT. The steady state is deemed to be reached by the time of 3250 ps (marked by the vertical line) and the final value of k is determined by averaging all data obtained within the time interval indicated by the horizontal arrow.

value of thermal conductivity.

A representative temporal conductivity plot calculated for the same 630 nm long CNT used for the illustration of the temperature profile in Fig. 3.1 is shown in Fig. 3.2. In this example, data was recorded every 0.005 ps and averaged over a 100 ps temporal window. The initial values of thermal conductivity calculated at the start of the constant heat flux simulation are much higher than the final values, and are not shown in this figure. As the simulation progresses, the conductivity decays to a steady-state value. After 3250 ps, the temporal decay of conductivity ceases and the temporal variation of the conductivity values can be attributed to statistical fluctuations about an average value. The final value of the thermal conductivity is obtained by averaging over the steady-state part of the simulation as schematically shown by the horizontal arrow in Fig. 3.2.

All simulations reported in this dissertation are performed with the LAMMPS package [107]. The equations of motion are solved using the velocity Verlet algorithm and the timestep of integration is 0.5 fs. In the simulations presented in Sections 3.2.2, 3.2.3.1, and 3.2.3.2, interatomic interactions are described with the LAMMPS implementation of the

AIREBO potential [111] that adopts the Brenner-II potential [103] for chemically bonded carbon atoms and describes the van der Waals interactions between non-bonded carbon atoms by the Lennard-Jones potential with parameters $\sigma = 3.40 \text{ \AA}$ and $\epsilon = 2.84 \text{ meV}$. A cutoff function that ensures a smooth transition of the Lennard-Jones potential to zero is applied in a range of interatomic distances from 2.16σ to 3σ . In Section 3.2.3.3, the effect of the choice of interatomic potential on the value of thermal conductivity predicted in NEMD is analyzed by performing additional simulations with Tersoff [100], Brenner-II [103], LAMMPS implementation of AIREBO [111], and optimized Tersoff [105] potentials.

3.2.2 Effect of CNT Length

A series of simulations was performed to examine the length dependence of CNT conductivity. The CNT length was varied between 47 and 630 nm (8,240 to 104,440 atoms, respectively). Following a common convention adopted in many NEMD studies of thermal conductivity, e.g., [2, 3, 72, 73, 80, 124, 125], the CNT length is defined as the length of a central unperturbed part of the tube, L_C , located between the 0.5 nm wide hot and cold heat baths regions. The results of the calculations of thermal conductivity plotted as a function of L_C are shown in Fig. 3.3. The strong length dependence observed for CNTs shorter than $\sim 200 \text{ nm}$ suggests the dominant contribution from ballistic phonon transport. For lengths greater than $\sim 200 \text{ nm}$, the dependence on CNT length becomes weaker. This marks the transition to the diffusive-ballistic regime and indicates that the sample length that corresponds to the onset of this transition is on the order of the effective phonon mean free path [126]. Note that the extent of the transitional diffusive-ballistic regime is defined by the longest mean free paths of long-wavelength phonons (of the order of several μm at room temperature [127]) that dominate the heat transfer in CNTs. Thus, while the dependence predicted in our simulations becomes notably weaker and shows signs of saturation as the length increases to 630 nm, the gradual increase of the thermal conductivity with increasing

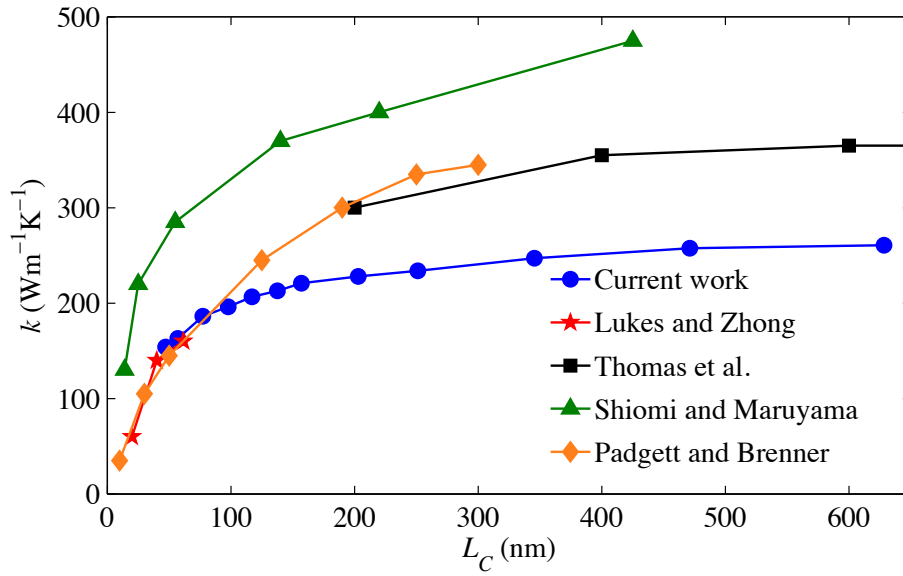


Figure 3.3: Thermal conductivity, k , of (10,10) CNTs as a function of sample length, L_C , defined as the distance between the hot and cold heat bath regions. For comparison, the length dependencies of thermal conductivity reported by Lukes and Zhong [1], Thomas et al. [2], Shiomi and Maruyama [3], and Padgett and Brenner [4] are also plotted. While quantitative discrepancies are present, all sets of data exhibit a consistent trend of strong length dependence for short CNTs transforming to weaker increase for CNTs that are longer than ~ 200 nm, thus signifying the transition from the ballistic to diffusive-ballistic heat transport regimes.

length may be expected up to CNT lengths of the order of tens of μm [128, 129].

For comparison, the results of other NEMD studies that report CNT length dependence of thermal conductivity [1–4] are also plotted in Fig. 3.3. While the predicted values of conductivity vary across these works, the qualitative trends in the length dependencies are similar. For CNTs with lengths shorter than 200 nm, all studies predict a strong length dependence of the conductivity, characteristic of dominant ballistic thermal transport. In studies where CNTs longer than 200 nm are investigated, a transition to a weaker length dependence and saturation of the conductivity values with increasing nanotube length is observed, suggesting a transition to the diffusive-ballistic regime. The transition between the two regimes is observed for nanotube length that roughly corresponds to the room temperature phonon mean free path that has been estimated to be of the order of 200-500 nm based on experimental data [10, 13], results of recent NEMD simulations [33] and

theoretical analysis [126].

The strong sensitivity of the thermal conductivity to the CNT length predicted in NEMD simulations demonstrates that quantitative comparison between the results of different simulations should account for the length dependence, especially when the results are compared for short CNTs, in the ballistic heat transport regime. Apart from the length dependence, the factors responsible for the apparent quantitative discrepancies in data obtained in different simulations illustrated in Fig. 3.3 are investigated and discussed in Section 3.2.3.

3.2.3 Effect of Atomistic Simulation Parameters

The results summarized in Fig. 3.3 demonstrate large discrepancies in quantitative results obtained in different studies. It is reasonable to assume that the differences in the computational setups used in different studies are to blame for the discrepancies in the results. There have been no systematic studies, however, reported on the effect of various parameters on the values of thermal conductivity predicted in NEMD simulations. Therefore, this section describes the results of several series of simulations targeted specifically at revealing the effect of some of the key simulation parameters on the predictions of CNT thermal conductivity. The conclusions of this study provide both insights into the nature of the nanoscale thermal transport in CNTs and recommendations on the choice of the computational parameters that may lead to the reduction in the discrepancies between the results of different simulations.

3.2.3.1 Heat Bath Length

When employing the NEMD method described in Section 3.2.1 to study thermal conductivity of CNTs in the ballistic regime, the length of the two heat bath regions, $2L_B$, can account for a substantial portion of the overall system length, L_{sys} , as measured from end to end, Fig. 3.4. In most NEMD studies employing non-periodic (rigid or free) boundary conditions, however, the CNT length is defined as the length between the inner bound-

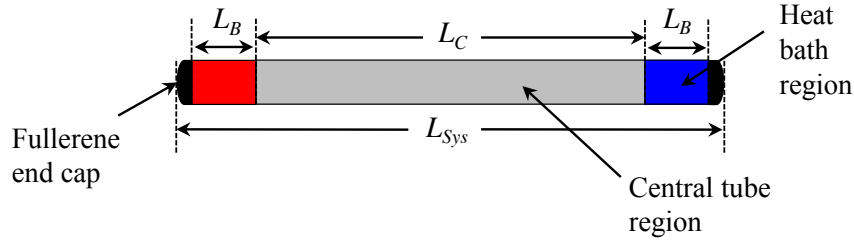


Figure 3.4: A schematic of a computational setup used in NEMD simulations of thermal conductivity of CNTs and the definitions of the length parameters. Two heat bath regions of length L_B are separated by a central tube region of length L_C .

aries of the heat bath regions, or the length of the central part of the nanotube, L_C , e.g., [2, 3, 72, 73, 80, 124, 125]. This definition of sample length is not limited to CNTs but is commonly applied in NEMD investigations of various materials [130–132]. The effect of the length of the heat baths is implicitly assumed to be negligible in most of these studies employing this definition of sample length. This assumption is challenged, however, by the results of two studies [3, 72] where the effect of L_B on k is analyzed. The simulations performed for CNTs with fixed size of the central region L_C but varied length L_B of Nose-Hoover thermostats applied to the heat bath regions demonstrate that the value of k has a pronounced dependence on L_B .

Shiomi and Maruyama [3] attributed this behavior to a thermal boundary resistance (TBR) present between each of the heat bath regions and the central tube region. According to this explanation, a difference between the bath length and the central tube length results in a difference in allowable phonon states in each of these regions. This mismatch in phonon states, and the resulting TBR, cause an abrupt temperature change at the interface between the central and heat bath regions, and thus affect the final steady-state temperature gradient used in the calculation of the conductivity. They concluded that this effect can be minimized when the length of the heat bath regions is equal to the central tube length, *i.e.*, $L_B = L_C$. Based on this conclusion, Shiomi and Maruyama suggest that a bath region with length equal to half the length of the central tube region, $L_B = L_C/2$, should be used

as an optimal choice that ensures a sufficient reduction of the TBR effect at a reasonable computational cost.

To further examine the effect of the length of the heat bath regions, two series of NEMD simulations were performed. In both series (10,10) CNTs covered by fullerene caps at the two ends are used. In the first series, Series 1, the distance between the heat bath regions was fixed at $L_C = 50$ nm while the length of each heat bath region was varied within a range from $L_B = 0.5$ nm to $L_B = 75$ nm. In the second series of simulations, Series 2, the central tube length was fixed at $L_C = 97$ nm and the length of the heat bath regions was varied from $L_B = 25$ nm to $L_B = 150$ nm. The two sets of parameters are chosen to allow for analysis of the effect of the length of the heat bath regions for the conditions when the bath regions are both shorter and longer than the central parts of the nanotubes. The calculations of the thermal conductivity follow the general procedure described in Section 3.2.1. The heat flux is maintained by adding/removing the kinetic energy in the heat bath regions at rates of $Q_{HB} = 0.45$ eV/ps for $L_C = 50$ nm (Series 1) and $Q_{HB} = 1.25$ eV/ps for $L_C = 97$ nm (Series 2).

Additional analysis was performed to estimate the standard error of the mean conductivity. After achievement of the steady state, calculations of conductivity are continued for an additional 2500 ps for Series 1 and 500 ps for Series 2. For each simulation, the data obtained in the steady state are divided into N sample sets, each with M conductivity calculations. The sample mean of each sample set, k_i , is calculated to provide N estimations of the true mean conductivity predicted in the NEMD simulation. The final value of the conductivity reported is the mean of the N estimations, \bar{k} . Averaging over M measurements in each sample set reduces the effect of the natural statistical fluctuations in instantaneous temperature profiles that arise due to the relatively small number of atoms in each CNT segment and provides a more accurate estimation of the mean conductivity. This method produces a sample of N independent estimations of the mean conductivity and is used to estimate the standard error of the mean [133]. The sample standard deviation, S , is deter-

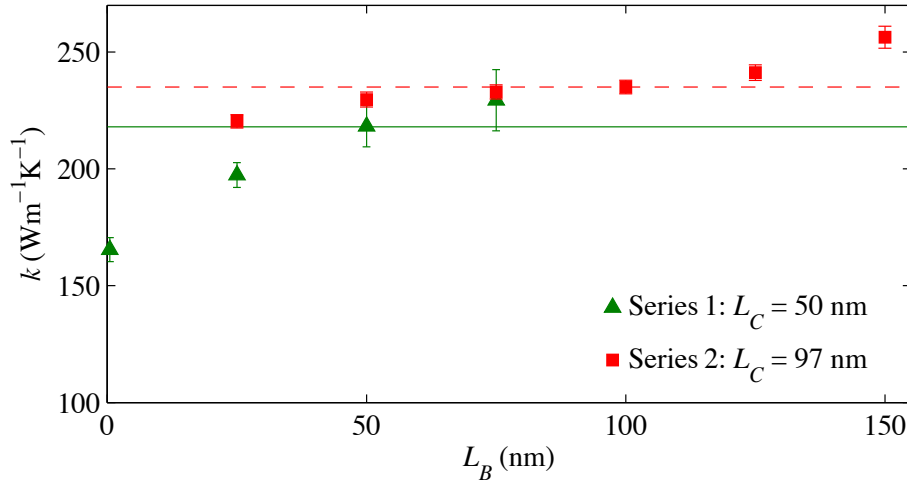


Figure 3.5: Thermal conductivity, k , as a function of the length of the heat bath regions, L_B . The results are shown for two series of NEMD simulations performed with fixed distance between the heat bath regions: in Series 1 (green triangles) $L_C = 50$ nm and in Series 2 (red squares) $L_C = 97$ nm. The error bars show the estimates of the standard error of the mean, with some error bars obscured by the width of the data points. The solid green and dashed red lines mark the values of k predicted in simulations of Series 1 with $L_B = L_C = 50$ nm and Series 2 with $L_C \approx L_B = 100$ nm, respectively. The consistent trend of increasing thermal conductivity for $L_B > L_C$ contradicts the notion that the sensitivity of the results to L_B is due to the thermal boundary resistance at the boundaries of the heat bath regions.

mined as

$$S = \left(\frac{1}{N} \sum_{i=1}^N (k_i - \bar{k})^2 \right)^{1/2}, \quad (3.2)$$

and the estimated standard error of the mean is calculated by $\hat{\sigma}_{\bar{k}} = S/\sqrt{N}$. This value provides a measure of the precision in estimating the mean conductivity predicted by the NEMD simulations.

The results of the two series of simulations plotted as a function of L_B are shown in Fig. 3.5. The data represented by green triangles are the results for Series 1, where the central tube length was $L_C = 50$ nm, and the data represented by red squares are the results for Series 2, where the central tube length was $L_C = 97$ nm. The error bars represent the estimates of the standard error of the mean conductivity predicted in the simulations. In both series of simulations, the conductivity shows a strong dependence on the length of the heat bath regions. The values predicted in the simulations range from $165 \text{ Wm}^{-1}\text{K}^{-1}$

to $229 \text{ Wm}^{-1}\text{K}^{-1}$ and from $220 \text{ Wm}^{-1}\text{K}^{-1}$ to $256 \text{ Wm}^{-1}\text{K}^{-1}$ for Series 1 and Series 2, respectively. These are significant variations, particularly in light of the common practice of defining CNT length as the distance between the inner boundaries of the two heat bath regions and the lack of a rigorous criterion for choosing the length of the heat bath regions. In the case of Series 1, for example, the results imply up to 39% variation in the conductivity values predicted for a 50 nm CNT, depending on the choice of the length of the heat bath regions, L_B .

It is also instructive to compare the results of the two series of simulations performed with fixed values of L_C with the data used in Section 3.2.2 to examine the length dependence of k . In this additional series of simulations, Series 3, the length of the heat bath regions was kept constant at $L_B = 0.5 \text{ nm}$, and L_C was varied from 47 nm to 630 nm. In Fig. 3.6a, all data is plotted as a function of L_C , which is a standard way to define the CNT length in the NEMD length dependence studies employing non-periodic boundary conditions [2, 3, 72, 73, 80, 124, 125]. In this representation, we can see that the variations of the values of k in the constant L_C series (Series 1 and 2) are comparable to the range of values obtained by changing L_C in Series 3.

Perhaps a more significant aspect of Fig. 3.5 is that the values of thermal conductivity predicted in the Series 1 and 2 simulations continue to increase with increasing lengths of the heat bath regions even for $L_B > L_C$. The solid green and dashed red lines in Fig. 3.5 mark the values of k predicted in simulations of Series 1 with $L_B = L_C = 50 \text{ nm}$ and Series 2 with $L_B \approx L_C$ ($L_B = 100 \text{ nm}$, $L_C = 97 \text{ nm}$), respectively. According to the interpretation offered by Shiomi and Maruyama [3], TBR between the heat bath regions and the central region of the unconstrained dynamics should reach a minimum for $L_B = L_C$ and the thermal conductivity should not increase with further increase of the heat bath length. The continued increase in the conductivity for the bath lengths $L_B > L_C$ suggests that the interpretation based on the TBR caused by the mismatch of the vibrational spectra of the heat bath regions and the central part of the CNT has to be reconsidered.

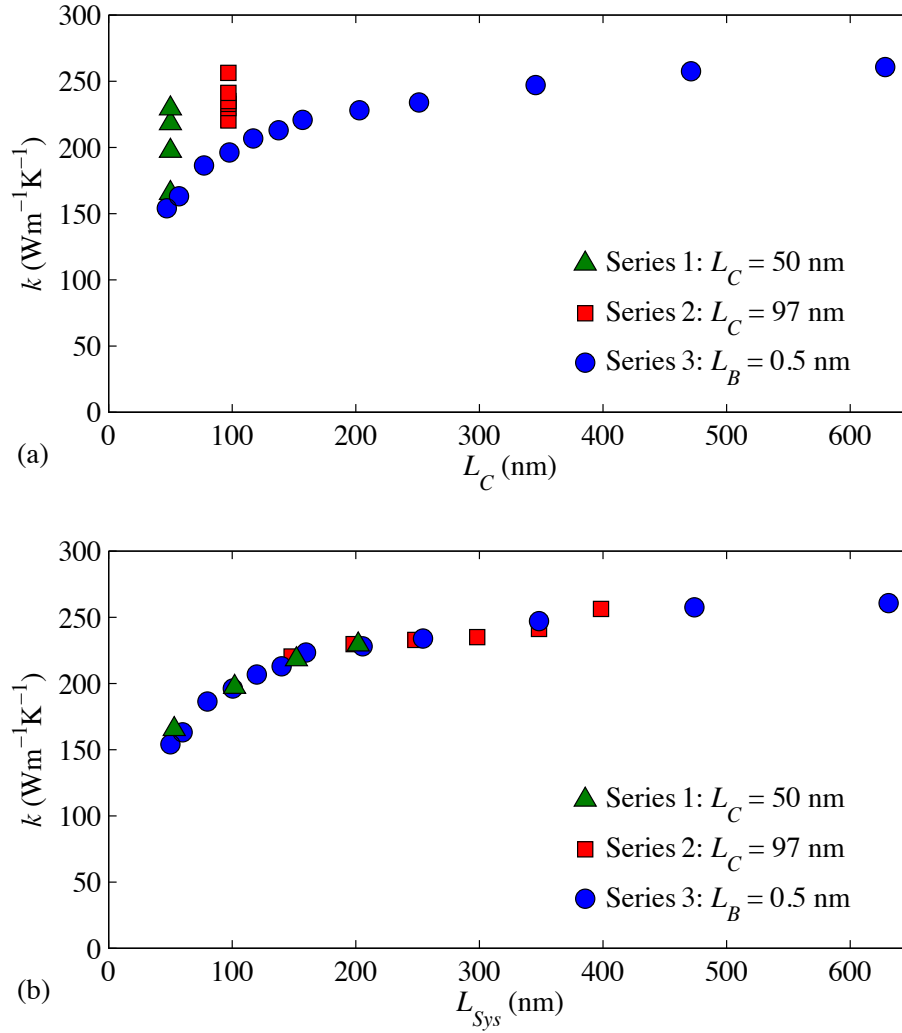


Figure 3.6: Thermal conductivity, k , as a function of (a) length of the central part of the CNT, L_C , and (b) the total length of the CNT, L_{Sys} . The results are shown for three series of NEMD simulations: in Series 1 (green triangles) CNTs have fixed $L_C = 50$ nm and varied L_B , in Series 2 (red squares) CNTs have fixed $L_C = 97$ nm and varied L_B , and in Series 3 (blue circles) CNTs have fixed $L_B = 0.5$ nm and varied L_C . While it is common to use L_C as a measure of the effective CNT length in NEMD simulations of thermal conductivity, plotting k versus L_{Sys} in (b) provides a more consistent representation of the length dependence of k across all series of simulations, regardless of whether the length is added to the central region (Series 3) or the bath regions (Series 1 and 2) of the nanotube.

	k (Wm ⁻¹ K ⁻¹)	L_{Sys} (nm)	L_C (nm)
Series 1	229	202	50
Series 2	230	198	97
Series 3	228	206	203

Table 3.2: Sample data taken from Fig. 3.6. Overall system length, L_{Sys} , which includes the heat bath regions, is found to be a better predictor of conductivity than the distance between the heat bath regions, L_C .

The results of the present simulations suggest that the length dependence of thermal conductivity predicted in NEMD simulations is most adequately described as the dependence on the overall (end-to-end) length of the system, L_{Sys} . The nature of this dependence is illustrated in Fig. 3.6b, where the exact same data from Fig. 3.6a is re-plotted as a function of the overall system length, L_{Sys} . A striking observation from this plot is that when the results from the three series of simulations are plotted with respect to L_{Sys} , the effect of increasing L_B in Series 1 and 2 is nearly *indistinguishable* from the effect of increasing L_C in Series 3. A near coincidence of the three points at $L_{Sys} \approx 200$ nm in Fig. 3.6b is a good illustration of this observation. The similarity of the values of k predicted in the three series of simulations and listed in Table 3.2 is consistent with the notion that the overall system length determines the value of the thermal conductivity. These CNTs, however, would be considered to have very different lengths by the common definition of CNT length as the length of the central part of the nanotube, L_C .

The length dependence of the thermal conductivity obtained in the simulations can be extrapolated to samples of infinite length to obtain an estimate of the thermal conductivity, k_∞ . From the kinetic theory for a phonon gas, the thermal conductivity can be related to the phonon mean free path as

$$k = \frac{1}{3}cvl_{eff}, \quad (3.3)$$

where c is the phonon heat capacity per unit volume, v is the average phonon velocity, and l_{eff} is the effective mean free path of the phonons. In a CNT of a finite length, the effective mean free path is defined by both the phonon-phonon scattering and the phonon scattering

at the boundaries of the CNT. Using Matthiessen's rule for independent contributions of the two scattering mechanisms, the effective mean free path can be written as

$$\frac{1}{l_{eff}} = \frac{1}{l_{\infty}} + \frac{2}{L_{Sys}}, \quad (3.4)$$

where l_{∞} is the mean free path of phonons in the system where $L_{Sys} \rightarrow \infty$. From Eqs. 3.3 and 3.4, it follows that the length dependence of the thermal conductivity can be written as [134, 135]

$$\frac{1}{k} = \frac{A}{2l_{\infty}} + \frac{A}{L_{Sys}}, \quad (3.5)$$

where A is a constant that defines the slope of the linear dependence of $1/k$ on $1/L_{Sys}$. The estimates of the phonon mean free path and thermal conductivity in an infinitely long CNT, l_{∞} and k_{∞} , can then be obtained by plotting the dependence of $1/k$ on $1/L_{Sys}$ predicted in NEMD simulations and extrapolating it to $L_{Sys} \rightarrow \infty$. Note that this linear extrapolation procedure provides only the first order approximation of the values l_{∞} and k_{∞} . The variability of the phonon group velocities and mean free paths [127], neglected in the simple Eq. 3.3, may result in substantial deviations from the linear dependence of $1/k$ on $1/L_{Sys}$ [2, 132]. However, a linear relationship was observed for the range of system lengths investigated in this study.

The values of l_{∞} and k_{∞} obtained by the procedure outlined above for the three series of simulations are listed in Table 3.3. The conditions of simulations of Series 3, where the size of the heat bath regions is kept constant while L_C is increased, are the closest reflection of the true physical system of interest. Thus, one can expect that the most accurate prediction of k_{∞} would come from the application of the extrapolation procedure to data produced in this series. The extrapolation of data from Series 1 and 2, where L_C is kept constant and L_B increases, can be represented by a CNT with a fixed length of the central part of the nanotube, but infinitely-long bath regions. It is clear that this representation does not match the true physical system of interest when considering the conductivity of infinite systems.

	L_C (nm)	L_B (nm)	k_∞ (Wm ⁻¹ K ⁻¹)	l_∞ (nm)
Series 1	50	∞	263	16
Series 2	97	∞	267	16
Series 3	∞	0.5	275	20

Table 3.3: The upper saturation limit of conductivity, k_∞ , and phonon mean free path, l_∞ , predicted by fitting the results of NEMD simulations to Eq. 3.5. The values of L_C and L_B correspond to systems extrapolated to infinite overall length, L_{Sys} , by following the procedures of the three series of simulations. Series 3 provides the most realistic representation of the true system of interest, with length added to the central region of the nanotube. Despite length being added to the heat bath regions while L_C is kept constant, Series 1 and 2 provide estimates of k_∞ that are surprisingly close to the more realistic prediction of Series 3.

While the highest prediction comes from extrapolation of the results of Series 3, it can be seen that the extrapolated values for $L_B \rightarrow \infty$ are similar to the one obtained for $L_C \rightarrow \infty$ and the agreement improves as L_C increases from 50 nm to 97 nm.

The main conclusion drawn from Fig. 3.6 is that the length dependence of CNT conductivity is better captured by the overall system length, L_{Sys} , than by the length of the central part of the nanotube, L_C . The length of the heat bath, L_B , is shown to have a strong effect on the values of k predicted in NEMD calculations for CNT lengths comparable to the phonon mean free path. This length dependence is nearly indistinguishable from the dependence on L_{Sys} and the agreement improves as L_C increases from 50 nm to 97 nm. This suggests that the contribution to thermal conductivity from L_B is similar to the contribution from L_C . It follows that bath regions of any significant length should be considered to be parts of the nanotube, and the CNT length should be defined as the length of the overall system, L_{Sys} . Physically, these results imply a relatively minor contribution of the phonon scattering at the interface between the heat bath regions and the unperturbed region of the system to the overall length dependence of the thermal conductivity. The dominant contribution is coming from the real boundaries of the sample, which scatter phonons and limit the maximum phonon wavelength that can exist in the nanotube.

Although the length dependencies shown in Fig. 3.6b for the three series of simulations are similar, the extrapolated values obtained by increasing L_B do not exactly reproduce the

values obtained by increasing L_C , as seen in Table 3.3. Therefore, the choice of a small bath length would be optimal for obtaining an accurate prediction of the length dependence of k and the extrapolated value of k_∞ . Overall, the results of the analysis discussed above provide guidance for choosing a simulation setup that best represents the conductivity of a system of interest. CNT length definition should *include* the heat bath regions, and the length of the heat bath regions should be small compared to the total length of the system. It is worth noting that the underlying physics of the effects of thermal bath length is applicable to phonon thermal transport in the ballistic-diffusive length regime of any material. Thus this definition of CNT length can be extended to the definition of sample length in any NEMD study of thermal transport.

3.2.3.2 Computational Configuration

The variation of computational setups used for the generation of steady-state heat fluxes in NEMD simulations could be an additional source of the discrepancies in the computational predictions. There are two commonly used ways of implementing the heat flux. In all simulations discussed in the previous sections of this chapter, the temperature or heat flux control is applied to the two heat bath regions located at the ends of a CNT and a steady-state heat flux is created in the central part of the CNT, between the two heat bath regions. Fig. 3.4 represents a schematic of this computational setup. This method of applying a uni-directional heat flux along the length of the sample is used in a number of works [2, 3, 21, 22, 26, 27, 31, 32, 72–75, 80, 82, 124, 125, 136, 137]. An alternative implementation of the NEMD method is represented in Fig. 3.7. In this approach, a hot heat bath region is defined in the center of the tube, two cold heat baths regions are applied at the two ends of the CNT, and equal and opposite fluxes are generated along the tube axis in opposite directions. This implementation is typically used in combination with periodic boundary conditions (PBCs) in the axial direction [4, 20, 23, 29, 30, 33, 77–79], thus creating a repeating pattern of bi-directional fluxes.

The discussion provided in the previous section demonstrates that for NEMD simulations implementing uni-directional flux, the length dependence of CNT conductivity is better captured by the overall system length, L_{Sys} , than by the length between the heat bath regions, L_C , although the majority of studies employing this method to investigate length dependence of conductivity use L_C as the defining length [2, 3, 72, 73, 124, 125]. Paradoxically, the results obtained in bi-directional flux simulations are often described in terms of the overall system length as the defining length [23, 29, 78, 79], despite the imposed thermal transport occurring in opposite directions over the two halves of the system length. This length definition does not seem to be intuitive given the nature of thermal transport in these systems, and the factors that affect the length dependence in the ballistic and diffusive-ballistic regimes. When a flux is applied between two heat bath regions, the dominant ballistic transport mechanism is energy transport from a hot heat source to a cold heat sink. In the case of bi-directional heat flux, the ballistic transport contributes to the heat transfer between the hot and cold bath regions, in the direction of the imposed heat flux. If the phonon mean free path is longer than the distance between the heat bath regions, however, the thermal transport may occur from a heat source, *through* a heat sink, and toward the second heat source on the other side of the computational system, against the dominant direction of heat transfer. In this case, the ballistic transport would actually serve to reduce the measured temperature gradient and the corresponding thermal conductivity, as it effectively inhibits the heat transfer in the direction of imposed flux. Thus, the ballistic thermal transport within the distance between the heat baths serves to increase thermal conductivity, while the ballistic transport at lengths greater than the distance between the heat baths regions serves to reduce the conductivity. Therefore, it seems plausible that thermal conductivity predicted in NEMD simulations is defined by the length of consistently imposed flux, *i.e.*, the length between the heat bath regions, rather than by the overall system length.

To investigate the effect of the bi-directional flux configuration on the predicted val-

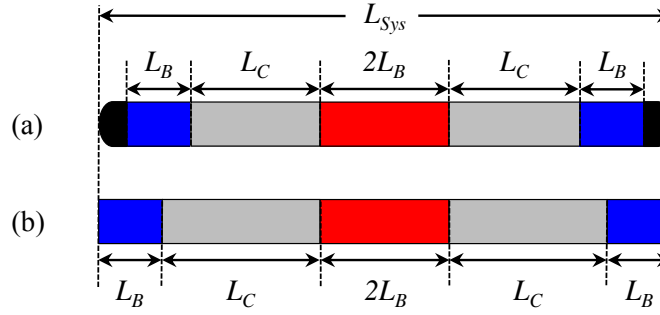


Figure 3.7: Schematics of computational setups with bi-directional heat flux implementations used in NEMD simulations of thermal conductivity of CNTs. The two setups are shown for free (a) and periodic (b) boundary conditions. In the case of free boundary conditions, the CNTs are covered by hemispherical fullerene caps that are not included in the heat bath regions.

ues of thermal conductivity, two NEMD simulations are performed for free and periodic boundary conditions applied along the axis of the CNTs as shown schematically in Fig. 3.7. In the case of free boundary conditions, the CNT is covered by two hemispherical fullerene caps and the total length of the system was 100 nm. Two cold bath regions are implemented immediately adjacent to the fullerene caps, and have a length of $L_B = 1$ nm each. A hot bath is implemented in the center of the CNT, measuring $2L_B = 2$ nm. The distance of unperturbed length between the heat bath regions is $L_C = 47.3$ nm on each side of the CNT. In the second simulation, the fullerene caps are removed and periodic boundary conditions are applied in the axial direction, creating a repeating pattern of bi-directional heat flux. In this case the overall system length remains 100 nm, and the distance between the heat bath regions is increased to $L_C = 48.1$ nm to account for the removal of the fullerene caps.

Thermal conductivity is calculated from the steady-state temperature profiles established in the system following a procedure similar to the one described in Section 3.2.1. The values of k are found to be $154 \text{ Wm}^{-1}\text{K}^{-1}$ in the free boundary conditions simulation, and $160 \text{ Wm}^{-1}\text{K}^{-1}$ with periodic boundary conditions. Comparing these predictions to the results obtained with uni-directional heat flux approach and described in Sections 3.2.2 and 3.2.3.1, we find that the results of bi-directional calculations are in a good agreement

Flux Direction	Boundary Conditions	L_{Sys}	$L_C + 2L_B$	k ($\text{Wm}^{-1}\text{K}^{-1}$)
bi-	periodic	100 nm	50 nm	160
bi-	free	100 nm	49 nm	154
uni-	free	50 nm	49 nm	154
uni-	free	100 nm	99 nm	196

Table 3.4: Thermal conductivity of (10,10) CNTs, k , predicted in NEMD simulations performed with bi-directional and uni-directional heat flux implementations. The predictions of the two types of simulations are reconciled when the results are compared for the same effective length defined as $L_C + 2L_B$.

with the ones obtained in simulations of Series 3 for $L_{Sys} = 50$ nm, $154 \text{ Wm}^{-1}\text{K}^{-1}$, but significantly under-predict the results for $L_{Sys} = 100$ nm, $196 \text{ Wm}^{-1}\text{K}^{-1}$, see Table 3.4. This observation supports the qualitative discussion provided above, which suggested that, due to the physical phenomena that lead to the length dependence, the length of consistently imposed heat flux is the length that defines the value of the thermal conductivity in bi-directional NEMD simulations. Keeping in mind the conclusion of Section 3.2.3.1, it is reasonable to include the length of the heat bath regions to the standard length definition. Thus, by defining the effective CNT length in bi-directional simulations as the length of an unperturbed region plus $2L_B$, $L_C + 2L_B \approx L_{Sys}/2$, we can reconcile the results obtained with the two types of the computational setup. Adopting this definition of CNT length may help to resolve some of the discrepancies in the values of CNT thermal conductivity reported in the literature.

3.2.3.3 Interatomic Potential

The interatomic potential is the most significant input parameter that must be defined in any MD simulation. Potentials that have been validated and widely used to represent carbon systems include the Tersoff [100], Brenner [102], Brenner-II [103], and AIREBO [111] potentials. Recently, modified sets of parameters for the Tersoff and Brenner-II potentials have been developed specifically for simulations of heat transfer in carbon nanotubes and graphene [105]. Considering the results of the simulations listed in Table 3.1, it is possible

to see a correlation between the type of interatomic potential employed in a simulation and the values of the predicted thermal conductivity: the increasing values of k tend to follow the order from AIREBO and Brenner-II + LJ, to Brenner/Brenner-II, to Tersoff, and to an optimized version of the Tersoff potential. Here two exceptions from this trend are noted: the value reported by Ren et al. [31], which is unusually high in comparison to other works employing the AIREBO potential, and the one by Berber et al. [18] which is acquired with the homogeneous non-equilibrium molecular dynamics (HNEMD) routine [138] and remains among the highest reported values in the literature. The differences in the CNT lengths and various parameters of the computational methods employed in the simulations, however, do not allow us to translate this apparent correlation to a definite quantitative conclusion on the extent the choice of the interatomic potential affects the value of thermal conductivity predicted in a simulation. Therefore, an additional series of NEMD simulations is performed for identical CNTs and computational setups, but different interatomic potentials. In this way, the possibility of other system parameters causing divergent results is eliminated, and the pure effect of the interatomic potential is examined in isolation.

The system used in this series of simulations is a (10,10) CNT with uni-directional heat flux (Fig. 3.4), $L_{\text{Sys}} = 205$ nm, and $L_B = 0.5$ nm. The computational setup and procedure used in the calculation of k are the ones described in Section 3.2.1. The four potentials investigated are original Tersoff [100], Brenner-II [103], AIREBO [111] with Brenner-II [103] adopted for bonding interactions, and the optimized Tersoff by Lindsay and Broido [105].

The results from the simulations, shown in the form of a bar chart in Fig. 3.8, reveal strong dependence of CNT conductivity on implemented potential. The general trend is the same as seen in the sample of published results presented in Table 3.1 (excluding the two highest values reported by Ren et al. [31] and Berber et al. [18]), with the highest values predicted with the optimized Tersoff potential, followed by the original Tersoff, Brenner-II and AIREBO potentials. The low values of k predicted with Brenner-II and AIREBO

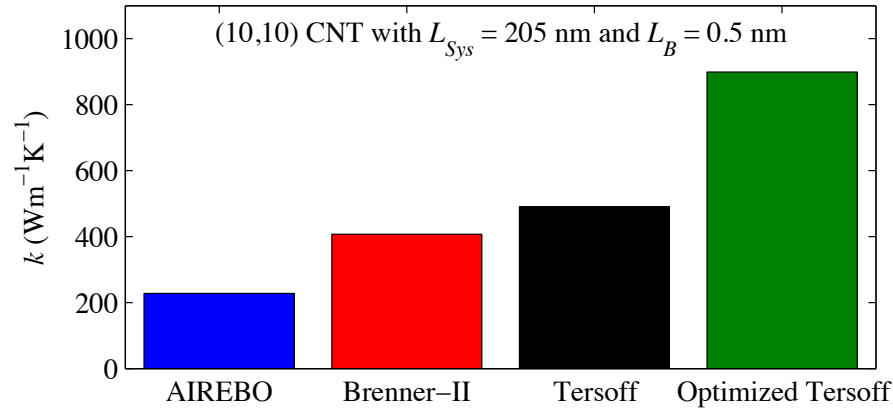


Figure 3.8: Thermal conductivity, k , predicted in NEMD simulations performed with four different interatomic potentials for identical CNTs under identical computational conditions.

potentials can be attributed to two factors: low velocities of acoustic phonons obtained from phonon dispersion relations for graphene and strong anharmonicity of Brenner-II potential resulting in high phonon-phonon scattering rates [105]. The long-range van der Waals interactions added to the Brenner-II potential in AIREBO may further increase the phonon scattering rate, thus additionally reducing the value of k . While the variability of the results of experimental measurements of thermal conductivity of individual CNTs [10–17] prevents a direct quantitative validation of interatomic potentials, the understanding of the degree to which the choice of interatomic potential can affect the predictions of the simulations may help in resolving some of the discrepancies in published MD results and may assist in design and interpretation of future computational studies. Moreover, despite the lack of quantitative predictive power of current MD calculations of thermal conductivity, the qualitative trends revealed in the simulations, such as the CNT length dependence shown in Fig. 3.3, are still consistent across studies undertaken with different interatomic potentials. These qualitative trends are certainly of interest for the design of CNT materials with thermal transport properties tailored for particular practical applications.

3.2.4 Effect of Inter-Tube Interactions in Bundles

The effect of inter-tube interactions on the intrinsic conductivity of a nanotube is investigated in MD simulations performed for systems of one, two, and seven CNTs that are shown schematically in Fig. 3.9a. The individual CNTs used in the simulations are 160 and 300 nm long and consist of 26 440 and 49 640 atoms, respectively. The CNTs are covered by 110-atom caps at the ends with one of the caps interfacing with the nanotube by a 20-atom ring constituting a half of the nanotubes unit cell. Free (vacuum) boundary conditions are applied in all directions. The basic sample preparation and computational procedure for simulations presented in this section differ slightly from the routine described in Section 3.2.1. Here, the configurations of CNT pairs and bundles are relaxed by quenching atomic velocities for 15 ps to establish a low-energy separation between the nanotubes and to prevent oscillations that would affect inter-tube interactions. All systems are then gradually heated to 300 K by applying the Langevin thermostat for 30 ps while ensuring that the total linear and angular momenta are zero [1]. Finally, in order to establish a steady-state temperature gradient along the CNTs, a constant heat flux is applied by scaling the velocities of atoms in two 0.5 nm wide heat bath regions located on either end of each CNT, neglecting the hemispherical caps. The velocity scaling is done so that the same amount of energy, Q_{HB} , is added and removed per unit time in the two heat bath regions of each CNT. The rates of the energy addition/removal used in the simulations of 160 nm and 300 nm CNTs are $Q_{HB} = 1.5 \text{ eV ps}^{-1}$ and $Q_{HB} = 1.3 \text{ eV ps}^{-1}$, respectively. These rates correspond to heat fluxes of $Q_{HB}/\Omega = 1.68 \times 10^{11} \text{ Wm}^{-2}$ and $Q_{HB}/\Omega = 1.46 \times 10^{11} \text{ Wm}^{-2}$, where Ω is the cross-sectional area of the CNT, defined as $\Omega = 2\pi\delta_T R_T = 1.43 \text{ nm}^2$, $R_T = 0.67 \text{ nm}$ is the nanotube radius found in MD simulations as the average radial distance of carbon atoms from the axis of an isolated CNT equilibrated at 300 K, and $\delta_T = 0.34 \text{ nm}$ is the nominal thickness of the CNT wall taken to be equal to the interlayer spacing in graphite [21, 47, 83].

The values of thermal conductivity of individual CNTs, k , are calculated from the

L_T	Single CNT	2-CNT Configuration	7-CNT Configuration
160 nm	$223 \pm 15 \text{ Wm}^{-1}\text{K}^{-1}$	$220 \pm 14 \text{ Wm}^{-1}\text{K}^{-1}$	$215 \pm 10 \text{ Wm}^{-1}\text{K}^{-1}$
300 nm	$241 \pm 6 \text{ Wm}^{-1}\text{K}^{-1}$	$243 \pm 5 \text{ Wm}^{-1}\text{K}^{-1}$	$238 \pm 6 \text{ Wm}^{-1}\text{K}^{-1}$

Table 3.5: Thermal conductivities of a (10,10) CNT, k , and the corresponding standard deviations from the mean values predicted in MD simulations performed for a single CNT, a pair of parallel interacting CNTs, and a bundle of 7 CNTs, as shown in Fig. 3.9a, for the CNT length $L_T = 160$ and 300 nm. In multi-tube simulations, the conductivity reported is the mean of all conductivity calculations for the 2 or 7 CNTs in the corresponding configurations. The measure of uncertainty presented is one sample standard deviation of all sequential k calculations obtained after achievement of a steady state. The values of k in all configurations with $L_T = \text{const}$ are within the standard deviations of each other, suggesting that the effect of the inter-tube coupling on the intrinsic thermal conductivity of CNTs is statistically insignificant.

Fourier law, $k = -Q_{HB}/(\Omega dT/dx)$, where the temperature gradients, dT/dx , are determined by linear fits of the temperature profiles generated in constant heat flux simulations, e.g., Fig. 3.9b. The ~ 20 nm regions of non-linear temperature distributions in the vicinity of the CNT ends are excluded from the calculation of dT/dx . The time required for the establishment of the steady-state temperature profiles was about 0.4 ns for 160 nm CNTs and 0.8 ns for 300 nm CNTs. In the steady state, the simulations are run for an additional 200 ps to 1200 ps and the instantaneous values of thermal conductivity are evaluated every 5 fs from instantaneous temperature gradients. The instantaneous values of thermal conductivity collected in the steady-state regime are found to obey normal distributions, confirming the random statistical nature of the fluctuations of these values during the time span of the data collection. The average thermal conductivity k and the sample standard deviation are then calculated from the instantaneous values. For multi-tube configurations, the values of k and sample standard deviations are derived from the total sample set of conductivity calculations for all CNTs present in a given configuration.

The temperature profiles shown in Fig. 3.9b for an isolated CNT and CNT bundles are almost identical, suggesting that the thermal conductivity of individual CNTs is not significantly affected by the interactions among the CNTs. Indeed, the values of k listed in Table 3.5 for each of the three configurations are within the standard deviations of each

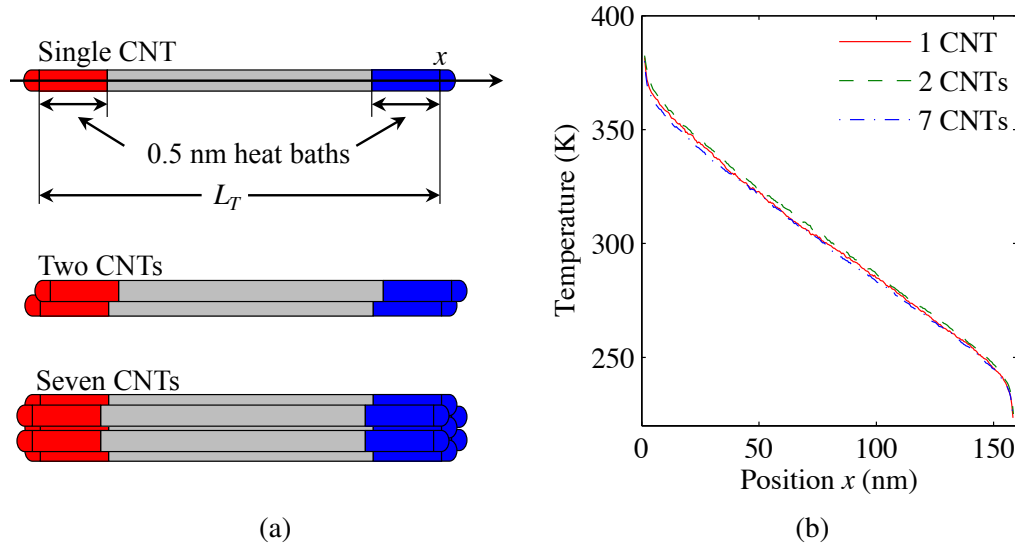


Figure 3.9: A schematic representation (not to scale) of the three aligned CNT bundles (a) and representative temperature profiles obtained in the simulations performed for (10,10) CNTs of length $L_T = 160$ nm (b). Thermal flux is applied to each CNT individually and the values of thermal conductivity are obtained from the steady-state temperature profiles. All simulations are performed for capped CNTs with the cylindrical part of length L_T . The temperature profiles in panel (b) for 2- and 7-CNT systems are obtained by averaging the profiles calculated for individual CNTs in the bundles.

other for a given length of the CNTs, while the increase of k with increasing CNT length L_T is characteristic of the diffusive-ballistic phonon transport in CNTs that has been discussed in a number of works [1, 3, 21, 126, 129] and presented in Section 3.2.2.

The absence of any significant effect of the van der Waals inter-tube coupling in CNT bundles on the intrinsic thermal conductivity of individual CNTs is consistent with relatively small changes of the vibrational spectra of CNTs due to the inter-tube interactions and negligible contribution of inter-tube phonon modes to thermal conductivity of bundles [122, 139]. It also suggests that three-phonon umklapp scattering involving phonons from neighboring CNTs does not play any significant role in perfect bundles consisting of defect-free CNTs. The results of the simulations, however, contradict the experimental observation of the pronounced decrease of the thermal conductivity of bundles with increasing bundle thickness [53, 54, 118] that is commonly attributed to the dramatic enhancement of phonon scattering by the inter-tube interactions [18, 36, 53–55, 120]. An alternative

explanation of the bundle thickness dependence of the thermal conductivity could be the increased degree of CNT misalignment and concentration of inter-tube defects, cross-links and foreign inclusions in larger bundles, which could result in the increase of both the phonon scattering and inter-tube contact thermal resistance. Indeed, SEM images of thick “bundles” that exhibit the lowest thermal conductivity on the order of several $\text{Wm}^{-1}\text{K}^{-1}$ reveal a loose arrangement of poorly aligned CNTs that resemble pillars cut from vertically aligned arrays of CNTs [116, 117].

3.3 Summary

The results of a systematic investigation of the effect of various computational parameters on the values of thermal conductivity of CNTs predicted in MD simulations uncover some of the key reasons for the wide variability of the computational predictions reported in literature and provide guidance for designing simulation setups that reduce the ambiguity in data interpretation.

The CNT length dependence of thermal conductivity is investigated in a broad range of nanotube lengths, from 47 nm to 630 nm, and is found to exhibit a gradual transition from a strong length dependence for CNTs shorter than ~ 200 nm to a much weaker dependence for longer CNTs. This dependence is characteristic of the transition from ballistic to diffusive-ballistic heat transport regimes and has been observed in many of the earlier studies. A detailed analysis of the CNT length dependence reveals that, in NEMD simulations with uni-directional heat flux implementation, the effect of increasing length of the central part of the nanotube, L_C , is nearly indistinguishable from the effect of increasing length of the heat bath regions, L_B . This observation suggests that the common practice of neglecting the length of the heat bath regions when defining the CNT length in NEMD simulations may introduce an uncertainty in interpretation of the results, as the variability of L_B in different studies may translate into a substantial variability in the predicted values of thermal

conductivity. The results of this study suggest that the total length of a CNT (*including* the length of the heat bath regions) should be used as the definition of the CNT length in NEMD simulations with uni-directional heat flux. To provide an adequate representation of the true nature of the system being modeled, the length of the heat bath regions should be short relative to the overall CNT length. The length dependence of k in bi-directional flux implementations, commonly used with periodic boundary conditions, is also shown to be best represented by the definition of the effective CNT length comprised of the length of the heat bath regions and the length of an unperturbed part of the CNT between the hot and cold heat bath regions. This convention yields values of k that are consistent between the two (uni- and bi-directional) implementations of the heat flux in NEMD simulations.

The effect of the choice of the interatomic potential on the value of thermal conductivity predicted in NEMD simulations is also quantified in a series of simulations performed with several commonly used potentials. An up to a four-fold difference in the values of k is predicted with different potentials for identical CNTs and computational setups. This large difference suggests that quantitative agreement between the results obtained with different interatomic potentials should not be expected. Many of the qualitative trends revealed in the simulations, however, are consistent across studies employing different potentials and are providing useful insights into the mechanisms of the nanoscale thermal transport in CNTs.

Overall, the results of the systematic evaluation of the effect of the boundary conditions, size and location of the heat bath regions, definition of the CNT length, and the choice of interatomic potential on the predictions of NEMD simulations clarify the origins of quantitative discrepancies across published data and provide recommendations on the choice of computational parameters that may reduce some of the inconsistencies between the computational results. The results of MD simulations of thermal conductivity in individual CNTs and in bundles consisting of 2 and 7 CNTs suggest that, contrary to a number of earlier reports, the van der Waals inter-tube coupling in the bundles does not result in

any statistically significant changes in the intrinsic conductivity of the CNTs. Implications for this result mean overall thermal transport in aligned CNT bundles can be improved by increasing the number of direct CNT channels in the bundle.

Chapter 4

CNT-CNT Thermal Conductance

4.1 Background

Thermal conductance between CNTs is achieved through non-bonded van der Waals interactions. Typical dimensions of CNT materials and structures are much longer than their constituent CNTs. Therefore, thermal transport in these devices may be limited by the weak CNT-CNT conductance and it is often assumed that inter-tube conductance, rather than intrinsic conductivity of CNTs, limits the effective conductivity of CNT-based materials [5–8, 43–46]. In addition, results from molecular dynamics (MD) simulations reported by Volkov et al. [76] and presented in Section 3.2.4 of this dissertation indicate inter-tube interactions have no significant affect on the intrinsic conductivity of individual CNTs, which implies low collective conductivity of CNT structures is primarily caused by low CNT-CNT contact conductance. Any measures that can improve inter-tube conductance will directly improve the thermal performance of the CNT structure as well. Therefore, it is important to determine what structural parameters affect thermal transport across CNT-CNT junctions.

The sensitivity of CNT-CNT conductance to the parameters which define the physical structure of the CNT-CNT contact and the surrounding environment is explored in this chapter. Further background information on the effect of the variations of CNT length, local density of contacts, and contact area on CNT-CNT conductance is provided in Sections

4.1.1, 4.1.2, and 4.1.3, respectively.

Next, computational results of a systematic evaluation of the sensitivity of the values of CNT-CNT conductance predicted in non-equilibrium molecular dynamics (NEMD) simulations to the parameters of CNT-CNT contacts are reported in Section 4.2. The magnitude and range of the dependence of CNT-CNT conductance on CNT length are analyzed in Section 4.2.1. The role of local density of CNT-CNT contacts on conductance is investigated in Section 4.2.2. Only a $\sim 10\%$ reduction in contact conductance is observed for the maximum density of contacts separated by their equilibrium distance and no reduction is found for lower contact densities. This is in sharp contrast with previously published findings [8] and leads to an important conclusion that the total conductance through CNT structures can be increased by increasing the number of CNT-CNT contacts. Results which demonstrate a linear increase in conductance with contact area between partially overlapping parallel CNTs are presented in Section 4.2.3. The linear dependence of the conductance on the overlap area, however, is found to break down for non-parallel configurations with very small contact areas, as demonstrated by the results reported in Section 4.2.4. This observation serves as the motivation for a qualitative study of conductance across multiple interacting interfaces in a 2-dimensional Lennard-Jones “toy model” discussed in Chapter 5 and provides a foundation for the development of a general predictive model of CNT-CNT conductance presented in Chapter 6.

4.1.1 Background on the Effect of CNT Length

The dependence of intrinsic CNT conductivity on CNT length is discussed in detail in Chapter 3. While much of this length dependence is due to an increase of ballistic thermal transport length as CNT length increases in the ballistic length regime, Cao and Qu [33] argued that an increase in available long wavelength phonon states with increasing CNT length also contributes significantly to the increase in conductivity. It is plausible that the addition of long wavelength phonon states may also promote an increase in CNT-CNT

conductance if these phonons contribute to the conductance. Kumar and Murthy [106] employed MD simulations to perform wavelet analysis of thermal pulse propagation along the axes of CNTs forming perpendicular cross-junctions at a very low temperature (0.01 K). The wavelet traveled along the axis of one CNT and passed through the contact region into the second perpendicular CNT. Analysis of the vibrational frequencies showed that most of the dominant frequencies excited in the second CNT were relatively low (less than 10 THz), implying that low frequency, long wavelength phonons transmit across CNT-CNT junctions more readily. This is similar to the findings of Shenogin et al. [140] who concluded the majority of heat transfer from a CNT into a surrounding octane liquid occurred predominantly through coupling of low frequency vibrational modes. While conduction between a CNT and surrounding liquid is expected to be different than conduction between two CNTs, the authors assert that this low frequency dominance is due to the weak van der Waals interactions at the interface, which are also responsible for conduction between two CNTs. They go on to show an increase in conductance per area with increasing CNT length above 2 nm. Huxtable et al. [141] also found an increase in conductance per area between a CNT and surrounding octane liquid for lengths up to 3.5 nm. Through spectral temperature analysis, they showed the lowest frequency vibrations to be most strongly coupled to the surrounding liquid. Conversely, Carlborg et al. [142] did not find any length dependence for conductance per area between a CNT and surrounding liquid argon, though they attributed this inconsistency to the difference between vibrational states in liquid argon and liquid octane.

Though there have been several direct MD investigations into the length dependence of CNT-CNT conductance, a definitive and consistent description is still lacking. Evans et al. [7] performed MD simulations of conductance at a junction between two perpendicular CNTs and found a significant length effect up to CNT lengths of about 20 nm. Zhong and Lukes [5] simulated conductance between parallel, overlapping CNTs with varying overlap and CNT length. They showed pronounced length dependence below 10 nm, which

becomes weaker as CNT length reaches 40 nm. Xu and Buehler [6] also modeled conductance between parallel CNTs and reported only very weak length dependence for CNTs between 25 and 75 nm.

While these results are not in direct contradiction with each other, there are still unresolved issues regarding the length dependence of CNT-CNT conductance. The works referenced above considered either only parallel or only perpendicular CNTs and did not attempt to come up with a general description of CNT-CNT conductance applicable to different configurations. A broader range of CNT lengths should be examined to definitively determine the saturation limit of CNT length effects. Important aspects to discern include the strength of this length dependence and the range of CNT lengths for which it is present. A more complete understanding of these length effects will help provide a context for comparison of conductance calculations and determine the parameters necessary for optimizing thermal performance of CNT based materials. Therefore, a series of simulations was performed to investigate the effect of CNT length on CNT-CNT conductance and the results of this study are presented in Section 4.2.1.

4.1.2 Background on the Effect of Contact Density

The thermal conductivity of CNT-based materials can be increased by increasing the density of CNTs. In the case of vertically aligned CNT forests, such as those used for thermal interface materials (TIMs), this is attributed to an increase in the number of direct channels for conduction [55]. In the case of more complex configurations of CNT networks, this increase is attributed to an increase in the density of CNT-CNT contacts in the network. Koblinski and Cleri [143] modeled electrical conductivity in a percolated network of conducting nanofibers, where the contact resistance limits the overall network conductivity, as is the case in CNT networks. They showed that both network electrical conductivity and concentration of contacts increased quadratically with increasing concentration of conducting fibers. Evans and Koblinski [92] found similar results from MD simulations of

thermal conductivity through repeated layers of perpendicular CNT arrays. They reported the thermal conductivity of a stacked structure consisting of four CNTs per repeated layer to be four times greater than that of a structure consisting of two CNTs per layer.

Despite these results, it is possible that an increase in contact density may not always increase the total conductivity in a CNT based material. Prasher et al. [8] employed atomistic Green's function simulations to model thermal conductance across individual junctions formed by perpendicular CNTs. They compared the conductance per junction for the case of a single junction formed by two perpendicular CNTs to the conductance per junction for the case of two junctions formed when two parallel CNTs were crossed by a single perpendicular CNT, to study the effects of contact density on conductance per junction. Their results show that the conductance per junction is reduced by approximately an order of magnitude for the two junction case, when the junctions are separated by only 0.816 nm. These results suggest there could be some critical contact density, above which the conductance per junction is reduced. It follows that for some configurations, an increase in contact density may reduce the overall thermal transport through the CNT network. In fact, the authors cite the decreased conductance per junction as the main explanation of discrepancies between the results of their experimental measurements of conductivity of a CNT bed and an analytical equation [46] based on the MD results for individual junction conductance. Thus, it is important to resolve any uncertainty regarding the influence of contact density on individual contact conductance. Parametric studies should be undertaken to determine if an effect exists, and for what critical levels of contact density. Clarification of these issues may help resolve discrepancies between experimental observations and theoretical predictions, and serve as a guide for optimal design of CNT networks for thermal applications. A series of simulations was performed to resolve the relationship between contact density and CNT-CNT conductance. The results of this study are reported in Section 4.2.2.

4.1.3 Background on the Effect of Contact Area

Defining a contact area between two adjacent, cylindrical CNTs is non-trivial. However, in the case of parallel, overlapping CNTs, as studied in some of the works referenced above [5, 6], any realistic definition of contact area will be linearly proportional to Δx_{12} , the length of the overlapping region between the two CNTs. In addition, σ_T can be defined as the conductance *per overlap length*, given in $\text{Wm}^{-1}\text{K}^{-1}$ and linearly proportional to the conductance per area. Thus, the effect of contact area on conductance per area can be indirectly observed by varying Δx_{12} and studying the effect of this variation on σ_T .

When the results from the previous works are defined in this manner, an interesting result is observed. Figure 4.1 represents the data from the two studies of overlapping CNTs. Here the data have been manipulated from the original form in the cited works to represent the conductance per overlap length, σ_T . For comparison across the two works, the conductance values have been divided by the maximum conductance value observed in each work, σ_{max} , respectively. In both works, σ_T is observed to decrease with increasing Δx_{12} . These observations imply that conductance per area *decreases* with increasing contact area over the range of overlap lengths studied.

The implications of the observed trend are significant. While total conductance was seen to increase with contact area over the range studied in both works, with diminishing returns for greater contact areas, there may be a point at which conductance does not improve with increased contact area. The contact area between CNTs is defined by the physical arrangement of CNTs in a network. If conductance per area is found to decrease with contact area, there may be some optimal contact area, above which the diminishing improvement in CNT-CNT conductance does not compensate for possible restrictions to thermal transport due to necessary changes in geometrical arrangement of CNTs, such as a reduction in the number of conducting channels. A better understanding of the effects of contact area on CNT-CNT conductance is needed. A broader range of contact areas must be investigated, independent of other variables, to determine the extent of the trend

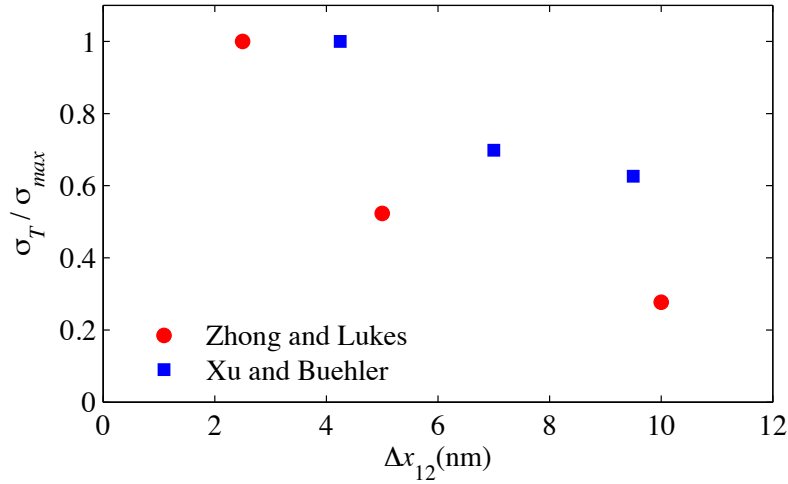


Figure 4.1: A comparison of the values of CNT-CNT conductance predicted for different overlap lengths in two studies by Zhong and Lukes [5] and Xu and Buehler [6]. The values have been manipulated from the original reference to reflect conductance per overlap length, and are normalized with respect to the highest value found in the respective studies. Both works show an inverse relationship between conductance per area and contact area.

suggested in the previous works. Such a systematic study was undertaken to investigate the relationship between contact area and CNT-CNT conductance, and results are presented in Section 4.2.3.

4.2 Computational Results

In this section, computational results of a systematic evaluation of the sensitivity of the values of MD predictions of CNT-CNT conductance to structural parameters of the surrounding environment are presented. The dependence of CNT-CNT conductance on CNT length is investigated and results are presented in Section 4.2.1. Results from a series of simulations investigating the role of local density of CNT-CNT contacts on the conductance are reported in Section 4.2.2. Results which demonstrate a linear increase in conductance with contact area between partially overlapping parallel CNTs are presented in Section 4.2.3. Conductance is found to deviate from this monotonic increase for non-parallel configurations with very small contact areas, as demonstrated by the results reported in Section

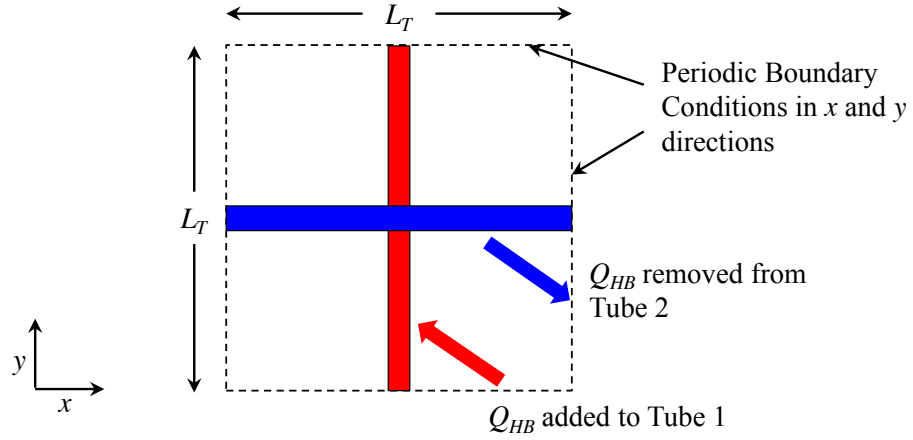


Figure 4.2: A schematic of a configuration employed to investigate the effect of CNT length on CNT-CNT conductance. Energy is uniformly added to Tube 1 and uniformly removed from Tube 2 at a rate of Q_{HB} . The lengths of both tubes, L_T , are identical and varied between simulations.

4.2.4.

4.2.1 Effect of CNT Length

A series of simulations is performed to resolve the nature and magnitude of the effect CNT length may have on CNT-CNT conductance. The Tersoff potential [100] describes interactions between carbon atoms belonging to the same CNT, and a Lennard-Jones potential describes the non-bonded van der Waals interactions between atoms belonging to different CNTs. In this implementation, the Lennard-Jones parameters are $\sigma = 3.41 \text{ \AA}$ and $\varepsilon = 3.0 \text{ meV}$. These values were chosen to closely match the values obtained through private communications with Evans et al., who conducted a similar study [7] investigating the length dependence of CNT-CNT conductance and an additional study [92] of the effect of contact density on CNT-CNT conductance, for the sake of comparison. A cutoff distance is used to ensure the Lennard-Jones potential equals zero for all separation distances greater than 1 nm. The equations of motion are solved using the velocity Verlet algorithm and the timestep of integration is 1 fs.

Fig. 4.2 illustrates the arrangement of CNTs in this series of simulations. Two perpendicular (10,10) CNTs of equal length, L_T , are brought into contact to form a cross junction. Tube 1 is orientated along the y -axis and Tube 2 is orientated along the x -axis. Periodic boundary conditions are applied in the x and y directions, and free boundary conditions are applied in the z direction, which is perpendicular to both the x and y directions. Six independent configurations are constructed this way, each with different L_T , ranging from 5 to 200 nm. The same procedure is performed on all configurations, to measure the cross-tube conductance as a function of L_T .

Initially, the configurations are relaxed by quenching atomic velocities for 0.5 ns to establish an equilibrium separation between the nanotubes and to prevent oscillations that would affect inter-tube interactions. The periodic boundaries are gradually adjusted at this stage to reach a target pressure of 1 atm in the x and y directions. The temperature of each CNT is determined from Eq. 2.1 and the systems are then gradually heated to 300 K by applying the Langevin thermostat [123] for 0.5 ns. The periodic boundaries are gradually adjusted again to reach the target pressure of 1 atm in the x and y directions for the final simulation temperature of 300 K.

Thermal management is applied to each tube in its entirety. Energy is added to Tube 1 at a rate of 0.16 eV ps^{-1} by scaling the velocities of all atoms in Tube 1, while energy is removed from Tube 2 at a rate of -0.16 eV ps^{-1} by scaling the velocities of all atoms in Tube 2. In this way, a flux is created across the junction from Tube 1 to Tube 2 with a heat flow rate of $Q_{HB} = 0.16 \text{ eV ps}^{-1}$. This results in a temperature difference between the two tubes, ΔT_{12} . This temperature difference increases with simulation time, until a steady-state temperature difference is achieved, which is related to the applied heat flow rate, Q_{HB} , and CNT-CNT conductance, G , by the expression $G = Q_{HB}/\Delta T_{12}$.

The number of atoms per tube ranges from 800 to 31 560 for the 5 and 200 nm tubes, respectively. Applying the velocity scaling procedure to the shorter tubes over a fewer number of atoms has a stronger effect on each individual atomic velocity. Over time,

an individual tube can acquire a net momentum in the x or y direction, due to statistical anomalies arising from velocity scaling of the limited number of atoms in the system, and cause the point of contact between the two tubes to move along the axis of one or both of the tubes. The physical configuration is such that if one tube gains a net momentum in the x or y direction, the other tube can move in the opposite direction to maintain a net momentum of zero for the entire system. To prevent an individual tube from achieving a non-zero net momentum, a small spring force is applied to each tube to restore it back to its original position. The spring force is applied evenly to all atoms in the tube, and the net magnitude of the force in the i direction is $F_i = -K_{Spr}\Delta x_i$, where Δx_i is the difference between i coordinates of the tube's current center of mass position and its initial center of mass position, and $K_{Spr} = 0.0003 \text{ eV } \text{\AA}^{-2}$ is the spring constant. This spring constant is chosen such that the spring potential, $U_i = 0.5K_{Spr}\Delta x_i^2$, is equal to $k_B T$ at $\Delta x_i = 14 \text{ \AA}$, where T is the system temperature of 300 K, and 14 \AA is roughly equal to the tube diameter. In this way, small, random perturbations about equilibrium, associated with the thermal vibrations of the system, are not suppressed, while larger non-physical displacements are prevented. The spring implementation was validated by performing two identical simulations with the exception of implementing the spring in one and excluding it from the other. No statistically relevant difference was found between the final results of the two methods. Therefore, it also follows that no statistically significant effect is seen when the non-zero momentum of individual tubes is present. Nonetheless, the spring implementation is adopted in the simulations for ease of visualization and data interpretation.

The average temperature of each CNT is calculated by evaluating Eq. 2.1 over all atoms in a CNT. A time series is generated by recording the average temperature of each CNT every 1 fs during the simulation. A moving average of each CNT's temperature is then generated by averaging each time series over a 40 ps temporal window to reduce statistical noise. A moving average of G is calculated over the same temporal window from the constant applied flux, Q_{HB} , and a moving average of ΔT_{12} , which is the difference between

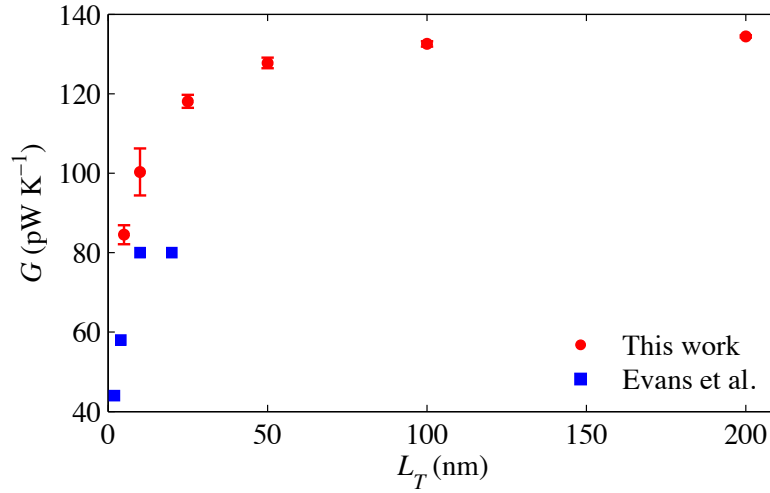


Figure 4.3: Calculations of CNT-CNT conductance, G , as a function of CNT length, L_T , obtained from this work (red circles) and a less extensive work by Evans et al. [7] (blue squares). The uncertainty in the final calculations of this work is represented by one sample standard deviation of all sequential G calculations obtained after achievement of a steady state. This value can vary between simulations as it is dependent on the statistical noise associated with the calculation of the temperature of each tube and the temperature difference between tubes, ΔT_{12} , both of which vary between simulations. The present study and the calculations by Evans et al. predict similar values of G for CNT lengths $L_T \leq 10$ nm. For longer CNT lengths, Evans et al. predict an abrupt deviation from the trend and a lower saturation limit.

the moving average temperature of Tube 1 and the moving average temperature of Tube 2. This moving average of G approaches, and eventually fluctuates about, a constant value when the system reaches the steady state. The time required to reach the steady state scales with the system size and ranges from ~ 2 ns for $L_T = 5$ nm to ~ 20 ns for $L_T = 200$ nm. After steady state has been achieved, the moving average of G is recorded for an additional period of 1 - 6 ns, depending on the system size and the corresponding level of statistical noise, to generate a sample set of G measurements. The mean of this sample set is the final reported value of G , and the sample standard deviation is taken as a measure of variation in the final value.

The final G values are plotted as a function of L_T in Fig. 4.3, and are represented as red circles with error bars indicating one sample standard deviation of all calculations of G used in determining the final mean value. CNT-CNT conductance is observed to increase

with CNT length over the range of lengths studied. The effect is the strongest for shorter CNTs and approaches a saturation limit near $L_T \approx 200$ nm. These results represent the most extensive investigation into the effect of CNT length on conductance that can be found from a thorough literature review. The results reveal a stronger effect over a longer range of CNT lengths than previously reported. Xu and Buehler [6] concluded the length effect was small enough to disregard for lengths between 25 and 75 nm. A more thorough investigation was performed by Evans et al. [7] and followed a procedure that was almost identical to the one described above. The Tersoff potential was implemented in combination with the Lennard-Jones potential to describe non-bonded carbon atom interactions. The authors cite almost the same potential parameters ($\sigma = 3.40$ Å, $\epsilon = 3.0$ meV) as employed in the simulations presented here ($\sigma = 3.41$ Å, $\epsilon = 3.0$ meV). Note that the values of the potential parameters used in the present study and obtained from private communications with the authors were from another study by the authors [92] designed to investigate the effect of CNT-CNT contact density on CNT-CNT conductance, which is also investigated in the present work. However, the similarities of the potential parameters used in all three of these works are such that it is reasonable to quantitatively compare the results of Evans et al. [7] and the results obtained in the present work. The blue squares shown in Fig. 4.3 represent the results reported by Evans et al. Results of Evans et al. for lengths $L_T \leq 10$ nm appear to be consistent with the trend seen in the results of the current work. However, Evans et al. show a deviation from this trend for length greater than $L_T = 10$ nm, with G nearly reaching a saturation limit by $L_T = 20$ nm. This variation in results affects the prediction of the maximum conductance and the length at which G can be considered to be nearly independent of CNT length.

This point may be better illustrated by implementation of the linear extrapolation technique [132, 134], the general premise of which has been previously described in Section 3.2.3.1. Here, the method may be used to extrapolate predicted values of G for CNT lengths that exceed the range studied. The estimates of the thermal conductance between infinitely

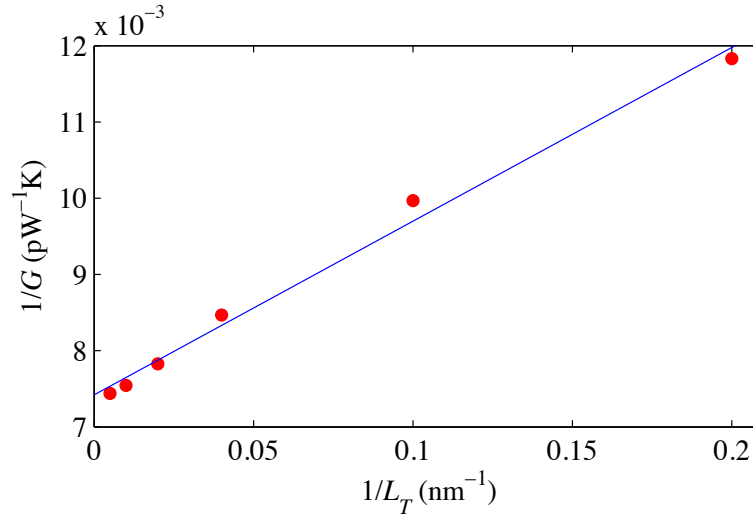


Figure 4.4: Inverse of conductance, G , plotted with respect to the inverse of CNT length, L_T . The linear extrapolation technique allows for prediction of conductance between two infinitely long CNTs.

long CNTs, G_∞ , can be obtained by plotting the dependence of $1/G$ on $1/L_T$ predicted in NEMD simulations and extrapolating it to $L_T \rightarrow \infty$. Fig. 4.4 shows the results of this procedure applied to data obtained in this work and shown in Fig. 4.3. Extrapolating to $1/L_T = 0$ yields a prediction of $G_\infty = 135 \text{ pW K}^{-1}$. Evans et al. followed the same linear extrapolation procedure for their results and predicted a value of $G_\infty = 91 \text{ pW K}^{-1}$. In addition, the current work demonstrates CNT length has a more significant effect on conductance over a larger range of lengths. For further comparison of the different trends, $L_{0.95}$ can be defined as the CNT length which corresponds to a predicted conductance $G = 0.95G_\infty$. This provides a quantitative way to compare the point at which G has nearly reached the saturation limit and further increase in CNT length does not yield a significant increase in conductance. This length is found to be $L_{0.95} = 59 \text{ nm}$ for the current work. Performing the same analysis for the data provided by Evans et al. yields $L_{0.95} = 42 \text{ nm}$.

This section represents a thorough investigation into the effect of CNT length on CNT-CNT conductance. The results demonstrate a stronger length dependence over a longer range of CNT lengths than has been previously reported. Linear extrapolation predicts a limiting value of G_∞ that is 48% higher than predicted in a similar, though less extensive,

study [7]. The length required to reach 95% of G_∞ , $L_{0.95} = 59$ nm, is found to be 40% longer than the respective $L_{0.95}$ found in the earlier study. Therefore, greater conductance than previously predicted can be achieved when CNT lengths are greater than ~ 60 nm. These findings have implications for the optimization of thermal transport in CNT-based materials which is significantly restricted by low CNT-CNT conductance.

4.2.2 Effect of Contact Density

A series of simulations is performed to investigate the role contact density has on CNT-CNT conductance. One way to quantify the contact density is by the distance between contacts. Fig. 4.5 illustrates the configuration of the simulation series. The setup is similar to the configuration employed in Section 4.2.1, with the addition of a third CNT, Tube 3, which forms a second cross-junction with Tube 1. Periodic boundary conditions are applied in the x and y directions and free boundary conditions are applied in z direction. In this series, the lengths of all three CNTs are fixed at 100 nm. The centers of Tube 2 and Tube 3 are separated by distance d , which is varied between simulation runs. In this way, the conductance per junction is measured as a function of the junction separation distance. The description of interatomic potentials, timestep of integration, and integration algorithm are identical to those described in Section 4.2.1.

The preparation routine is identical to that which is described in Section 4.2.1. After the system has been equilibrated at 300 K, energy is added to Tube 1 at a rate of 0.15 eV ps $^{-1}$ in the same manner as described above. Energy is also removed from Tube 2 and Tube 3 such that the total energy removed from both tubes is removed at a rate of 0.15 eV ps $^{-1}$. In this way, an average heat flow rate of $Q_{HB} = 0.075$ eV ps $^{-1}$ is maintained across each individual junction. The computational procedure to determine steady state and calculate the final conductance is the same as the procedure described in Section 4.2.1 with the additional step of dividing the final conductance by 2 to determine the conductance per junction which is plotted with respect to the junction separation distance in Fig. 4.6. For

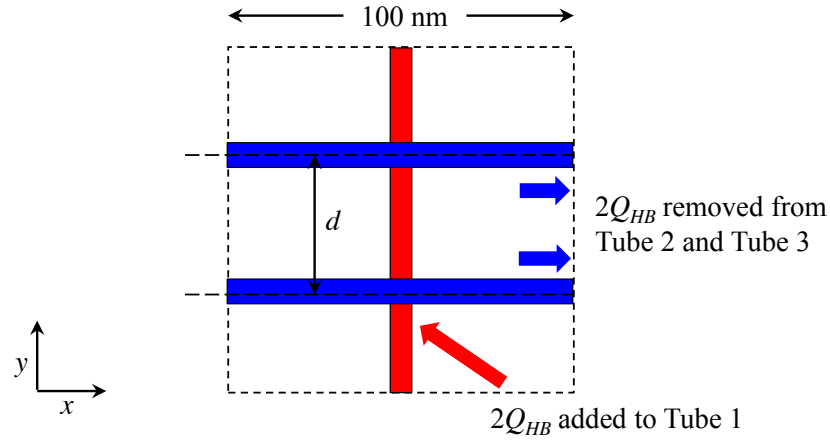


Figure 4.5: A schematic of the configuration employed to investigate the effect of contact density on CNT-CNT conductance. Energy is uniformly added to Tube 1 and uniformly removed from Tubes 2 and 3 at a rate of $2Q_{HB}$. The lengths of all tubes, L_T , is 100 nm and the distance between the centers of Tube 2 and Tube 3, d , is varied between simulations.

all but the lowest separation distance, the restoring spring force described in Section 4.2.1 is applied to each tube individually to ensure the average separation distance is maintained throughout the duration of the simulation. The lowest separation distance case, $d = 0.314$ nm, corresponds to the equilibrium separation distance between Tubes 2 and 3. In this case the tubes are allowed to reach their equilibrium separation distance and a spring force is applied to both tubes as a whole, keeping the pair centered on Tube 1 but not affecting the separation distance between the pair.

The data show no statistically significant effect from separation distance for distances $d \geq 5$ nm. Furthermore, there is only roughly a $\sim 10\%$ decrease in conductance when the tubes are separated by their equilibrium separation distance. For all initial separation distances > 3 nm there were no direct atomic interactions between Tubes 2 and 3 due to the imposition of a 1 nm cutoff distance in the Lennard-Jones potential. Simulations were attempted for $d = 3$ nm but the attractive force between Tube 2 and Tube 3 overcame the restoring spring force causing the two tubes to draw towards their equilibrium separation distance and resulting in a final conductance value that was consistent with the lowest

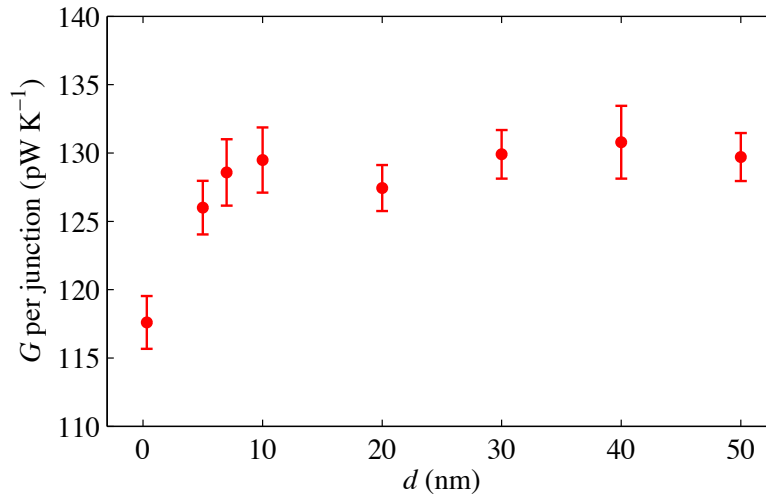


Figure 4.6: Conductance, G , per junction plotted with respect to distance between junctions, d . The uncertainty is represented by one sample standard deviation of all sequential G calculations obtained after achievement of a steady state. There is no statistically significant effect from the presence of neighboring junctions, except for the case when $d \approx 0.314$ nm, the equilibrium separation distance, which demonstrates a $\sim 10\%$ reduction. This contradicts findings by Prasher et al. [8] who predict a reduction by approximately one order of magnitude.

separation distance case, $d = 0.314$ nm. With the separation distance d defined as the distance from the center of Tube 2 to the center of Tube 3 at the start of the simulation there are no initial attractive forces between tubes when $d > 2.4$ nm, where 2.4 nm is equal to the tube diameter plus the cutoff distance. However, attractive forces between Tube 2 and Tube 3 are eventually present when $d = 3$ nm due to the fluctuation of each tube about its initial equilibrium position. Thus the data can be segmented into two distinct cases. In the first case the initial separation distance is such that there are no direct interactions between Tubes 2 and 3 and the conductance per junction is unaffected by the presence of the neighboring junction. In the second case the initial separation distance is small enough to allow an attractive force between Tubes 2 and 3. The two tubes are drawn to their equilibrium separation distance and conductance per junction decreases by $\sim 10\%$.

The conductance across a CNT-CNT junction has been shown to be unaffected by the presence of neighboring junctions when separated further than the range of direct van der

Waals interactions. When junctions are separated by the equilibrium separation distance of the two neighboring tubes, the conductance per junction is reduced by only $\sim 10\%$. This is in contrast to a previous study that claimed a reduction by approximately one order of magnitude [8]. Given that poor CNT-CNT conductance is known to be the limiting factor in thermal transport in CNT networks, the findings presented here have important implications for improving thermal performance in CNT-based materials. Increasing the contact density of CNT junctions will only improve the overall thermal transport when the arrangement is such that the CNTs creating the junction do not have direct van der Waals interactions with each other. Even when the CNTs that make up the adjacent junctions are in direct contact with each other (are separated by the equilibrium distance), the reduction of the contact conductance at each junction is only $\sim 10\%$. These findings suggest that overall CNT-CNT conductance can be increased by increasing the number of CNT-CNT contacts.

4.2.3 Effect of Contact Area between Parallel CNTs

The dependence of the conductance at the interface between two partially overlapping parallel CNTs on the length of the overlap is investigated in a series of simulations. The computational setup used in these simulations is shown in Fig. 4.7. Periodic boundary conditions are used in the axial direction (along the x-axis), while free boundary conditions are applied in other directions. The two CNTs have the same length of 100 or 200 nm and are covered by 110-atom caps at the ends with one of the caps interfacing with the nanotube by a 20-atom ring constituting a half of the nanotubes unit cell. This series of simulations employs a different interatomic potential than the series of simulations described in Sections 4.2.1 and 4.2.2. Here, the LAMMPS implementation of the AIREBO potential [111] is used to describe the interatomic interactions. This implementation adopts the 2nd generation REBO potential [103] for chemically bonded carbon atoms within the CNTs and describes the van der Waals interactions between non-bonded carbon atoms by the Lennard-Jones potential with parameters $\sigma = 3.40 \text{ \AA}$ and $\epsilon = 2.84 \text{ meV}$. A cutoff func-

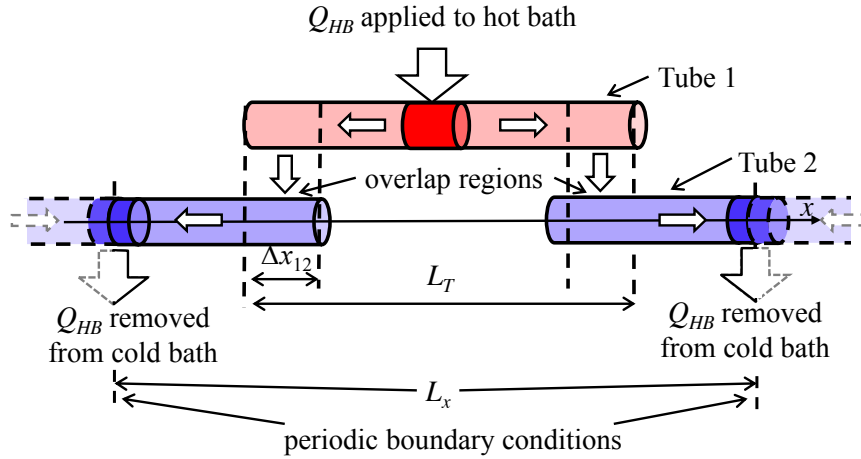


Figure 4.7: Computational setup used in MD simulations of the conductance through overlap regions between parallel CNTs. Block arrows indicate the directions of the heat flow. The flux across the overlap regions is created by adding energy at a constant rate Q_{HB} in the heat bath region in the center of Tube 1 and removing it from the heat bath region in the center of Tube 2. Each of the heat bath regions has length of 2 nm. Periodic boundary conditions are applied in the axial direction.

tion that ensures a smooth transition of the Lennard-Jones potential to zero is applied in a range of interatomic distances from 2.16σ to 3σ [111].¹ The equations of motion are solved using the velocity Verlet algorithm and the timestep of integration is 0.5 fs.

The length of the overlap region, Δx_{12} , is systematically varied in the range of 10 to 95 nm, leading to the corresponding variation of the size of the computational cell in the x-direction, $L_x = 2L_T - 2\Delta x_{12}$, where L_T is the length of the CNTs. Similar to simulations described in Sections 4.2.1 and 4.2.2, the initial systems are relaxed by quenching atomic velocities for 10 ps and brought to 300 K by applying the Langevin thermostat for 30 ps. A constant heat flux is then generated by scaling the velocities of atoms in two 2 nm wide heat bath regions defined in the centers of the two CNTs, so that the same amount of energy, $Q_{HB} = 0.4 \text{ eV ps}^{-1}$ for 100 nm CNTs and $Q_{HB} = 1.0 \text{ eV ps}^{-1}$ for 200 nm CNTs, is added and removed per unit time in the two heat bath regions, as shown in Fig. 4.7. The thermal

¹The cutoff of the nonbonding interaction potential at large distances is not explicitly discussed in Ref. 111 but is used in the computational code implementing the AIREBO potential and provided to us by Steven Stuart of Clemson University. The values of 2.16σ to 3σ are from the code.

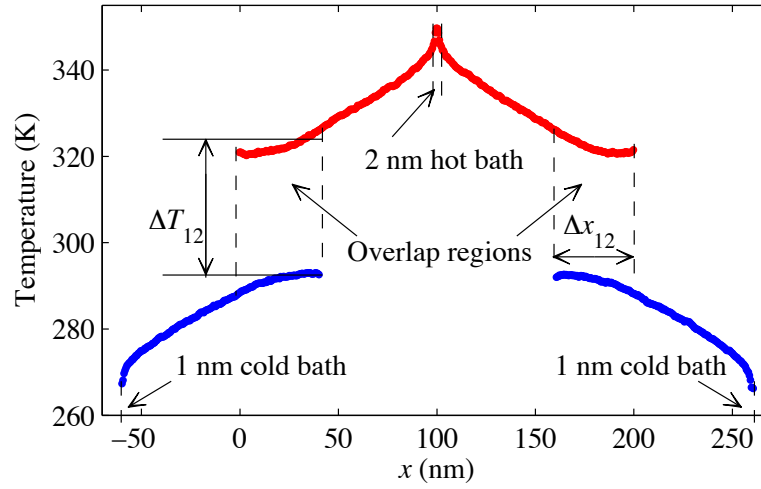


Figure 4.8: A representative temperature distribution in the overlapping Tubes 1 (red curve) and 2 (blue curve) obtained by averaging data over 6.7 ns in the steady-state regime of a simulation performed for (10,10) CNTs with length $L_T = 200$ nm and overlap length $\Delta x_{12} = 40$ nm. The temperature drop at the inter-tube contact, ΔT_{12} , is calculated as the difference of the average temperatures of the overlapping CNT segments.

energy is conducted from the center of the hot CNT, out to the overlap regions, across to the cold CNT by inter-tube conductance, and finally to the heat bath in center of the cold tube.

Steady-state temperature distributions are established in the simulations by the time of 1.5 to 4.5 ns, depending on the values of L_T and Δx_{12} . The simulations are continued in the steady-state regime for an additional period of 4 to 7.7 ns in order to collect data for evaluation of the inter-tube conductance. A representative temperature profile averaged over a period of 6.7 ns in the steady-state regime is shown in Fig. 4.8 for $L_T = 200$ nm and $\Delta x_{12} = 40$ nm. Given that the heat flux through each of the two overlap regions is $Q_{HB}/2$, the values of the effective inter-tube conductance per unit overlap length, σ_T , is calculated as $\sigma_T = Q_{HB}/(2\Delta T_{12}\Delta x_{12})$, where ΔT_{12} is the temperature jump at the CNT-CNT contact defined as the difference of temperatures averaged over the overlap regions in each tube. The calculation of the inter-tube conductance is done by collecting “instantaneous” (averaged over sequential 1 ps windows) values of ΔT_{12} , calculating the corresponding instantaneous values of σ_T , and obtaining the average conductance σ_T and the sample

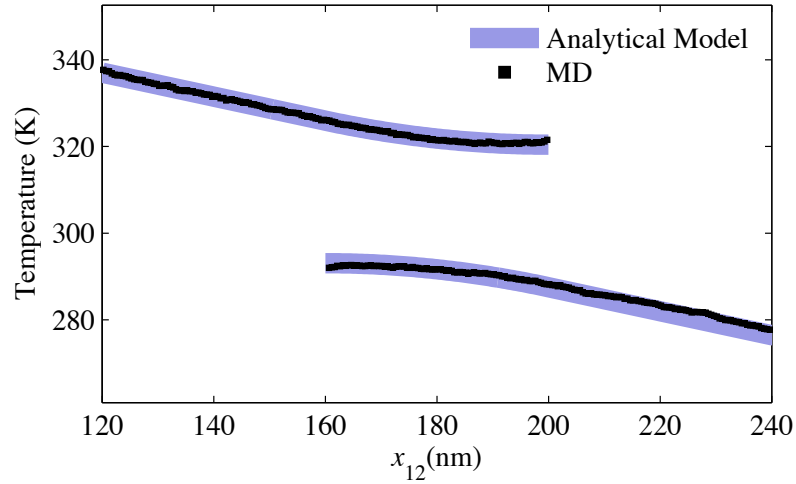


Figure 4.9: Comparison of the temperature distributions in the vicinity of the overlap region obtained from the predictions of an analytical solution (thick light curve) and the MD simulation (black dots). The temperature profile corresponding to predictions of the MD simulation was obtained by averaging data over 6.7 ns in the steady-state regime.

standard deviation from the data collected over the steady-state part of the simulation.

To determine the dependence of σ_T on the length of the overlap region, the simulations are performed for Δx_{12} ranging from 10 to 45 nm for $L_T = 100$ nm and from 10 to 95 nm for $L_T = 200$ nm. The calculated values of σ_T are shown in Fig. 4.10 by solid squares and circles for simulations performed for 100 and 200 nm CNTs, respectively. The sample standard deviation is also presented as a measure of uncertainty. All data points are confined within a relatively narrow range from 0.057 to 0.065 Wm⁻¹K⁻¹, and are all within one sample standard deviation of each other, thus suggesting that σ_T is independent of the overlap length.

This last conclusion is also justified by the comparison of temperature distributions obtained in the MD simulations with the ones predicted by an analytical solution of the one-dimensional steady-state heat conduction equations for partially overlapping nanotubes, Fig. 4.9. The analytical solution is obtained under assumption of constant values of the intrinsic thermal conductivity of the interacting nanotubes, k , and inter-tube conductance per unit length, σ_T . This analytical model was developed by colleague Alexey Volkov

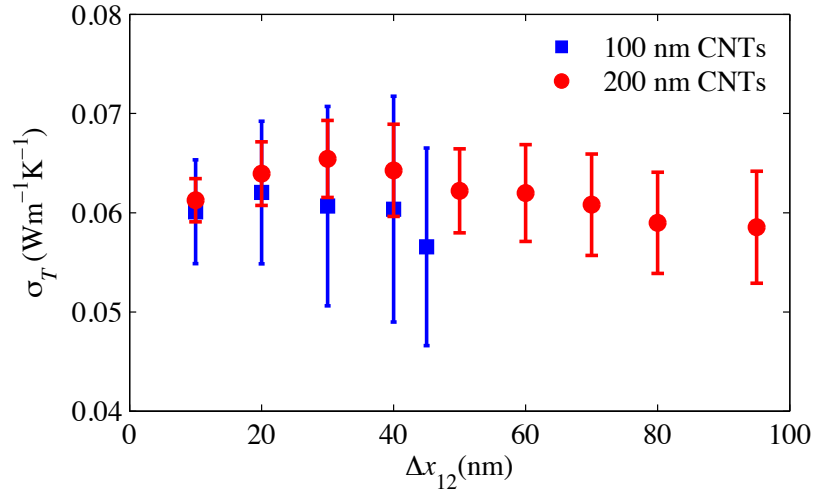


Figure 4.10: Inter-tube conductance per unit length, σ_T , versus overlap length, Δx_{12} , obtained in MD simulations for two parallel partially overlapping (10,10) CNTs of 100 nm (blue squares) and 200 nm (red circles) length. The computational setup used in the simulations is shown in Fig. 4.7. The error bars show one sample standard deviation calculated for “instantaneous” values of inter-tube conductance collected during the steady-state part of the simulation.

and is described in detail in Appendix A of Ref. 76. The inter-tube conductance per unit length in the theoretical model is defined by the same equation that has been used for analysis of results of atomistic simulations, $\sigma_T = Q_{HB}/(2\Delta T_{12}\Delta x_{12})$. The theoretical temperature profiles obtained with Δx_{12} , Q_{HB} , ΔT_{12} , and k taken from the MD simulation are in very good quantitative agreement with the time-average MD temperature distributions (Fig. 4.9). Small deviations of the MD results from the theoretical curve observed for the right (lower-temperature) CNT can be explained by the temperature dependence of k (k increases and, for fixed heat flux, $|dT/dx|$ decreases with decreasing T in the range of temperatures used in the MD simulations[18, 23, 24]) that is not accounted for in the theoretical model. The good overall agreement between the theoretical model and the results of MD simulations provides an additional support to the assumption of the constant inter-tube conductance per unit length used in the theoretical model.

The values of the inter-tube conductance obtained in this work, $\sim 0.06 \text{ Wm}^{-1}\text{K}^{-1}$, are consistent with the results of similar MD simulations reported in Ref. 6 for shorter 25 to 75

nm long (10,10) CNTs, where the conductance of $0.05 - 0.08 \text{ Wm}^{-1}\text{K}^{-1}$ is predicted for overlap lengths ranging from 4 to 9.5 nm. Comparable values of $0.03 \text{ Wm}^{-1}\text{K}^{-1}$ and of $0.048 \text{ Wm}^{-1}\text{K}^{-1}$ can be calculated from the results of MD simulations performed for two parallel 20 nm long (10,10) CNTs [7] and two parallel 4.3 nm long (10,0) CNTs embedded into “frozen” matrix [45]², respectively. On the other hand, an order of magnitude smaller value of $0.0048 \text{ Wm}^{-1}\text{K}^{-1}$ can be drawn³ from the results of MD simulations of non-stationary heat transfer in a bundle of seven (5,5) CNTs reported in Ref. 44. Similarly small values of σ_T can also be calculated from data reported in Ref. 5 for MD simulations performed for 5 to 40 nm long (10,10) CNTs, where the overlap length is varied from 2.5 to 10 nm.

More importantly, the values of inter-tube conductance reported in Ref. 5, when expressed in units of $\text{Wm}^{-1}\text{K}^{-1}$, exhibit a strong dependence on the overlap length, e.g., $\sigma_T \approx 0.0065 \text{ Wm}^{-1}\text{K}^{-1}$ for 2.5 nm overlap length, $\sigma_T \approx 0.0034 \text{ Wm}^{-1}\text{K}^{-1}$ for 5 nm overlap length, and $\sigma_T \approx 0.0018 \text{ Wm}^{-1}\text{K}^{-1}$ for 10 nm overlap length are predicted in simulations performed for 20 and 40 nm long CNTs. This observation of a strong overlap length dependence of σ_T is in a sharp contrast with findings of the present study and can be attributed to the small values of Δx_{12} and L_T considered in Ref. 5. Indeed, a moderate decrease of σ_T with increasing Δx_{12} is also observed in Ref. 6, where the values of $0.08 \text{ Wm}^{-1}\text{K}^{-1}$ and $0.05 \text{ Wm}^{-1}\text{K}^{-1}$ can be estimated for (10,10) CNTs from the data shown for 4 and 9.5 nm overlap lengths, respectively. For longer overlap lengths of 10 to 95 nm considered in the present study, no statistically significant variation of σ_T can be inferred from the results shown in Fig. 4.10.

The fixed boundary conditions at the ends of the interacting CNTs and the short length

²The values of interface conductance given in Ref. 45 in units of $\text{Wm}^{-1}\text{K}^{-1}$ (Figs. 6 and 7) are about an order of magnitude larger than the actual values found in the simulations, as established through private communication with Dr. Vikas Varshney.

³The values of the thermal boundary conductance between CNTs in a bundle reported in Table 4 of Ref. 44 are twice smaller than its actual value found in the simulations and the value of the surface area is twice higher than the value reported in this table, as established through private communication with Professor Junichiro Shiomi. The conductance in units of WK^{-1} or $\text{Wm}^{-1}\text{K}^{-1}$, however, is not affected by these corrections.

of the CNTs used in Ref. 5 could be additional factors responsible for both the strong overlap length dependence of σ_T and the small values of the conductance observed in this work. The dependence on the CNT length is especially pronounced for $L_T < 10$ nm and is weaker as the length is increasing from 10 to 40 nm [5]. The observation of the pronounced CNT length dependence for short CNTs is consistent with the results of an MD simulation study of the interfacial conductance between a (5,5) CNT and a surrounding octane liquid [141], where an increase in the interfacial conductance per CNT area with increasing nanotube length is observed up to a length of ~ 3.5 nm and attributed to the extinction of low frequency phonons in short CNTs. A very weak dependence on the CNT length is reported in Ref. 6 for L_T ranging from 25 to 75 nm and no statistically significant difference between the results shown in Fig. 4.10 for 100 and 200 nm long CNTs is observed.

Overall, the results of the simulations reported in literature and obtained in the present study suggest that the conductance between partially overlapping parallel CNTs is proportional to the length of the overlap (the conductance per length is constant) for conditions relevant to bundles present in real CNT materials, when the CNTs and CNT-CNT overlaps are longer than several tens of nanometers. This conclusion is also consistent with the results of experimental measurements of the thermal conductance between a single walled CNT and a silica substrate, which suggest that the net value of the thermal conductance is proportional to the length of the CNT [144].

4.2.4 CNT-CNT Contacts of Arbitrary Configuration

A series of simulations was performed to investigate the effect of contact area on conductance at the interface between two overlapping CNTs forming a junction with angle θ between them. The computational setup used in these simulations is shown in Fig. 4.11. Adjusting the value of θ results in alterations of the physical configuration of the junction and allows the contact area to be varied from a minimum value when $\theta = 90^\circ$ to a maxi-

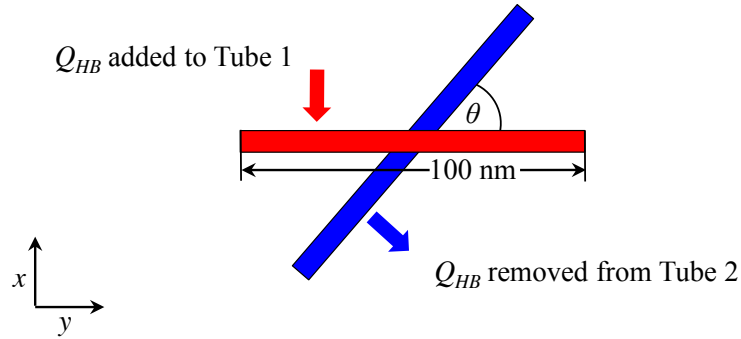


Figure 4.11: A schematic of the computational setup employed to investigate the effect of contact area on conductance at a CNT-CNT junction. Energy is uniformly added to Tube 1 and uniformly removed from Tube 2 at a rate of Q_{HB} . The lengths of both tubes are fixed at 100 nm and the angle θ is varied between simulations.

mum value when $\theta = 0^\circ$. Free boundary conditions are applied in all directions. The two CNTs have the same length of 100 nm and are covered by 110-atom caps at the ends with one of the caps interfacing with the nanotube by a 20-atom ring constituting a half of the nanotubes unit cell. Just as in the simulations discussed in Sections 4.2.1 and 4.2.2, the Tersoff potential [100] describes interactions between carbon atoms belonging to the same CNT and a Lennard-Jones potential describes the non-bonded van der Waals interactions between atoms belonging to different CNTs, with Lennard-Jones parameters $\sigma = 3.41 \text{ \AA}$ and $\epsilon = 3.0 \text{ meV}$. The equations of motion are solved using the velocity Verlet algorithm and the timestep of integration is 1 fs.

All configurations are relaxed by quenching atomic velocities for 0.25 ns to establish an equilibrium separation between the nanotubes in the contact region and to prevent non-thermal oscillations that would affect inter-tube interactions. The temperature of each CNT is determined from Eq. 2.1 and the systems are then gradually heated to 300 K by applying the Langevin thermostat for 0.25 ns [123]. For configurations where initial θ is greater than 0° , the separation distance between CNTs in the region surrounding the contact area is

greater than the equilibrium separation distance between parallel CNTs. Attractive van der Waals forces cause the CNTs to bend and minimize the interaction energy in this region. This distortion results in additional attractive forces between the CNTs as different regions are brought into the range of van der Waals interactions. The process continues until the CNTs are completely parallel which is the lowest energy configuration. To inhibit this process, a small spring force is applied to the ends of each CNT to prevent the CNTs from becoming parallel. The implementation of the spring force is similar to the implementation that is described in detail in Section 4.2.1 and has the same spring constant of $K_{Spr} = 0.0003 \text{ eV } \text{\AA}^{-2}$. However, instead of applying the force evenly to all atoms in the CNTs, the spring force is applied only to the 150 atoms at each end of each CNT. This corresponds to the 110-atom cap and adjacent 40-atom nanotube unit cell on each nanotube end. In this way, the extreme ends of each CNT are tethered to their original positions by a spring force while the main central region of each CNT is allowed to bend and distort around the contact area. Thus, while the initial input angle θ is not explicitly preserved around the contact area, the final contact area may be adjusted by variations in the input parameter θ . For consistency, the spring force is applied to the ends of each CNT during the preparation of every configuration, including $\theta = 0^\circ$.

After the sample preparation, a constant heat flux is then generated by scaling the velocities of all atoms in each CNT so that the same amount of energy, Q_{HB} , is added to Tube 1 and removed from Tube 2 per unit time. The thermal energy is conducted from Tube 1 across to Tube 2 by inter-tube conductance in the region of the CNT-CNT contact where the tubes are separated by less than the Lennard-Jones cutoff distance of 1 nm. This results in a temperature difference between the two tubes, ΔT_{12} , which eventually reaches a steady-state value that is related to the applied heat flow rate, Q_{HB} , and CNT-CNT conductance, G , by the expression $G = Q_{HB}/\Delta T_{12}$. The overall conductance G differs between simulation configurations due to variations in the area in which inter-tube interactions are present. Thus, the value of the heat flow rate Q_{HB} is varied between 0.08 eV ps^{-1} and 3.0 eV ps^{-1} .

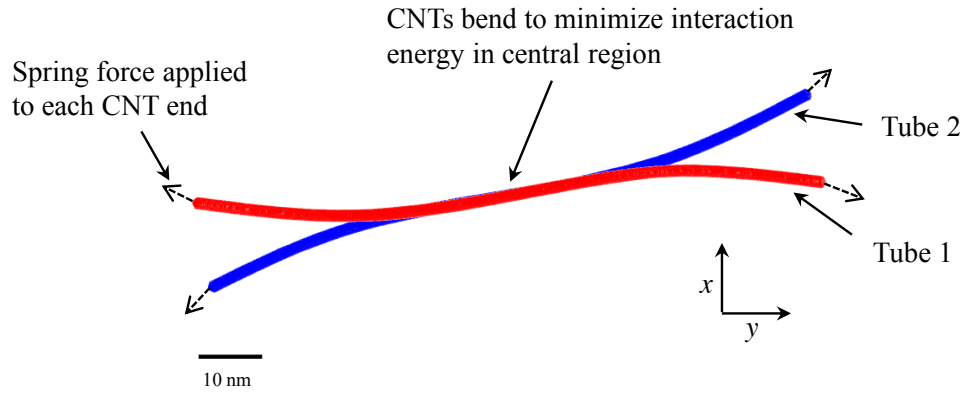


Figure 4.12: A representative plot of atomic positions recorded during the constant flux implementation for the configuration where initial $\theta = 20^\circ$. The central region of each CNT deforms to minimize the inter-tube interaction energy, thus altering the local configuration at the junction. A spring force with spring constant $K_{Spr} = 0.01 \text{ eV } \text{\AA}^{-2}$ is applied to the 150 atoms in the ends of each CNT to prevent complete alignment of the CNTs.

for different simulations in order to obtain similar values of ΔT_{12} for all configurations.

Non-parallel configurations with low initial values of θ experience greater CNT deformation in the contact region resulting in a greater attractive force between CNTs as compared to configurations with greater values of θ . For the two cases where $\theta = 20^\circ$ and $\theta = 35^\circ$ the attractive forces were sufficient to overcome the original small spring force and cause the CNTs to completely align with each other during the time of constant flux implementation. Thus, the spring constant used during constant flux implementation for these two cases was increased from the original value used during sample preparation to $K_{Spr} = 0.01 \text{ eV } \text{\AA}^{-2}$. An instantaneous snapshot of the atomic coordinates recorded during constant flux implementation for the configuration where $K_{Spr} = 0.01 \text{ eV } \text{\AA}^{-2}$ and the original input parameter $\theta = 20^\circ$ is plotted in Fig. 4.12. Due to the low value of θ , the CNTs experience greater attractive van der Waals forces and require a stronger spring force to prevent complete overlap as compared to configurations with higher initial values of θ . While the original contact area between CNTs and the initial orientation angle θ are not maintained during the constant flux implementation, the steady-state configuration can still

be controlled by variations in the input parameter θ . The parallel configuration remain stable in the absence of a small spring force. Therefore, the small spring force was omitted during the time of constant flux implementation for the simulation where $\theta = 0^\circ$. The original spring constant of $K_{Spr} = 0.0003 \text{ eV } \text{\AA}^{-2}$ was maintained for all other configurations where $\theta > 35^\circ$.

To examine the effect of the spring force implementation, the case where $\theta = 0^\circ$ was repeated while maintaining the original spring force for the entire simulation duration. The final predicted value of CNT-CNT G between parallel 100 nm CNTs with spring forces applied to each CNT end was 0.3% greater than the predicted value of G for of the same configuration when the spring forces were not applied during the constant flux implementation. The predicted values for the two cases are in good agreement with each other given the 2.8% measure of uncertainty for each case, providing support for the conclusion that the inclusion of the spring force did not have a significant effect on the final predicted values of G . Final results reported below for the parallel configuration are for the case when the spring forces were not applied during the constant flux implementation.

A moving average of each CNT's temperature is calculated over a 50 ps temporal window using a procedure similar to the temporal averaging procedure described in Section 4.2.1. A moving average of G is calculated over the same 50 ps temporal window from the constant heat flow rate, Q_{HB} , and a moving average of ΔT_{12} , which is the difference between the moving average temperature of Tube 1 and the moving average temperature of Tube 2. The temporal evolution of the moving average calculation of G is used to determine achievement of the steady state. The time required to reach the steady state scales with the overall conductance value, which is dependent on the total contact area. Thus, the duration of time for which the temporal evolution was monitored varied between simulations and was within the range of 8 ns to 30 ns. After achievement of the steady state, the constant flux implementation is continued for an additional 1 ns. The temporal averaging procedure is abandoned and *instantaneous* values of the prediction of G are recorded every 100 ps.

This produces a sample set of 10 values of the prediction of G in the steady state. The final value of the prediction of G is taken as the sample mean of this sample set and one sample standard deviation is given as a measure of uncertainty.

Defining the area of contact between two overlapping cylindrical objects is non-trivial. Previous MD investigations of conductance between partially overlapping, parallel CNTs have considered the interfacial region as a single planar interface between two coaxial CNTs joined end to end [5, 6]. The contact areas used in calculations of interfacial thermal resistance per area and interfacial thermal conductance per area in Ref. 5 and Ref. 6, respectively, are represented by the cross-sectional area of a single CNT regardless of the overlap length. The present study investigates conductance between overlapping, non-parallel CNTs which form junctions that do not have an easily defined length of overlap, as can be seen from Fig. 4.12. Moreover, the motivation for this study is to provide results that will be used in the formation of a general model of CNT-CNT conductance for junctions of arbitrary configuration. Therefore, a more robust characterization of the contact region is needed.

An accurate representation of the contact area between two CNTs differs from the representation of the contact area in a traditional material interface in two major ways. First, rather than a single, well defined planar interface between two chemically bonded materials, the region of interaction between two CNTs is defined by two curved surfaces with different surface elements separated by different distances. Second, due to the largely one-dimensional nature of CNTs, the periphery region of the contact accounts for a significant fraction of the CNTs regions contributing to the inter-tube interaction. The combination of these two factors causes heterogeneity of the local environment throughout the contact region which prevents the consideration of any accurately representative elemental area.

It is intuitive to consider the contact area between CNTs to be related to the number of inter-tube interactions as these interactions will be responsible for inter-tube conductance. The total number of interatomic interactions between CNTs in the MD simulations can

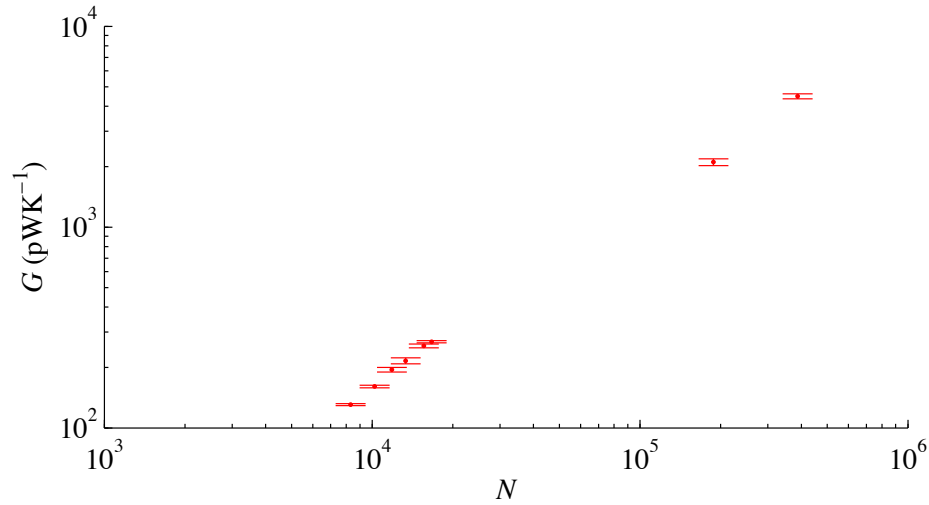


Figure 4.13: Predicted values of G are plotted with respect to the total number of interatomic interactions between CNTs, N . Error bars represent one sample standard deviation of the sample set of predictions of G and are provided as a measure of uncertainty. Total conductance is observed to increase with increasing N .

be determined by the total number of atomic pairs shared between both CNTs that are separated by less than 1 nm, i.e., the cutoff distance of the Lennard-Jones potential. The total number of interatomic inter-tube interactions was evaluated at each timestep for which an instantaneous value of the prediction of G from the MD method was recorded in the steady state to produce a sample set of 10 calculations. The total number of interactions between CNTs, N , is taken as the mean of this sample set and is used to characterize the contact region for each simulation configuration. The final value of G is plotted with respect to the total number of interatomic interactions for each simulation in Fig. 4.13. Error bars represent one sample standard deviation of the sample set of G values and are provided as a measure of uncertainty.

As can be seen in Fig. 4.13, the predicted values of conductance, G , increase with increasing number of interatomic interactions, N . This trend is reasonable considering that N characterizes the level of interaction responsible for thermal conductance. A more interesting trend is observed when the conductance *per* interaction, G/N , is considered. The values of G and standard deviation indicated by the error bars in Fig. 4.13 are divided

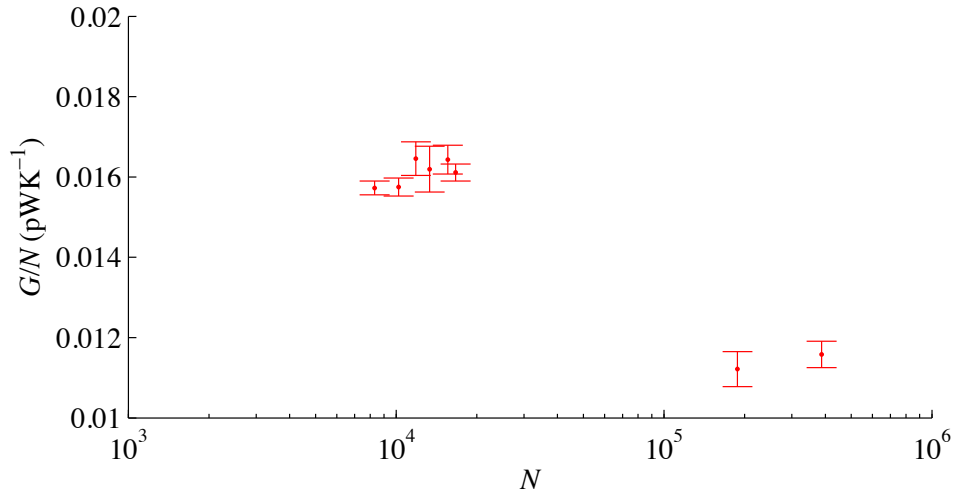


Figure 4.14: Values of the average conductance per inter-tube interaction, G/N , plotted with respect to the total number of interatomic interactions between CNTs, N . The ranges of the error bars are determined by dividing the sample standard deviations of G predictions by the values of N for each configuration and are provided as a measure of uncertainty. The data consist of two distinct groups, with configurations with relatively low values of N (i.e., initial $\theta \geq 35^\circ$) having values of G/N which are all similar to each other and higher than the values of G/N for configurations with higher values of N (i.e., initial $\theta = 20^\circ$ and 0°), which are also similar to each other.

by N to characterize the average conductance per interatomic interaction and plotted with respect to N in Fig. 4.14. Results fall into two distinct groupings where configurations with initial $\theta \geq 35^\circ$ have a total number of interactions ranging from $\sim 8.3 \times 10^3$ to $\sim 1.7 \times 10^4$ and configurations with initial $\theta = 20^\circ$ and $\theta = 0^\circ$ have $\sim 1.9 \times 10^5$ and $\sim 3.9 \times 10^5$ total interactions, respectively. Moreover, all values of G/N for the grouping of configurations with lower N are similar to each other and greater than the values of G/N for the grouping of configurations with greater N , which are also similar to each other.

The nature of the variation of G/N suggests that there is a distinct difference between the two groupings of configurations. Conductance per unit overlap length, σ_T , between partially overlapping parallel CNTs was observed to be constant for overlap lengths of more than several tens of nanometers in Section 4.2.3. These results support the idea that the distinct difference between values of G/N for the two groupings of configurations is not simply due to variation in contact area or N alone. There appears to be a characteristic

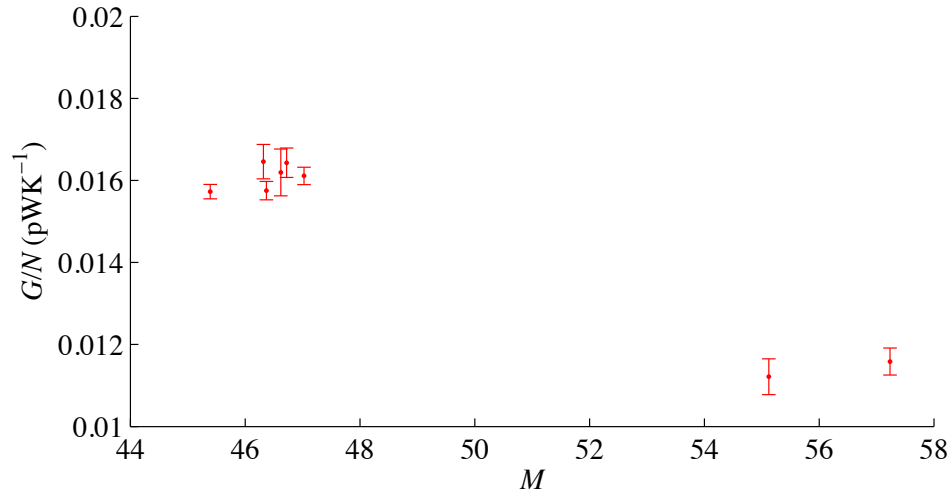


Figure 4.15: Predicted values of the average conductance per inter-tube interaction, G/N , are plotted with respect to the average number of inter-tube interactions per atom in the contact region, M . The ranges of the error bars are determined by dividing the sample standard deviations of G values by the values of N for each configuration and are provided as a measure of uncertainty. The data form two distinct groups, with configurations with initial $\theta \geq 35^\circ$ having relatively lower values of M due to a greater proportion of atoms in the contact regions being located in the periphery of the contact. Greater predicted values of G/N are observed for configurations with relatively lower values of M , suggesting conductance per interaction is greater in areas with less inter-tube interactions.

difference between the two groupings that is not fully captured by N . Further investigation into the geometry of the contact regions reveals another distinct difference between the two groupings of configurations. For each configuration, the average number of inter-tube interactions per atom in the contact region, M , is taken as twice the total number of van der Waals interatomic interactions divided by the total number of atoms involved in inter-tube interactions. This value provides a measure of the average number of interatomic inter-tube interactions experienced by each atom in the inter-tube interaction region.

Similar to the calculation procedure for N , sample calculations of M are taken for each timestep for which an instantaneous value of G was recorded and the final value of M is taken as the mean of this sample set. Calculations of G/N are plotted with respect to M for each configuration in Fig. 4.15. Just as in Fig. 4.14, the data divide into two groupings. The values of M for configurations with initial $\theta \geq 35^\circ$ fall within a range from 45.4 to

47.0 and configurations with initial $\theta = 20^\circ$ and $\theta = 0^\circ$ have values of $M = 55.1$ and $M = 57.2$, respectively. It is reasonable that configurations with higher initial values of θ would have a lower average number of interatomic inter-tube interactions in the contact region as compared to configurations with lower initial values of θ . Atoms located at the periphery of a contact region have less inter-tube interactions than atoms located in the center of a contact region. The geometries of the configurations with high initial values of θ are such that the peripheries of the contact regions account for a higher fraction of the overall contact regions. Thus, these configurations will have less average number of inter-tube interactions per atom.

The grouping of configurations with lower values of M are observed to have higher values of G/N as compared to the grouping of configurations with higher values of M . This suggests that the conductance per area is greater at the periphery of contact regions or where there are less inter-tube interactions per area. This result is in contrast the findings of an MD study by Evans et al. [7] which investigated the conductance between 20 nm CNTs forming cross-junctions with different angles of orientation, θ . The authors conclude that the conductance between CNTs is directly proportional to the contact area between the CNTs, for values of θ from 0° to 90° . However, the finding of the current study is consistent with the results of the studies by Zhong and Lukes [5] and Xu and Buehler [6] which are discussed in Section 4.1.3 and suggest the conductance per overlap length between parallel partially overlapping CNTs is greater for small overlap lengths which correspond to contact areas where the periphery of the contact region accounts for a higher fraction of the overall contact area. These findings provide the motivation for a series of simulations designed to investigate the effects of the local density of inter-tube interactions on the conductance per area across Lennard-Jones interfaces, the details and results of which are discussed in the next chapter.

4.3 Summary

Systematic evaluation of the sensitivity of the values of CNT-CNT conductance predicted in MD simulations to the structural parameters of the CNT-CNT contact were performed. Results of a series of simulations designed to investigate the effects of CNT length on CNT-CNT conductance demonstrate a stronger length dependence preserved over a longer range of CNT lengths than has been previously reported. Linear extrapolation predicts a saturated value of G_∞ that is 48% higher than predicted in a similar, though less extensive, study [7]. The length required to reach 95% of G_∞ , $L_{0.95} = 59$ nm, is found to be 40% longer than the respective $L_{0.95}$ found in the earlier study. Therefore, greater conductance than previously predicted can be achieved when CNT lengths are greater than ~ 60 nm.

The conductance across a CNT-CNT junction has been shown to be unaffected by the presence of neighboring junctions when the junctions are separated further than the range of direct van der Waals interactions between the nanotubes in a series of simulations designed to study the effect of contact density. When junctions are separated by the equilibrium separation distance of the two neighboring nanotubes, the conductance per junction is reduced by only $\sim 10\%$. This is in contrast to a previous study that claimed a reduction by approximately one order of magnitude [8]. Increasing the contact density of CNT junctions will only improve the overall thermal transport.

Results of a series of simulations performed to investigate the effect of contact area on CNT-CNT conductance demonstrate that the conductance between partially overlapping parallel CNTs is proportional to the length of the overlap (the conductance increases monotonically with increasing overlap length) for conditions relevant to bundles present in real CNT materials, when the CNTs and CNT-CNT overlaps are longer than several tens of nanometers. In contrast to this finding, the results of a series of simulations studying the conductance between non-parallel configurations with small contact areas demonstrate a non-linear dependence of conductance on the number of inter-tube interactions between

CNTs. The conductance per inter-tube interaction is shown to be dependent on the average number of inter-tube interactions per atom in the contact region.

These findings have implications for the optimization of thermal transport in CNT-based materials which is largely limited by the low CNT-CNT conductance. Overall conductance in the CNT material can be improved by increasing CNT length, and density and area of CNT-CNT contacts. Conductance per area may be sensitive to the density of inter-tube interactions. A description and the results of a series of simulations designed to further investigate this sensitivity are provided in Chapter 5.

Chapter 5

Thermal Conductance between Two-Dimensional Lennard-Jones Materials

5.1 Background

As discussed in Section 4.2.4, the results of a series of simulations designed to investigate the CNT-CNT conductance for configurations of non-parallel CNTs with varying area of inter-tube interaction suggest that the conductance per area is greater at the periphery of the contact regions or where there are less interatomic inter-tube interactions per area. In other words, conductance per area may be dependent on the density of interatomic inter-tube interactions. In Section 4.2.4, the average number of interatomic inter-tube interactions per atom in the contact region, M , is defined as a measure of the average density of interatomic interactions between CNTs in the contact region. Modifying the geometric configuration of the contact region by varying the initial angle between CNTs, θ , results in variation in the values of M between different simulations. The conductance per interatomic inter-tube interaction, G/N , is observed to be higher for configurations with lower values of M . However, these variations in M also correspond to variations in other structural parameters such as the total number of interatomic inter-tube interactions, N , and the angle between CNTs. Therefore, the motivation for the computational investigations re-

ported in this chapter is to study the sensitivity of conductance to the density of interatomic interactions *in isolation* of variation in other geometric parameters.

The Lennard-Jones (LJ) potential is an attractive choice of interatomic potential for the simulation series reported in this chapter, where the goal is a qualitative understanding of the effects of the density of interatomic interactions rather than an accurate quantitative prediction of thermal conductance. Without loss of generality, simplistic LJ “toy” models allow for qualitative and controlled investigation of physical trends in systems that are not material specific. The simplicity of the LJ potential can facilitate the investigation of phenomena that may be obscured in more complex systems [94]. Moreover, the motivation for this work comes from results of a previous MD investigation of thermal conductance between CNTs via van der Waals interactions which are commonly described by the LJ potential.

In addition to being generalizable, the simplicity of LJ “toy” models allow for unique adaptations of the computational setup to examine theoretical, non-physical systems. Non-equilibrium MD (NEMD) simulations are performed to investigate the thermal conductance across an interface between two-dimensional (2D) LJ materials. The motivation for this series of simulations is to examine the effects of the density of interatomic interactions between the two LJ materials while minimizing the variation of other parameters such as structural geometry and contact area. To achieve this goal, a unique computational setup is employed and is described in detail in Section 5.3.2.

5.2 General Computational Procedure

Simulations are designed to predict the thermal conductance across an interface between 2D LJ materials. While some procedures are varied across different simulations, the sample preparation and computational procedure for a reference simulation are outlined in this section. Results from all other simulations will be compared to results from this

reference simulation, and deviations from the reference procedure will be noted.

Simulations are performed for a 2D atomic plane. Initial atomic positions are determined by the projection of a hexagonal lattice onto a rectangular computational cell domain with dimensions 40.5×99.5 unit cells. This produces 199 rows of atoms with lengths alternating between 40 and 41 atoms, yielding 8060 total atoms. The sample contains two LJ materials comprised of different types of atoms. Rows 1-100 (4050 atoms) are designated as Type 1 atoms and form Material 1, and rows 101-199 (4010 atoms) are designated as Type 2 atoms and form Material 2.

Interatomic interactions are described by the LJ potential. All values are presented in LJ reduced units, where nondimensional values (denoted by “*”) are related to the corresponding real values by

$$\begin{aligned}
 r^* &= r/\sigma, \\
 E^* &= E/\epsilon, \\
 m^* &= m, \\
 T^* &= Tk_B/\epsilon, \\
 t^* &= t\sqrt{\epsilon/(m\sigma^2)},
 \end{aligned} \tag{5.1}$$

for distance r , energy E , mass m , temperature T , and time t , where k_B is the Boltzmann constant. Here, σ and ϵ represent the LJ distance and energy parameters respectively, for interactions between Type 1 and Type 2 atoms, and m is the mass of Type 1 atoms. As all remaining values will be presented in LJ reduced units, the “*” is no longer necessary and will be omitted. Thus, $\sigma_{12} = 1$ and $\epsilon_{12} = 1$ define interactions between Type 1 and Type 2 atoms, $\sigma_{xx} = 1$ and $\epsilon_{xx} = 4$ define interactions between atoms of the same type, the mass of both types are equal (i.e., $m_1 = m_2 = 1$), and the cutoff radius for all interactions is $r_c = 2.5$.

Simulations are performed with the LAMMPS package [107]. The equations of motion are solved using the velocity Verlet algorithm and the timestep of integration is 0.005. The computational domain is two-dimensional and free (vacuum) boundary conditions are applied in both directions. Initially a uniform distribution of velocities is randomly distributed

among the atoms resulting in an average system temperature of $T_{sys} = 0.2$ after equipartition of energy.

The thermal conductance across the interface between the two materials is determined from NEMD simulations by generating a constant heat flux between hot and cold bath regions defined in the atomic plane. The heat flux is applied by adding and removing a known amount of energy at a constant heat flow rate Q_{HB} through the scaling of the velocities of atoms in the hot and cold heat bath regions. Energy is removed from the 770 Type 1 atoms in rows 1-19 and added to the 770 Type 2 atoms in rows 181-199 at a rate of $Q_{HB} = 6$ for a duration of $t = 3 \times 10^4$ (6×10^6 timesteps).

The implemented flux creates a non-equilibrium temperature profile in the sample, which is determined by the implemented flux, the conductivities of both LJ materials, and the interfacial conductance between the two materials. The temperature profile is obtained by dividing the sample into segments and calculating the local temperature of each segment from the average kinetic energy of the corresponding atoms. The procedure is similar to the procedure described in Section 3.2.1 but modified for a 2D LJ system. A representative temperature profile is shown in Fig. 5.1. The width of each segment is 0.64 which corresponds to the average separation distance between rows of atoms within the same material. The temperature profiles of Material 1 and Material 2 are represented by blue and red circles, respectively. The two black curves represent two linear fits applied independently to each temperature profile, with the heat bath regions and the first five segments adjacent to either the heat bath regions or the interface excluded from the fitting procedure. Non-linear effects cause the temperature profiles to deviate from the linear fits near the interface. Therefore, the temperatures of Material 1 and Material 2 adjacent to the interface are taken to be the values of the linear projections of Material 1 and Material 2 profiles projected to the interface and are defined as T_L and T_H , respectively. The temperature drop ΔT across the interface is determined by $T_H - T_L$ and the interfacial temperature T_{int} is the mean of T_H and T_L .

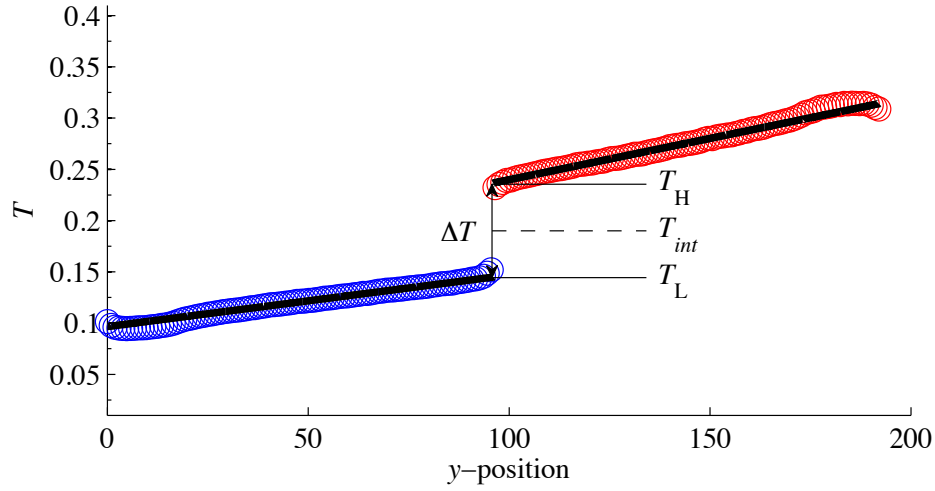


Figure 5.1: A representative steady-state temperature profile obtained in the reference simulation. The temperature profiles for Material 1 and Material 2 are shown in blue and red circles, respectively. The black curves are independent linear fits that are used to define the temperatures of Material 1 and Material 2 adjacent to the interface, T_L and T_H respectively. The fit excludes the data points that correspond to the heat bath regions and the first five segments adjacent to either the heat bath regions or the interface. The interfacial temperature, T_{int} , is determined by the mean of T_L and T_H and the temperature drop across the interface, ΔT , is determined by $T_H - T_L$.

Once ΔT is found, the interfacial conductance, G , can be calculated from the expression $G = Q_{HB}/\Delta T$. One of the most important requirements of the NEMD method is to ensure that the system has reached the steady state. During the simulation, both temperature gradients and the temperature drop evolve from zero to final steady-state values. Measuring the temperature drop before the steady state is established will result in an over-prediction of the interfacial conductance. To ensure the system has reached the steady state, a moving average of conductance over a fixed temporal window is monitored. Temperature profiles and the resultant temperature drop are averaged over the moving temporal window throughout the simulation and a moving temporal average of the interfacial conductance is obtained. The evolution of the conductance averaged over the moving temporal window is used to determine when the steady-state temperature drop is established in the system. All data for times after the steady state was reached are averaged in the calculation of the final value of conductance.

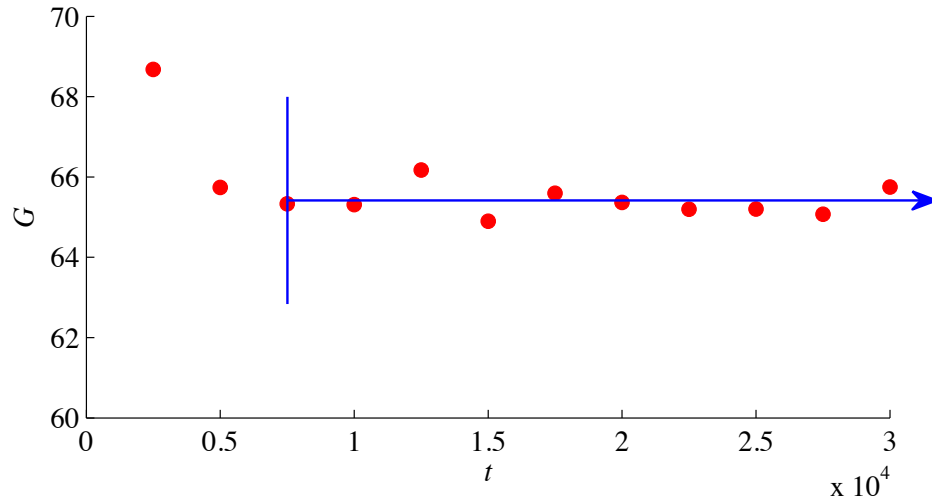


Figure 5.2: The time evolution of interfacial conductance, G , calculated from the temperature profiles and temperature drop, ΔT , averaged over a moving temporal window in a simulation of heat flow through the reference sample. The steady state is deemed to be reached by the time of $t = 7500$ (marked by the vertical line). The final value of G is determined by averaging all data obtained after achievement of the steady state indicated by the horizontal arrow.

The temporal conductance plot calculated for the reference simulation is shown in Fig. 5.2. In all simulations, data was recorded every timestep and averaged over a 500 000 timestep ($t = 2500$) temporal window. By the time of $t = 7500$ the temporal decay of conductance ceases and the temporal variation of the conductance values can be attributed to statistical fluctuations about an average value. The final conductance value is obtained by averaging over the steady-state part of the simulation as schematically shown by the horizontal arrow in Fig. 5.2.

By this method, the data obtained in the steady state are divided into 10 estimations of the value of conductance predicted by the NEMD simulation. The final value of the conductance reported is the mean of the 10 estimations. An estimate of the standard error of the mean is determined from the sample set of 10 estimations and is provided as a measure of the precision in estimating the mean conductance predicted by the NEMD simulations [145]. For the reference simulation with $Q_{HB} = 6$ and temporal evolution of G shown in Fig. 5.2, this method produces a final predicted conductance value of $G = 65.4 \pm 0.1$.

5.3 Computational Results

The results of a systematic evaluation of the sensitivity of the values of interfacial conductance, G , to variations in ΔT , T_{int} , the density of interatomic interfacial interactions, and strength of interaction potential are reported in this section. First, the effects of variations in ΔT and T_{int} are evaluated to serve as a reference for comparison of other simulation results, in Section 5.3.1. Predicted values of conductance are found to increase with increasing T_{int} and be independent of ΔT . In Section 5.3.2, results from a series of simulations are reported which show conductance to decrease as the density of interatomic interfacial interactions increases. Next, the sensitivity of the conductance to the strength of the local interatomic interactions adjacent to the interface is investigated and compared to the effect of the density of interatomic interactions in Section 5.3.3. Analysis of the vibrational spectra is reported for a better understanding of the observed effects in Section 5.3.4.

5.3.1 Effect of Temperature

Two series of simulations were performed to examine the sensitivity of interfacial conductance, G , to the interfacial temperature, T_{int} , and temperature drop, ΔT . In the first series of simulations, the implemented heat flow rate, Q_{HB} , was varied to produce different resultant temperature drops, ΔT , in the steady state. In addition to the reference simulation where $Q_{HB} = 6$, the simulation procedure was repeated with $Q_{HB} = 3$ and $Q_{HB} = 1$, which resulted in different values of ΔT across the interface. The results of this series of simulations are plotted as a function ΔT in Fig 5.3.

The value of ΔT shown in Fig 5.3 is the mean of the 10 values of interfacial temperature drop corresponding to the 10 calculations of G in the steady state for each simulation. The error bars represent the estimation of the standard error of the mean calculated by the method described above. The greater estimate of the standard error of the mean for smaller ΔT is expected as there will be greater variation in conductance calculations when ΔT is

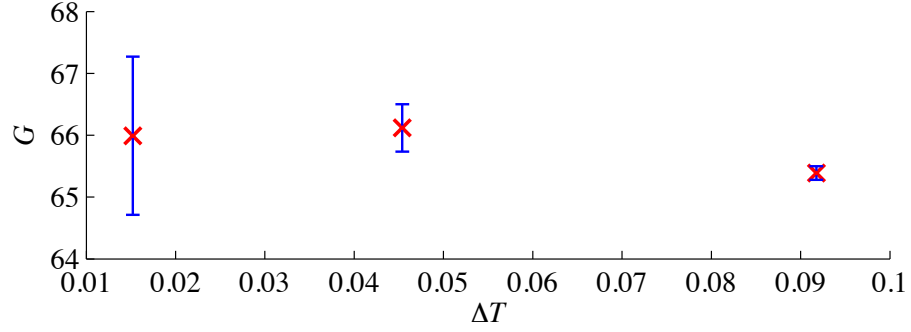


Figure 5.3: Values of interfacial thermal conductance, G , between two 2D LJ materials plotted as a function of the temperature drop across the interface, ΔT , resulting from variations in the implemented heat flow rate, Q_{HB} . The values of G are determined by the mean of 10 sample calculations taken in the steady state and the ranges of the error bars are determined from the estimate of the standard error of the mean. No statistically significant variation in G values is observed, suggesting G is independent of Q_{HB} over the range studied.

smaller relative to the statistical fluctuations in the temperature profiles. The reference simulation where $Q_{HB} = 6$ yields the lowest estimate of the standard error of the mean and a predicted conductance of $G = 65.4 \pm 0.1$. No statistically significant variation in G values is observed with variation in ΔT . Different values of ΔT were obtained for different simulations by varying the applied heat flow rate, Q_{HB} . Therefore, the results of this series of simulations demonstrate that the values of G are independent of Q_{HB} over the range studied.

In the second series of simulations, the initial distribution of velocities is altered to produce a different average system temperature, T_{sys} , for each simulation. In addition to the reference simulation where $T_{sys} = 0.2$, the simulation procedure was repeated with $T_{sys} = 0.3$ and $T_{sys} = 0.15$. Variation in the values of T_{sys} results in variation in the values of T_{int} , which are taken as mean of the 10 values of interfacial temperatures corresponding to the 10 calculations of G in the steady state for each simulation. The results of this series of simulations plotted as a function T_{int} are shown in Fig 5.4. The estimates of the standard error of the mean are less than 1 for each simulation and are not represented in the figure for simplicity.

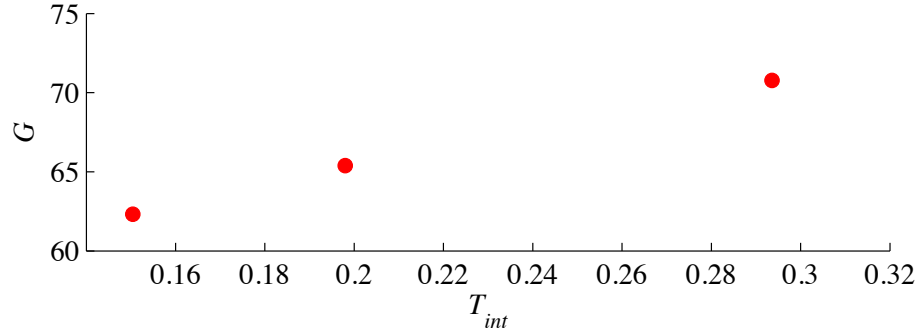


Figure 5.4: Values of interfacial thermal conductance, G , between two 2D LJ materials plotted as a function of the interfacial temperature, T_{int} . The values of G are observed to increase with increasing T_{int} . This result is expected due to the contribution of inelastic phonon scattering processes to interfacial thermal transport, which increases with temperature [9].

The results show an increase in conductance with increasing interfacial temperature. This result is expected due to the contribution of inelastic phonon scattering processes to interfacial thermal transport [9]. These processes depend directly on the occupancy of the phonon vibrational states, which increases with temperature. Therefore, this dependence should be considered when comparing results from simulations of different interfacial temperature.

5.3.2 Effect of Density of Interatomic Interfacial Interactions

In this sub-section, the details and results of a series of simulations performed to investigate the sensitivity of the conductance to the density of interatomic interfacial interactions (i.e., interatomic interactions between materials across the interface) are presented. The motivation for this series of simulations comes from the results presented in Section 4.2.4 which suggest the thermal conductance per interatomic inter-tube interaction is sensitive to the local density of interatomic inter-tube interactions. To further investigate this result, a series of simulations is designed to study the effect of the density of interatomic interfacial interactions between LJ materials on the thermal conductance across the LJ material interface.

As discussed above, a simple LJ “toy” model is employed to allow variation in the density of interatomic interfacial interactions while minimizing variation in the structural characteristics of the interface. This is achieved by unique adaptations to the reference computational setup described in Section 5.2. The initial lattice sites are identical to the reference setup. Type 1 atoms are placed on lattice sites in rows 1-100 (4050 atoms) to form Material 1 and Type 2 atoms are placed on lattice sites in rows 101-199 (4010 atoms) to form Material 2. An additional set of 4010 atoms of Type 3 are also placed on the same lattice sites in rows 101-199 to form Material 3. Interactions between Type 1 and Type 3 atoms are identical to interactions between Type 1 and Type 2 atoms, such that $\sigma_{12} = \sigma_{13} = 1$ and $\epsilon_{12} = \epsilon_{13} = 1$. Just as in the reference setup, interactions between atoms of the same type are equal with $\sigma_{xx} = 1$ and $\epsilon_{xx} = 4$, and the mass of all atom types are equal (i.e., $m_1 = m_2 = m_3 = 1$). However, interactions between Type 2 and Type 3 atoms are not considered (i.e., $\sigma_{23} = 0$ and $\epsilon_{23} = 0$). In this way, a computational setup is designed where Type 1 atoms are interfacing with Type 2 and Type 3 atoms which share the same initial atomic coordinates, atomic mass, interatomic potential for self-interactions, and interatomic potential for interactions with Type 1 atoms, but do not interact with each other.

This setup can be considered as two separate interfaces with identical physical characteristics; the interface between Material 1 and Material 2 (i.e., Interface 1-2) and the interface between Material 1 and Material 3 (i.e., Interface 1-3). The interfaces in this setup also share the same physical characteristics as the interface in the reference setup, with the exception that Type 1 atoms adjacent to the interface have exactly twice as many interatomic interfacial interactions in the 2-interface setup as compared to the reference setup. Therefore, the 2-interface setup produces two interfaces with the same physical characteristics as the interface of the reference setup while having twice the density of interatomic interfacial interactions in Material 1.

The density of interatomic interfacial interactions can be increased further with the

introduction of additional materials. Analogous to the setup described above, additional setups are constructed with 4, 7, 11, and 15 LJ materials which produce 3, 6, 10, and 14 interfaces, respectively. In all computational setups, the additional LJ materials share the same initial atomic coordinates, atomic mass, interatomic potential for self-interactions, and interatomic potential for interactions with Type 1 atoms, which are all identical to the atomic coordinates, atomic mass, and interatomic potentials described for Material 2 and Material 3 above. In addition, there are no interatomic interactions considered between materials where both atom types are greater than 1 (i.e., $\sigma_{xy} = 0$ and $\epsilon_{xy} = 0$ where $x, y > 1$).

The computational procedure is similar to the one described in Section 5.2 with the following exceptions. Energy is removed from the 770 Type 1 atoms in rows 1-19 at a rate of Q_{HB} which varies between simulations. Energy is added to the 770 atoms of each type in rows 181-199 of each material at a rate of Q_{HB}/I where I is the number of interfaces in the system. Velocity scaling is performed individually for each material to ensure the heat flow rate into each material in the hot heat bath region is Q_{HB}/I . In this way, the heat flow rate across each of the I interfaces is Q_{HB}/I . Energy must be removed from Material 1 at a rate of Q_{HB} to equal the rate of heat flow being imparted by I interfaces. Q_{HB} is adjusted between simulations to minimize variation in the values of both the rate of energy removal, Q_{HB} , and the rate of energy addition, Q_{HB}/I , across all simulations. A sample of the LAMMPS input script for the simulation of the system described above, where $I = 2$, is provided in Appendix A to detail the general setup and computational procedure used in this series of simulations.

Temperature profiles are generated for each individual material. When $I = 1$, energy is removed from Material 1 and added to Material 2 at the same rate which causes the values of the average temperatures of Material 1 and Material 2 to fall and rise by about the same amount, respectively. This results in a steady-state value of interfacial temperature, T_{int} , that is roughly equal to the value of the initial average system temperature. However, for the cases where $I > 1$, energy is removed from Material 1 at a greater rate than the

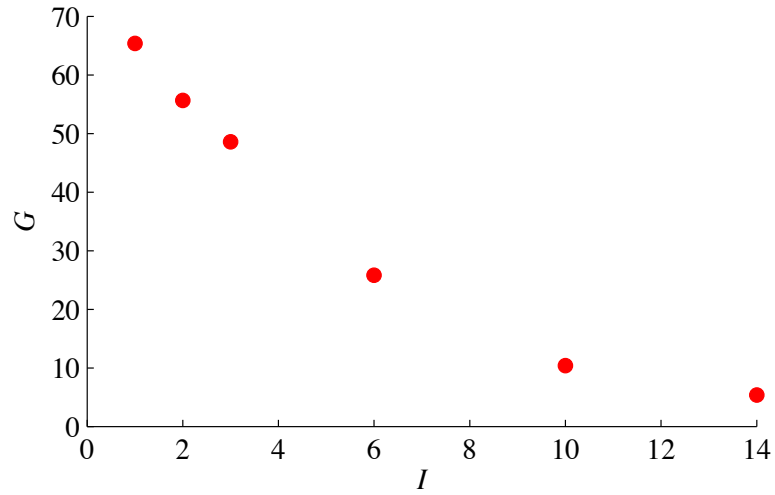


Figure 5.5: Values of interfacial thermal conductance across Interface 1-2, G , plotted as a function of the total number of interfaces in the system, I . The unique computational setup is designed such that Material 1 forms multiple interfaces with multiple identical materials which do not interact with each other. Thus, an increase in the value I corresponds to an increase in the number of interatomic interfacial interactions experienced by Material 1, but does not affect the interfacial area or the number of interatomic interfacial interactions contributing to interfacial conductance for Interface 1-2. The results suggest conductance per interatomic interfacial interaction decreases with increasing density of interatomic interfacial interactions.

individual rates at which energy is added to all other materials, causing the value of the average temperature of Material 1 to fall by more than the rise in values of the average temperatures of the other materials. This causes the steady-state value of T_{int} for each interface to be lower than the value of the initial average system temperature. However, as shown in Section 5.3.1, G is sensitive to T_{int} . Therefore, the values of the initial average system temperature, defined by the initial distribution of atomic velocities, are adjusted to ensure steady-state values of T_{int} range between 0.16 and 0.21 across all simulations. Although some variation in values of T_{int} exist between simulations, the degree of variation is not considered significant enough to affect final results, as is discussed below.

The values of G are determined for Interface 1-2 in all simulations by the same temporal averaging procedure described in Section 5.2 and the expression $G = Q_{HB}/I\Delta T$, where Q_{HB}/I and ΔT are the heat flow rate and temperature drop for Interface 1-2, respectively.

For the sake of comparison across simulations, calculations of G are restricted to Interface 1-2, since all interfaces in a given simulation are considered identical and averaging over all interfaces would lead to variations in the precision of the estimate of G between simulations. As a reference, calculations of G were performed for all interfaces in the simulation where $I = 14$. The variation in final values of G for all interfaces in this simulation was found to be less than 1.4% of the minimum predicted value, which is much less than the variation in values of G for different simulations. Therefore, restricting the comparison of values of G across simulations to only those values obtained for Interface 1-2 in each simulation is validated.

The final values of G across Interface 1-2 are plotted with respect the number of interfaces in each simulation, I , in Fig. 5.5. The estimates of the standard error of the mean are less than 0.4 for every simulation and are omitted from the plot for simplicity. Recall that some variation in values of T_{int} exist between simulations, as mentioned in Section 5.3.1. The mean value of T_{int} for Interface 1-2 was obtained for each simulation by averaging over the time during which values of G were calculated. The mean values of T_{int} were determined to be 0.19, 0.21, 0.21, 0.21, 0.18, and 0.16 for the cases where $I = 1, 2, 3, 6, 10$, and 14, respectively. As illustrated in Fig. 5.4, the final values of G increase with increasing values of T_{int} . Thus, the values of T_{int} should be considered when comparing values of G across simulations. The value of T_{int} for the reference simulation ($I = 1$) is less than the values of T_{int} for the cases where $I = 2, 3$ and 6. Therefore, a decrease in the values of G for these simulations is in contradiction to the dependence of G on T_{int} . Moreover, while a reduction in G with decreasing values of T_{int} , as compared to the values of G and T_{int} for the reference simulation, can be expected for the cases where $I = 10$ and $I = 14$, the magnitude of the reduction cannot be explained solely by the magnitude of the dependence of G on T_{int} observed in Fig. 5.4. Therefore, the nature of the results observed in Fig. 5.5 cannot be explained by variations in the values of T_{int} .

The values of G decrease with increasing I and the effect is strongest for lower values

of I . This suggests the interfacial conductance between Material 1 and Material 2 decreases as Material 1 experiences more interatomic interfacial interactions. Recall that the results of Section 4.2.4 suggest that the conductance per interatomic inter-tube interaction, G/N , decreases with increasing average number of interatomic inter-tube interactions per atom in the contact region, M . Although the results of this sub-section are presented in terms of total conductance, the number of interatomic interfacial interactions attributed to Interface 1-2 (i.e., interactions between Type 1 and Type 2 atoms), which is analogous to N , is the same for all simulations. Thus, G is directly related to the conductance per interatomic interfacial interaction across Interface 1-2. Moreover, while the number of interatomic interfacial interactions across Interface 1-2 remains constant, the average number of interatomic interfacial interactions per atom for Type 1 atoms adjacent to the interface, which is analogous to M , is directly related to I . The combination of these factors implies the results are analogous to the results reported in Section 4.2.4; the conductance per interatomic interfacial interaction across Interface 1-2 decreases as the average number of interatomic interfacial interactions per Type 1 atom adjacent to the interface increases.

5.3.3 Effect of Interaction Energy

The computational setup described in the previous sub-section was designed to minimize all other variations between simulations except for the density of interatomic interfacial interactions experienced by Type 1 atoms adjacent to the interface. However, since the interatomic potential between Type 1 atoms and all other atom types is the same for all simulations, the magnitude of the total interfacial interaction energy increases with the density of interatomic interfacial interactions for Type 1 atoms. Therefore, an alternative explanation for the results observed in Section 5.3.2 could be that the conductance per interfacial interaction decreases as the magnitude of the interaction energy experienced by Type 1 atoms adjacent to the interface increases. Note that the unique computational setup allows the interaction energy experienced by Type 1 atoms adjacent to the interface to be

increased without increasing the number or strength of interatomic interactions between Type 1 and Type 2 atoms, which would increase interfacial conductance [146–149].

A second computational setup is designed to investigate the dependence of conductance on interaction energy without altering the number or strength of interatomic interactions between Type 1 and Type 2 atoms. The initial setup is identical to the reference setup described in Section 5.2 with the exception that the single row of Type 1 atoms adjacent to the interface are replaced with Type 3 atoms. Note that the definition of Type 3 atoms described here differs from the definition given in the previous sub-section. Here, interactions between Type 2 and Type 3 atoms are identical to interactions between Type 1 and Type 2 atoms such that $\sigma_{12} = \sigma_{23} = 1$ and $\epsilon_{12} = \epsilon_{23} = 1$. Just as in the reference setup, interactions between atoms of the same type are equal with $\sigma_{xx} = 1$ and $\epsilon_{xx} = 4$, and the mass of all atom types are equal (i.e., $m_1 = m_2 = m_3 = 1$). However, interactions between Type 1 and Type 3 atoms are defined by $\sigma_{13} = 1$ and $\epsilon_{13} = 6$. This single row of Type 3 atoms can be considered as a special case of interfacial Type 1 atoms where interactions between these interfacial atoms and Type 2 atoms are the same as they are in previous simulations, but interactions between these interfacial atoms and all other non-interfacial Type 1 atoms are stronger than they are in previous simulations. In this way, the magnitude of the total interaction energy experienced by these special case Type 1 atoms adjacent to the interface is increased without increasing the number or strength of interatomic interactions between Type 1 and Type 2 atoms as compared to the reference simulation.

The remainder of the computational procedure is identical to the one used in the reference simulation. For the remainder of the discussion on this special case simulation, Type 3 atoms are considered as special case interfacial Type 1 atoms, and thus are treated as Type 1 atoms for the purpose of determining ΔT . The final predicted value of $G = 55.0 \pm 0.1$ is observed to be lower than the value of $G = 65.4 \pm 0.1$ obtained from the reference simulation. The values of G can be expected to change with variations in the interaction energy experienced by atoms adjacent to the interface, as these variations can affect the

local occupied vibrational density of states (DOS) in the interfacial monolayers [147]. The interaction energy experienced by the special case interfacial Type 1 atoms in the simulation described in this sub-section is identical to the interaction energy experienced by the interfacial Type 1 atoms interacting with three different interfaces (i.e., $I = 3$) in the simulations described in the previous sub-section. However, the value of G obtained from the simulation where $I = 3$ is only $G = 48.6 \pm 0.4$. Therefore, the reduction in the values of G cannot be explained by variation in interaction energy alone. This suggests that increasing the average number of interatomic interactions per atom adjacent to the interface has an additional effect that is not realized simply by increasing the magnitude of the interaction energy per atom.

Although the special interfacial Type 1 atoms described in this sub-section and the interfacial Type 1 atoms in the case where $I = 3$ experience the same total interaction energy, the nature of the interactions are expected to be different. For example, while the special interfacial Type 1 atoms interact with just one material across a single interface, the interfacial Type 1 atoms in the case where $I = 3$ interact with three different atom types across three different interfaces. As the three different atom types do not directly interact with each other, their trajectories will be far less coherent than the trajectories of one single atom type. Therefore, the additional reduction in the values of G may arise from a coherence effect which increases with the number of interatomic interactions per atom.

5.3.4 Analysis of Vibrational Spectrum

To further investigate the nature of the effects which cause variations in the values of G , the spectral density of occupied vibrational states is estimated by Welch's method of estimation of a power spectrum [150] for both the row of Type 1 atoms and the row of Type 2 atoms adjacent to the interface. Simulations of the single interface system, 3-interface system, 6-interface system, and the special case system described in the previous sub-section are continued for an additional 3.24×10^5 timesteps ($t = 1620$) after the initial

6×10^6 timesteps over which the investigation of G was performed for all simulations. Instantaneous velocities are recored every 10 timesteps for all Type 1 and Type 2 atoms adjacent to the interface.

The local vibrational power spectral density (PSD) for both rows is obtained by performing Welch's estimation from each atom's recorded velocities and averaging over all atoms in each row. Summation of the PSD over a range of frequencies provides the amount of vibrational power contained in the range of frequencies. In this way, the PSD can be considered as a classical analogy to the occupied vibrational DOS, where the PSD is a measure of the vibrational power contained in a range of frequencies, rather than the number of quantized vibrational states occupied. Thus, the PSD is directly related to the energy of all phonons occupying available vibrational states over a range of phonon frequencies. Each measurement of the PSD is normalized with respect to the total vibrational power such that the summation of the normalized PSD over all frequencies is equal to 1. The normalized PSD is a measure of the relative contribution to total vibrational power as a function of phonon frequency and allows for direct comparison between rows of atoms possessing different amounts of total vibrational power.

Results of the normalized PSD calculations for the interfacial atoms in the single interface, 3-interface, 6-interface, and special case systems are shown in Fig. 5.6. In all plots, the normalized PSD for Type 1 and Type 2 atoms adjacent to Interface 1-2 are represented by blue and red curves, respectively, and vibrational frequencies are given in inverse LJ time units. The area of overlap between the two normalized PSD calculations in each plot is defined by the summation of the minimum of the two PSD curves over all frequencies, and is visually represented by the gray shaded areas. The calculated overlap area provides a measure of the similarity between the local occupied DOS of Type 1 atoms adjacent to the interface and the local occupied DOS of Type 2 atoms adjacent to the interface, which is directly related to the conductance across the interface [88, 147, 151]. Since the area under all normalized PSD curves is equal to 1, an overlap area of 1 indicates perfect similarity

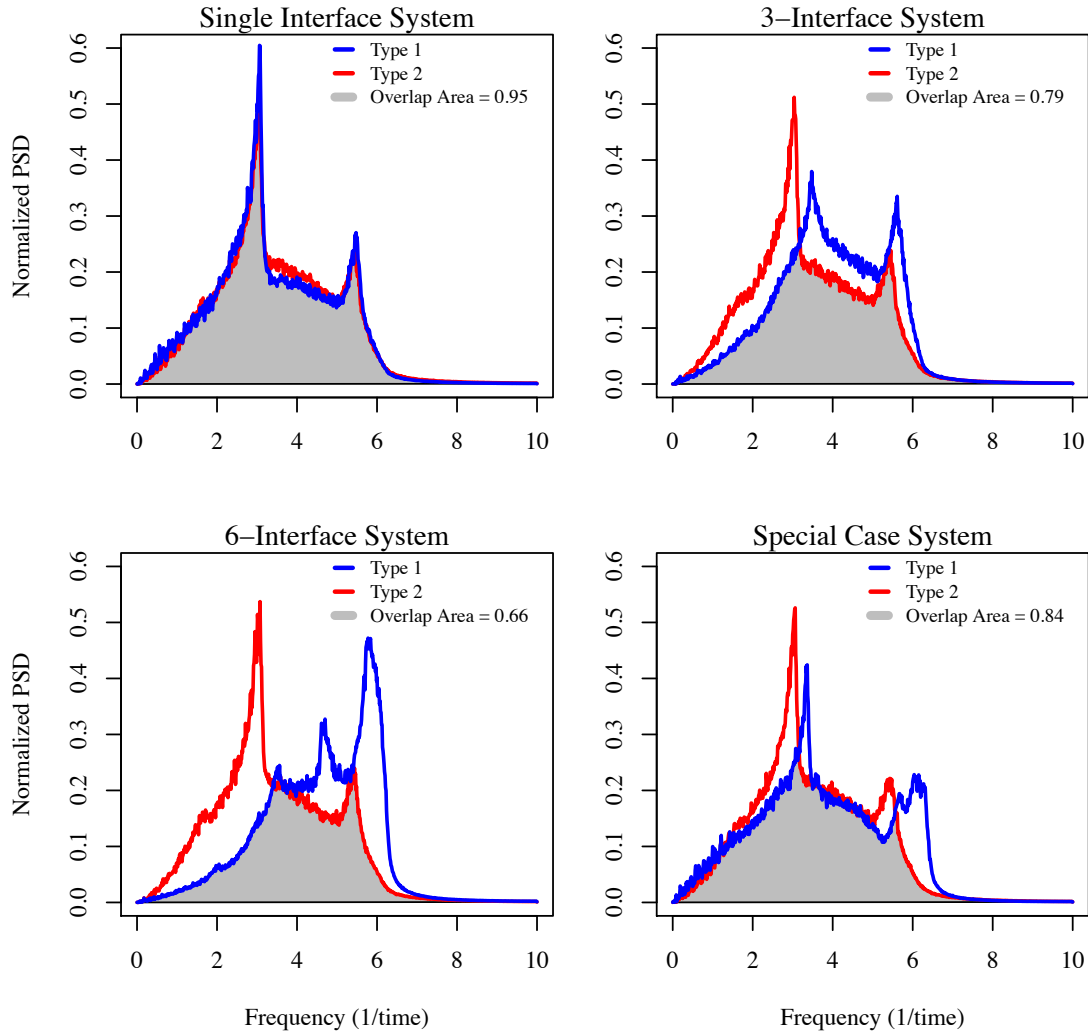


Figure 5.6: Calculations of the normalized PSD for the Type 1 and Type 2 atoms adjacent to Interface 1-2 are represented by blue and red curves, respectively, for the single interface, 3-interface, 6-interface, and special case systems. The area of overlap between the two normalized PSD curves, the value of which is provided in the legend and is visually represented by the gray shaded area in each plot, is a measure of the similarity between the normalized PSD curves. The normalized PSD for Type 1 atoms is shifted to higher frequencies for increasing number of interfaces, which indicates less similarity between the local occupied DOS of the two atom types adjacent to the interface, and corresponds to a decrease in the value of G . The interaction energy experienced by Type 1 atoms adjacent to the interface is equal in both the 3-interface and special case systems. However, the value of the area of overlap in the 3-interface system is less than the value of the area of overlap in the special case system, suggesting an additional effect caused by the incoherent trajectories of the atoms adjacent to each of the multiple interfaces in the 3-interface system.

between the local occupied DOS for the two rows of atoms adjacent to the interface, and smaller values of overlap area indicate less similarity between the two local occupied DOS.

The results presented in Fig. 5.6 indicate the normalized PSD for Type 2 atoms adjacent to the interface is similar for all systems, while the normalized PSD for Type 1 atoms adjacent to the interface varies between simulations. Focusing on the single interface, 3-interface, and 6-interface systems, variation in the normalized PSD for Type 1 atoms illustrates a shift in the power distribution, with a higher fraction of the total power being distributed among higher frequency phonons with increasing number of interfaces. This results in less similarity between the two local occupied DOS, as indicated by a reduction in the area of overlap between the two PSD curves with increasing number of interfaces. Less similarity between the local occupied DOS of Type 1 atoms and Type 2 atoms adjacent to the interface means there are less direct channels of conductance for phonons adjacent to the interface, which leads to a reduction in interfacial conductance.

An increase in the interaction energy experienced by atoms adjacent to the interface is expected to shift the distribution of local occupied DOS towards higher frequency phonons [147]. However, recall that the results of Section 5.3.3 suggest the reduction in values of G cannot be explained by variations in interaction energy alone. This notion is further supported by comparison of the plots of the normalized PSD for the 3-interface system and the special case system described in Section 5.3.3. Recall that Type 1 atoms adjacent to the interface in both systems experience the same total interaction energy. The normalized PSD for Type 1 atoms in both plots show a shift in energy distribution to higher frequency phonons resulting in lower overlap area as compared to the reference single interface system. Two prominent peaks in the normalized PSD for Type 1 atoms are observed, with one peak occurring in a relatively low frequency range and the other peak occurring in a higher frequency range, for both systems. It is interesting to note that while the higher frequency peak appears to have been shifted to higher frequencies in the special case system than in the 3-interface system, the 3-interface system has a lower value overlap area. This implies

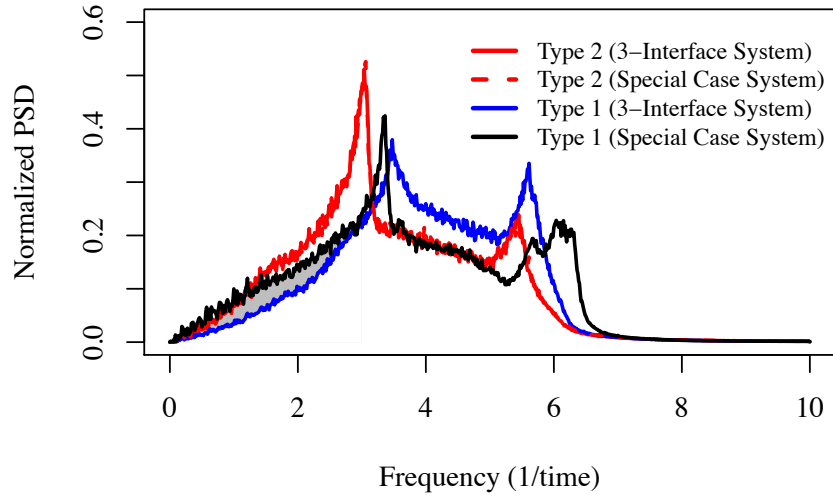


Figure 5.7: Calculations of the normalized PSD for the Type 1 and Type 2 atoms adjacent to Interface 1-2 are plotted for the 3-interface and special case systems. The normalized PSD for Type 1 atoms in the 3-interface and special case systems are represented by blue and black curves, respectively. The normalized PSD for Type 2 atoms in the 3-interface and special case systems are represented by solid red and dashed red curves, respectively, and show very little variation between systems. These two curves are intentionally chosen to have the same color to demonstrate the nearly indistinguishable difference between them. The value of overlap area for frequencies below Frequency = 3 is greater in the special case system than in the 3-interface system, and the difference between the two values is visually represented by the gray shaded area. Variation between the normalized PSD for Type 1 atoms in the 3-interface and special case systems suggest the presence an additional effect caused by the incoherent trajectories of the atoms adjacent to each of the multiple interfaces in the 3-interface system.

that the shape of the normalized PSD for Type 1 atoms varies between the two simulations.

To further investigate the variation between the vibrational spectra, the normalized PSD for Type 1 and Type 2 atoms for both the 3-interface and the special case systems are re-plotted on the same axes and shown in Fig. 5.7. The normalized PSD for Type 1 atoms adjacent to the interface in the 3-interface and special case systems are represented by blue and black curves, respectively. The normalized PSD for Type 2 atoms adjacent to the interface in the 3-interface and special case systems are represented by solid red and dashed red curves, respectively. Note that the normalized PSD for Type 2 atoms in both systems are nearly identical and the colors of the curves representing them are intentionally chosen to be the same to allow for a simpler representation. The normalized PSD for Type 1 atoms demonstrate two prominent peaks in both systems. However, while the higher frequency peak is shifted less for the 3-interface system than for the special case system, as compared to the single interface system, the distribution of the normalized PSD changes such that the value of the overlap area in the 3-interface system is lower than the value of the overlap area in the special case system.

In addition to the value of the total overlap area being less for the 3-interface system, the value of the overlap area for frequencies below Frequency = 3 is also less for the 3-interface system. This difference in overlap area is visually represented by the gray shaded area and is a measure of the difference between the values of overlap area for frequencies below Frequency = 3 in each system. As discussed in Section 4.1.1, low frequency phonons transmit across the interface of two materials more readily than higher frequency phonons when the interatomic interactions across the interface are weak as compared to interatomic interactions within the two materials, which is the case for all simulations discussed in this chapter and for all simulations designed to investigate the conductance across CNT-CNT junctions discussed in this dissertation. Therefore, just as in the case of CNT-CNT conductance, lower frequency phonons contribute more to the conductance between Material 1 and Material 2 than higher frequency phonons. This means that differences in the values of

the overlap area at lower frequencies affect the values of conductance more than differences in the values of the overlap area at higher frequencies. Variation in the normalized PSD of the Type 1 atoms in the two systems is such that values of both the total overlap area and the overlap area occurring at lower frequencies is less in the 3-interface system than in the special case system. The combination of these factors contributes to the lower value of G in the 3-interface system. This variation in the normalized PSD of Type 1 atoms between the two systems cannot be explained by a difference in interaction energy and provides further evidence of a coherence effect arising from the introduction of multiple interfaces.

5.4 Summary

NEMD simulations were performed to investigate the thermal conductance across an interface between 2D LJ materials. The motivation for this investigation was to examine the effects of the density of interatomic interactions between Material 1 and Material 2 while minimizing the variation of other parameters such as structural geometry and contact area. A unique computational setup was designed to allow Material 1 to interact with multiple identical materials which did not directly interact with each other, across multiple interfaces. Determination of G was limited to the conductance across the interface between Material 1 and Material 2. Increasing the number of interfaces, I , leads to an increase in the number of interatomic interfacial interactions experienced by Type 1 atoms adjacent to the interface, while keeping the interfacial area and the number of interatomic interactions between Material 1 and Material 2 constant.

Results presented in Section 5.3.2 show a reduction in the values of total conductance across Interface 1-2, G , with increasing number of interfaces, I . Due to the unique computational setup, these results are directly analogous to results discussed in detail in Section 4.2.4, which suggest a reduction in the conductance per interatomic inter-tube interaction, G/N , with increasing average number of interatomic inter-tube interactions per atom in the

contact region, M . An additional computational setup was designed to investigate the effect of the total interaction energy experienced by Type 1 atoms adjacent to the interface on the values of G . Simulations were performed for a special case system containing a single interface with the interactions between Type 1 atoms adjacent to the interface and all other Type 1 atoms modified such that the interaction energy experienced by Type 1 atoms adjacent to the interface in the special case system was equal to the interaction energy experienced by Type 1 atoms adjacent to the interface in the 3-interface system. Results presented in Section 5.3.3 demonstrate the value of G for the special case system is greater than the value of G for the 3-interface system, even though Type 1 atoms adjacent to the interface experience the same interaction energy in both systems. These results suggest the difference in the values of G for different values of I cannot be explained by variation in interaction energy alone and that additional effects may arise due to the incoherent trajectories of the atoms adjacent to each of the multiple interfaces.

The normalized PSD, which is related to the occupied DOS, was calculated for Type 1 and Type 2 atoms adjacent to the interface for several systems. Results presented in Section 5.3.4 demonstrate a shifting of the distribution of occupied vibrational states of Type 1 atoms to higher frequencies with increasing I . This shifting leads to less similarity between the normalized PSD for Type 1 and Type 2 atoms adjacent to the interface and causes a reduction in the values of G . The normalized PSD of the Type 1 atoms in the 3-interface and special case systems were compared and found to vary in such a way that the values of both the total overlap area and the overlap area occurring at lower frequencies is less in the 3-interface system than in the special case system. This variation in the normalized PSD of Type 1 atoms between the two systems cannot be explained by a difference in interaction energy and provides further evidence of a coherence effect arising from the introduction of multiple interfaces.

The summation of these results has significant implications for the development of the general model for CNT-CNT conductance. Conductance across the interface between two

2D LJ materials is observed to depend on the number of interatomic interfacial interactions experienced by Material 1. This dependence cannot be accounted for by interatomic interaction energy alone. Systems having the same values of interatomic interaction energy experienced by atoms adjacent to the interface and the same number of interatomic interfacial interactions across Interface 1-2, but different values of G , are distinguished by variations in the total number of interatomic interfacial interactions experienced by Type 1 atoms adjacent to the interface. Therefore, any general model of CNT-CNT conductance based on the conductance per interatomic inter-tube interaction, G/N , should depend on the average number of interatomic inter-tube interactions per atom in the contact region, M .

Chapter 6

General Description of CNT-CNT Conductance

6.1 Background

Thermal conductance between partially overlapping parallel CNTs has been shown to be linearly proportional to the length of the overlap, which is directly related to the overlap area, when the CNTs and CNT-CNT overlaps are longer than several tens of nanometers in Section 4.2.3. However, this linear dependence of conductance on the overlap area is found to break down for overlap lengths less than 10 nm [5, 6], as discussed in Section 4.1.3, and for non-parallel configurations with small contact areas in Section 4.2.4. A decrease in the conductance per interatomic inter-tube interaction, G/N , with increasing average number of interatomic inter-tube interactions per atom in the contact region, M , is observed in Section 4.2.4 as well. This observation is further supported by results discussed in Section 5.3, which show a decrease in conductance per interface and increasing mismatch between the vibrational spectra of atoms adjacent to the interface as the number of interatomic interactions of the atoms adjacent to the interface increases.

The summation of these results suggests that any predictive model of conductance at CNT-CNT contacts of arbitrary configuration should be dependent on the area of the contact region, which can be quantified by the number of interatomic inter-tube interactions, and the density of interatomic inter-tube interactions in the contact region, which can be

characterized by the average number of interatomic inter-tube interactions per atom in the contact region. In this chapter, the development of a general description of CNT-CNT conductance is described. In the next section, the formulation of the predictive model is discussed. The functional form of the model is based on the observed qualitative trends discussed above, and the model is fit to quantitatively match the results of MD simulations reported in Section 4.2.4. In Section 6.3, the predictive model is shown to accurately predict conductance at CNT-CNT contacts with configurations that differ from the contacts for which the model was fit and span a wider range of contact area and geometric structure. The model is summarized in the context of qualitative trends observed from the results of the MD simulations reported in this work and in the literature, and the quantitative limitations of the model are discussed in Section 6.4.

6.2 Predictive Model

A general predictive model of the conductance at CNT-CNT contacts is developed for contacts of arbitrary configuration based on the results of the MD simulations discussed in Chapters 4 and 5. Determining the contact area between two adjacent, cylindrical CNTs is non-trivial and the value may be relative to different definitions of the contact region. Therefore, the predictive model is designed to be dependent on the number of interatomic interactions between CNTs, which is a more objective description of the contact area.

The total number of interatomic interactions between CNTs in an MD simulation can be determined geometrically by the total number of inter-tube atomic pairs (i.e., pairs with one atom belonging to each CNT) separated by less than the cutoff distance of the Lennard-Jones (LJ) potential, which is $r_c = 1$ nm for all simulations of conductance between CNTs reported in this work. However, since the interaction energy of the LJ potential approaches zero near the cutoff distance, the magnitude of the interaction energy between atoms decreases as their separation distance approaches the cutoff distance. Thermal conductance

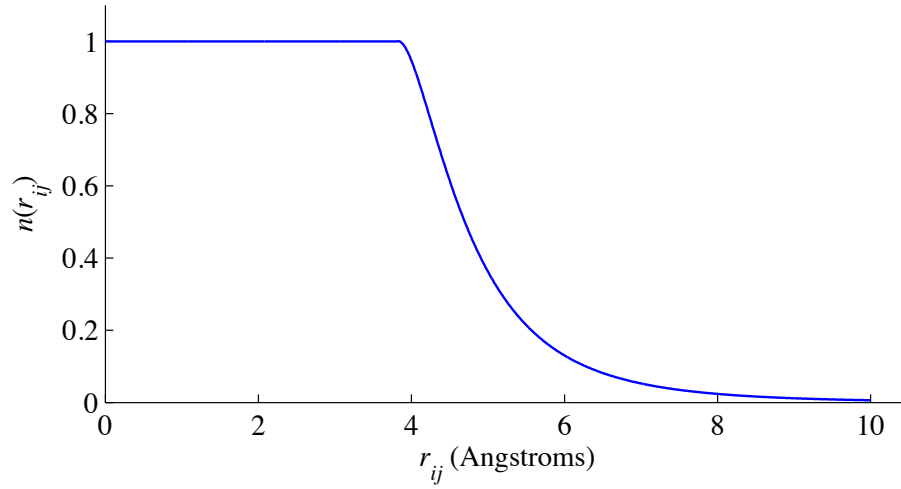


Figure 6.1: The scaling factor, n , which is described by Eq. 6.1 and scales the contribution of each inter-tube atomic pair to the total “effective” number of interatomic inter-tube interactions, N_{eff} , based on the separation distance between each atomic pair, r_{ij} . All inter-tube atomic pairs with r_{ij} less than the equilibrium separation distance of the LJ potential, r_m , are counted as one interaction, with r_{ij} greater than the LJ cutoff distance, r_c , are not counted, and with $r_m \leq r_{ij} \leq r_c$ are scaled by the absolute value of the LJ potential for the given r_{ij} , and normalized such that $|U_{ij}^{LJ}(r_m)| = 1$.

across a material interface increases as the magnitude of the bonding energy of interatomic interactions across the interface increases [146–149]. Therefore, interatomic interactions with lower magnitudes of energy and separation distances near the cutoff distance are likely to contribute less to the total inter-tube conductance than interactions with greater magnitudes of energy and separation distances closer to the equilibrium separation distance. Thus, when characterizing the contact region in terms of the total number of interatomic inter-tube interactions, it is reasonable to count the atomic pairs separated by distances close to the cutoff distance less than the atomic pairs separated by distances close to the equilibrium separation distance. In other words, each atomic pair can be scaled by its separation distance when counting the total number of interatomic inter-tube interactions.

One way to scale the counting of each interatomic inter-tube interaction is by the interatomic potential describing the interactions themselves. The 12-6 form of the LJ potential is defined by Eq. 2.2 and is used to described all interatomic inter-tube interactions in all

simulations discussed in this work. The equilibrium separation distance for LJ interactions, r_m , is the distance at which the LJ potential is equal to the potential minimum, $-\epsilon$, such that $U_{ij}^{LJ}(r_m) = -\epsilon$, and is determined by $r_m = 2^{1/6}\sigma$. For the purposes of counting the total number of interatomic inter-tube interactions, inter-tube atomic pairs with separation distances of $r_{ij} < r_m$ are counted as 1 interaction, inter-tube atomic pairs with $r_{ij} > r_c$ are not counted as an interaction, and inter-tube atomic pairs with $r_m \leq r_{ij} \leq r_c$ are scaled by the absolute value of $U_{ij}^{LJ}(r_{ij})$ divided by ϵ , where division by ϵ normalizes the scaling factor to ensure it equals 1 when evaluated at $r_{ij} = r_m$. Thus the scaling factor for each inter-tube atomic pair is defined as

$$n(r_{ij}) = \begin{cases} 1 & r_{ij} < r_m \\ \frac{1}{\epsilon} \left| 4\epsilon \left[\left(\frac{\sigma}{r_{ij}} \right)^{12} - \left(\frac{\sigma}{r_{ij}} \right)^6 \right] \right| & r_m \leq r_{ij} \leq r_c \\ 0 & r_{ij} > r_c \end{cases} \quad (6.1)$$

The scaling factor, n , is plotted as a function of r_{ij} in Fig. 6.1. The value of the curve for $r_m \leq r_{ij} \leq r_c$ takes the same form as the absolute value of the LJ potential, normalized such that $|U_{ij}^{LJ}(r_m)| = 1$. In this way, the scaling of each interatomic inter-tube interaction with a separation distance in this range is directly related to its interatomic interaction energy. The total “effective” number of interatomic inter-tube interactions, N_{eff} , is defined by the summation of $n(r_{ij})$ over all inter-tube atomic pairs, or equivalently by

$$N_{eff} = \sum_i \sum_j n(r_{ij}), \quad (6.2)$$

where index i is varied over the indices of all atoms in one CNT and index j is varied over the indices of all atoms in the neighboring CNT. The value of N_{eff} provides a quantitative description of the contact region and accounts for variations in geometric structure by consideration of the separation distance between each interatomic inter-tube interaction. Analogous to the definition of M provided in Section 4.2.4, M_{eff} is taken as the average

number of “effective” interatomic inter-tube interactions per atom in the contact region. The value of M_{eff} can be determined by the average of all non-zero values of n , i.e.,

$$M_{eff} = \frac{N_{eff}}{\sum_k (1 - \delta(n_k))}, \quad (6.3)$$

where index k is varied over the indices of all n values and δ is the Dirac delta distribution defined as

$$\delta(x) = \begin{cases} 1 & x = 0 \\ 0 & x \neq 0 \end{cases} \quad (6.4)$$

Recall that the results presented in Section 4.2.4 show that the conductance per interatomic inter-tube interaction, G/N , varies for different values of M . Therefore, it may be possible to describe the total conductance across a CNT-CNT junction as a function of N_{eff} and M_{eff} such that $G(N_{eff}, M_{eff}) = g(M_{eff}) \cdot N_{eff}$ where $g(M_{eff})$ describes the dependence of G/N_{eff} on M_{eff} . For each simulation discussed in Section 4.2.4, instantaneous values of N_{eff} and M_{eff} were calculated at each timestep for which an instantaneous value of G was recorded in the steady state. The final values of N_{eff} and M_{eff} are taken as the mean of each corresponding sample set of 10 calculations. The final values of G are divided by their corresponding values of N_{eff} and plotted with respect to M_{eff} for each system in Fig. 6.2. The error bars represent the division of the standard deviation of the instantaneous values of G by the final value of N_{eff} .

The function $g(M_{eff})$ is derived empirically to fit the data and is plotted as a blue curve in Fig. 6.2 along with the calculations of G/N_{eff} represented as red circles. The functional form of $g(M_{eff})$ is determined purely by empirical fitting and is taken as

$$g(M_{eff}) = (AM_{eff}^B + C), \quad (6.5)$$

where $A = -1.62 \times 10^{-11}$, $B = 10.86$, and $C = 0.2154$ are empirical fitting parameters. The

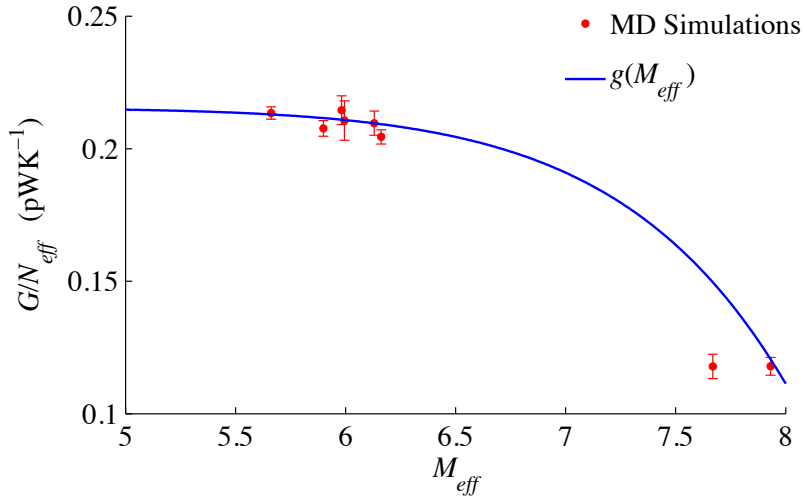


Figure 6.2: The conductance per total “effective” number of interatomic inter-tube interactions, G/N_{eff} , plotted as a function of the average number of “effective” interatomic inter-tube interactions per atom in the contact region, M_{eff} . Values of G/N_{eff} are calculated from the results of MD simulations and represented by red circles. The error bars represent the division of the standard deviation of the instantaneous values of G by the final mean value of N_{eff} , for each simulation. The blue curve represents the function $g(M_{eff})$, which is defined by Eq. 6.5, empirically fit to the results of the MD simulations, and incorporated into the final predictive model, $G(N_{eff}, M_{eff})$, given by Eq. 6.6.

calculated value of G/N_{eff} from the MD simulations which is predicted by $g(M_{eff})$ with the least amount of accuracy at $M_{eff} \sim 7.67$ corresponds to the simulation configuration with an initial orientation angle between CNTs of $\theta = 20^\circ$ which is described in detail in Section 4.2.4. The CNTs of this simulation demonstrate a greater degree of bending in the steady-state configuration, shown in Fig. 4.12, than the CNTs of any other simulation. It is possible that the CNTs in this simulation experienced a greater degree of strain than the CNTs in all other simulations, due to the greater degree of bending, and that this additional strain has an affect on the final value of G . Therefore, for the purposes of determination of $g(M_{eff})$, the value of G/N_{eff} calculated from the initial $\theta = 20^\circ$ configuration simulation is not considered in the empirical fitting procedure. Possible inconsistencies with the results of this configuration simulation and the results of simulations of other configurations are discussed further in the next section.

With $g(M_{eff})$ defined, a general predictive model of the conductance at CNT-CNT

contacts can be expressed in terms of N_{eff} and M_{eff} by

$$G(N_{eff}, M_{eff}) = (AM_{eff}^B + C)N_{eff}, \quad (6.6)$$

where N_{eff} and M_{eff} are determined directly from the atomic coordinates of any arbitrary configuration. In the next section, the accuracy of this predictive model is discussed through comparison of predictions of CNT-CNT conductance obtained from this model and predictions obtained from MD simulations of CNT-CNT contacts with varied geometric configurations.

6.3 Comparison with Computational Results

Several additional series of simulations are performed in order to compare results of the predictive model given in Eq. 6.6 to results of additional MD simulations of other configurations. In the first additional series, non-equilibrium MD (NEMD) simulations are performed to predict the thermal conductance at the interface between two partially overlapping parallel CNTs. The general geometric arrangement of the CNTs is identical to the geometric arrangement of the CNTs in the simulations described in Section 4.2.3. However, the LAMMPS implementation of the AIREBO potential [111] was used to describe the interatomic interactions in the simulations described in Section 4.2.3. Due to variation in the predicted CNT thermal properties among simulations employing different interatomic potentials, which is discussed in Section 3.2.3.3, quantitative agreement may not be expected between values of G obtained from simulations employing the AIREBO potential and simulations employing a combination of the Tersoff and LJ potential as was implemented in the simulations described in Section 4.2.4. Therefore, simulations are performed for configurations of the same partially overlapping parallel CNT arrangement described in Section 4.2.3 while having the same description of interatomic potential described in Section 4.2.4.

The computational procedure is nearly identical to the general computational procedure described in Section 4.2.4, with the following exceptions. Just as in the simulations described in Section 4.2.3, periodic boundary conditions are applied in the direction parallel to the aligned axes of both CNTs. The distance between the periodic boundaries of the computational cell is adjusted during the sample preparation routine to achieve pressure of 1 atm in the periodic direction before implementation of the constant flux. In addition, no restoring spring force is applied, as the CNTs are already completely aligned. The remainder of the computational procedure follows the general procedure described in Section 4.2.4. The configurations simulated in this first series were for CNTs with CNT length $L_T = 100$ nm and overlap lengths of $\Delta x_{12} = 10, 20, 30$ and 40 nm, and for CNTs with CNT length $L_T = 200$ nm and overlap length $\Delta x_{12} = 40$ nm. One additional simulation was performed with $L_T = 100$ nm and $\Delta x_{12} = 10$ nm but with free boundary conditions in all directions. This simulation contains only one contact in the computational cell and can be considered as a special case of the simulations described in Section 4.2.4 where the initial $\theta = 0^\circ$ and the CNTs are translated in the direction parallel to their longitudinal axes so that they only overlap by 10 nm. A spring force is applied in this simulation in the same manner as described in Section 4.2.4 with $K_{Spr} = 0.01$ eV \AA^{-2} .

In the second additional series of simulations, the same computational procedure that was implemented for simulations described in Section 4.2.4 was repeated for CNTs of length $L_T = 200$ nm and initial $\theta = 0^\circ$ and 45° . The procedure described in Section 4.2.4 for obtaining instantaneous values of G and the procedure described in the previous section for obtaining instantaneous values of N_{eff} and M_{eff} were performed for the steady state of all simulations to produce a sample set of 10 calculations for each variable in each simulation. The mean of the instantaneous values of G is taken as the final MD prediction of G for each simulation, and the standard deviation of each sample set is taken as a measure of precision in the MD prediction. The sample sets of 10 calculations of N_{eff} and M_{eff} are used to calculate 10 values of G by the general predictive model given in Eq. 6.6 for each

configuration. The mean of these 10 values of G is taken as the final prediction of G by the predictive model for each configuration, and the standard deviation of each sample set is taken as a measure of precision in the model prediction.

The values of G obtained by the MD method, represented by red circles, and by the predictive model, represented by blue and black crosses, are plotted with respect to N_{eff} in Fig. 6.3. The value of N_{eff} shown in this figure is taken as the mean value of all instantaneous calculations of N_{eff} for each configuration, for the purposes of plotting. The results of the MD simulations are obtained by the computational procedures previously described, whereby values of G are determined from values of ΔT_{12} obtained during the steady state of constant flux simulations. The results of the predictive model are calculated by Eq. 6.6, where calculations of N_{eff} and M_{eff} are based on the atomic coordinates obtained during the steady state of the corresponding constant flux simulations. Blue crosses represent the results of the predictive model for configurations similar to the ones described in Section 4.2.3 with values of $\Delta x_{12} = 10, 20, 30$ and 40 nm and values of L_T equal to 100 nm and 200 nm. Black crosses represent the results of the predictive model for configurations similar to the ones described in Section 4.2.4 with initial values of θ ranging from 0° to 90° and values of L_T equal to 100 nm and 200 nm. In addition, the special case configuration of two parallel 100 nm CNTs with overlap length $\Delta x_{12} = 10$ nm and free boundary conditions in all directions is also represented by a black cross. Error bars represent one sample standard deviation of the sample set of calculations of G by the MD method and the predictive model, and are provided as a measure of precision.

The results of the predictive model are found to be in good agreement with the results of the MD simulations for all simulations except one. The configuration for which the results of both methods are the least consistent with each other is of the two 100 nm CNTs forming a single junction with initial $\theta = 20^\circ$. As discussed in the previous section, the CNTs of this configuration simulation demonstrate a greater degree of bending in the steady state than the CNTs of any other simulation. The initially low value of $\theta = 20^\circ$ causes a greater

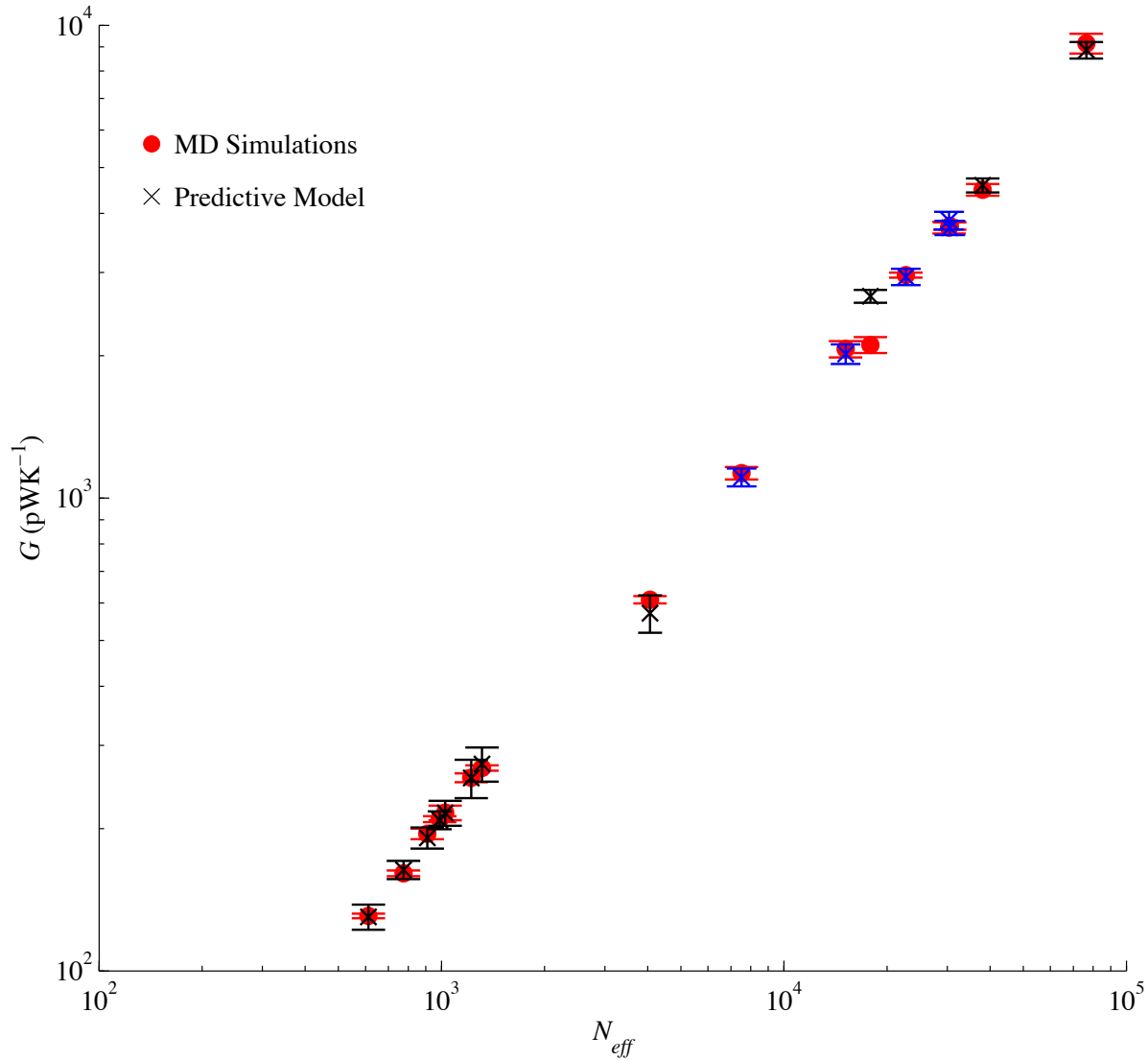


Figure 6.3: The values of conductance, G , obtained by the MD method, represented by red circles, and by the predictive model, represented by blue and black crosses, plotted with respect to the total “effective” number of interatomic inter-tube interactions, N_{eff} . Error bars represent one sample standard deviation of the sample set of calculations of G by the MD method and the predictive model. Blue crosses represent the results of the predictive model for configurations of partially overlapping parallel CNTs, and black crosses represent the results of the predictive model for configurations similar to the ones described in Section 4.2.4 and a special case configuration of two parallel 100 nm CNTs with overlap length $\Delta x_{12} = 10$ nm and free boundary conditions in all directions. The results of predictive model and the MD method show the least amount of agreement for the case of two CNTs forming a junction with initial $\theta = 20^\circ$. Inconsistencies with the results of this configuration simulation and the results of the other simulations are discussed in detail in the text. The results of the predictive model show good agreement with the MD results for all other configurations.

magnitude of interaction energy between the CNTs than any other non-parallel configuration and a stronger spring force is required to prevent complete alignment. As the CNTs bend and deform to seek a low-energy configuration, the ends of each CNT become displaced from their original positions, causing the magnitude of the spring force to increase. These factors likely cause stress in the axial and/or radial directions of the CNTs which can affect their thermal properties. Xu and Buehler [78] performed NEMD simulations on CNTs under varying degrees of axial strain. Their results suggest a decrease in thermal conductivity and phonon group velocity with increasing magnitudes of positive and negative strain. Zhu et al. [152] investigated the thermal conductivity of CNTs under radial strain by the non-equilibrium Green's functions method. Their results show a decrease in thermal conductivity with increasing degree of radial deformation. These results imply the vibrational spectrum of a CNT is affected by axial and radial stress. Furthermore, the increased magnitude of the spring force in the initial $\theta = 20^\circ$ simulation can be expected to restrict the low frequency, long wavelength vibrational modes in the CNTs. As discussed in Section 4.1.1, low frequency vibrational modes are considered to significantly contribute to CNT-CNT conductance. The summation of these factors suggests the CNT-CNT conductance in this configuration may be affected by significantly stronger spring forces exerted on the CNT ends.

6.4 Summary

A general predictive model of the conductance at CNT-CNT contacts is developed for contacts of arbitrary configuration based on the results of previous MD simulations. The total number of interatomic interactions between CNTs is chosen as an objective description of the contact area, and can be calculated directly from the atomic coordinates obtained from MD simulations. The contribution of each interatomic inter-tube interaction to the total number of interatomic inter-tube interactions is scaled based on the separation distance

of the atomic pair, r_{ij} , and Eq. 6.1. The summation of all contributions, N_{eff} , is taken as the “effective” number of total interatomic inter-tube interactions and provides a more descriptive characterization on the contact region. Based on the results presented in Sections 4.2.4 and 5.3, the average number of “effective” interatomic inter-tube interactions per atom in the contact region, M_{eff} , is also considered.

Values of N_{eff} and M_{eff} are calculated from the atomic coordinates obtained from all MD simulations described in Section 4.2.4 and additional simulations described in the previous section. An empirical model is derived which predicts values of G from values of N_{eff} and M_{eff} . The predictive model has the functional form given in Eq. 6.6 and parameters which are empirically fit based on the results of MD simulations. Comparison of the values of G obtained from the MD method and the values obtained from the predictive model is shown in Fig. 6.3. The results of the predictive model are found to be in good agreement with the results of the MD simulations for all simulations except for the simulation of two 100 nm CNTs forming a single junction with initial $\theta = 20^\circ$. As previously discussed, the CNTs of this configuration simulation demonstrated a greater degree of bending in the steady state than the CNTs of any other simulation. Therefore, the results of this simulation may be influenced by higher levels of stress experienced by each CNT.

The agreement between the results of the predictive model and the results of the MD method over the wide range of simulation configurations is non-trivial. Recall that the conductance per interatomic inter-tube interaction, G/N , was found to decrease with increasing number of interatomic inter-tube interactions, N , in Section 4.2.4. This trend is consistent with the results of Zhong and Lukes [5] and Xu and Buehler [6] discussed in Section 4.1.3, which show that the conductance per overlap length between partially overlapping parallel CNTs, σ_T , decreases with increasing overlap length, Δx_{12} , for overlap lengths less than 10 nm. However, σ_T is observed to be constant with increasing Δx_{12} for overlap lengths greater than several tens of nanometers in the results presented in Section 4.2.3. Accurately reproducing this complex dependence required the introduction of an additional variable,

M_{eff} . Results presented in Sections 4.2.4 and 5.3.2 suggest the conductance per interatomic inter-tube interaction is sensitive to the value of M_{eff} , which is a quantitative description of the average density of interatomic inter-tube interactions in the contact region. Incorporation of M_{eff} into the predictive model allows for accurate description of the conductance at CNT-CNT contacts over a range of contact areas and orientations, despite a complex relationship between conductance per area and the structure of the contact region. Furthermore, consideration of M_{eff} can likely explain the unique results of Zhong and Lukes [5] and Xu and Buehler [6] since small contact regions tend to have higher values of M_{eff} , as seen in Section 4.2.4.

Although the predictive model is presented as a generalized description of conductance at CNT-CNT contacts, the values of A , B , and C of Eq. 6.6 are parameterized based on the results of MD simulations which share common parameters. Therefore, it is likely that quantitative agreement between the predictive model and the results of MD simulations will be restricted to simulations with those same parameters. For example, the van der Waals interactions responsible for CNT-CNT conductance are described by the LJ potential with LJ energy parameter $\epsilon = 3.0$ meV. An increase in ϵ would correspond to an increase in the bonding strength between CNTs and lead to an increased prediction of G [149, 153]. Therefore, the current parameterization of the predictive model is not expected to accurately predict the results of MD simulations implementing different values of LJ parameters. In addition, the predicted values of G are shown to increase with CNT length for CNT lengths less than 100 nm in Section 4.2.1. Thus, the current parameterization of the predictive model is likely to over-predict values of G for configurations of CNTs with lengths less than 100 nm. Finally, Evans et al. [7] performed MD simulations of conductance across CNT-CNT cross-junctions with pressure applied to the contact region in the direction perpendicular to the axes of the CNTs. Their results show an increase in conductance with increasing magnitude of applied pressure. The authors attribute this relationship to both the increased contact area resulting from CNT deformation and an increase

in the van der Waals bonding stiffness due to shorter separation distances of the interatomic interactions. While variations in contact area and interatomic separation distances are accounted for in the predictive model, the results obtained for the junction between two 100 nm CNTs with initial $\theta = 20^\circ$ suggest the current parameterization of the predictive model is less accurate for systems under significant amounts of pressure or stress. The summation of these factors implies the need for modified parameterizations of the predictive model when considering systems with varied descriptions of van der Waals interactions between CNTs, CNTs with lengths less than 100 nm, or CNTs under pressure or stress.

Chapter 7

Summary, Relevance, and Future Direction

7.1 Summary of Major Results

Carbon nanotubes (CNTs) have gained a significant amount of research interest for use in thermal management applications due to the exceptionally high values of the intrinsic CNT thermal conductivity, k , reported in experiments [10–17] and computational studies [1–4, 18–34]. However, the collective thermal conductivity through CNT structures or CNT-based material is found to be orders of magnitude lower than the values of measurements of individual CNT thermal conductivity [8, 35–41]. This work describes the results of molecular dynamics (MD) simulations designed to investigate the two major factors that may be responsible for the low conductivity of the CNT structures: the reduction of the intrinsic conductivity of the individual CNTs due to the inter-tube interactions, and the low thermal conductance at CNT-CNT contacts that may be sensitive to the geometry of the contact and the local contact density.

In spite of the ability of MD simulations to fully control the simulated environment, the values of thermal conductivity, k , predicted in different MD simulations exhibit surprisingly large divergence even when the simulated system is nominally the same. Therefore, it is important to understand the reasons for the data variability across the published studies, which is due to contributions from both the true variation of the intrinsic CNT conductivity

due to the variation of the length of the CNTs used in the simulations, and the variation of k due to variability of computational procedures and interatomic potentials employed in the different simulations. Thus, the major results of this work are categorized into two distinct areas: investigations of the factors which affect intrinsic and MD predictions of CNT conductivity, and investigations of the factors which affect CNT-CNT conductance.

An MD investigation of k of individual CNTs discussed in Section 3.2.2 reveals a sensitivity of k to CNT length which is found to transition from a strong length dependence for CNTs shorter than ~ 200 nm to a much weaker dependence for longer CNTs. Results of an MD study of k of CNTs formed into aligned bundles discussed in Section 3.2.4 show that contrary to a number of earlier reports, the van der Waals inter-tube coupling between CNTs does not result in any statistically significant changes in the intrinsic conductivity of the CNTs. This finding directly addresses Objective 2 presented in the introduction of this work.

In Section 3.2.3, results of non-equilibrium molecular dynamics (NEMD) simulations with uni-directional heat flux implementation reveal the effect of increasing the length of the central part of the nanotube, L_C , is nearly indistinguishable from the effect of increasing the length of the heat bath regions, L_B . This observation suggests that the common practice of neglecting the length of the heat bath regions when defining the CNT length in NEMD simulations may introduce a substantial variability in the predicted values of thermal conductivity. The results of this study suggest that the total length of a CNT (*including* the length of the heat bath regions) should be used as the definition of the CNT length in NEMD simulations with uni-directional heat flux, and the length of the heat bath regions should be short relative to the overall CNT length. The length dependence of k in bi-directional flux implementations is also shown to be best represented by the definition of the effective CNT length comprised of the length of the heat bath regions and the length of an unperturbed part of the CNT between the hot and cold heat bath regions. This convention yields values of k that are consistent between the two (uni- and bi-directional)

implementations of the heat flux in NEMD simulations. The summation of these findings directly addresses Objective 1 presented in the introduction.

Objective 3 is directly addressed throughout Chapter 4. In Section 4.2.1, results of a series of simulations designed to investigate the effects of CNT length on CNT-CNT conductance demonstrate a stronger length dependence acting over a longer range of CNT lengths than has been previously reported. The conductance across a CNT-CNT junction is shown to be unaffected by the presence of neighboring junctions when separated further than the range of direct van der Waals interactions in a series of simulations discussed in Section 4.2.2. When junctions are separated by the equilibrium separation distance of the two neighboring tubes, conductance per junction is reduced by only $\sim 10\%$. This is in contrast to a previous study that claimed an approximately one order of magnitude reduction [8].

Results of a series of simulations presented in Section 4.2.3 demonstrate that the conductance between partially overlapping parallel CNTs increases monotonically with increasing overlap length when the CNTs and CNT-CNT overlaps are longer than several tens of nanometers. In contrast to this finding, the results of a series of simulations presented in Section 4.2.4 demonstrate a non-linear dependence of conductance on the number of inter-tube interactions between CNTs. The conductance per inter-tube interaction is shown to be dependent on the local density of interatomic inter-tube interactions, which is quantified by the average number of inter-tube interactions per atom in the contact region. This observation is further supported by the results of a series of LJ “toy model” simulations presented in Section 5.3 which demonstrates that the conductance between two 2D LJ materials decreases as the number of interatomic interactions of atoms in one material adjacent to the interface increases. These results cannot be explained by variation in the interaction energy alone, and analysis of the vibrational spectra of the atoms adjacent to the interface suggests an additional coherence effect which depends on the average number of interatomic interactions per atom, rather than the interaction energy.

The summation of the results presented in Sections 4.2.4 and 5.3 suggests that any predictive model of conductance at CNT-CNT contacts of arbitrary configuration should be dependent on the area of the contact region, which can be quantified by the number of interatomic inter-tube interactions, and the density of interatomic inter-tube interactions in the contact region, which can be characterized by the average number of interatomic inter-tube interactions per atom in the contact region. The observed sensitivity of conductance to the average number of interatomic inter-tube interactions per atom in the contact region is a novel finding. This observation is also supported by the results of LJ “toy model” simulations, suggesting the nature of this dependence may not be limited to the interfacial conductance between CNTs.

Objective 4 is satisfied in Chapter 4 with the formulation of an empirical predictive model of conductance at CNT-CNT contacts for an arbitrary configuration of CNTs. The model is quantitatively fit to the results presented in Section 4.2.4 and shown to have good agreement with additional MD predictions of the conductance at CNT-CNT contacts of various configurations. Limitations of the predictive model are discussed and modified parameterizations are recommended when considering systems with different descriptions of van der Waals interactions between CNTs, CNTs with lengths less than 100 nm, or CNTs under pressure or stress.

7.2 Relevance to Application Areas

The major results presented in this work have implications for both thermal applications of CNT-based materials and investigation of CNT conductivity by the NEMD method. The results of the systematic evaluation of the effect of the size and location of the heat bath regions, and definition of the CNT length on the predictions of NEMD simulations clarify the origins of the quantitative discrepancies across published data and provide recommendations on the choice of computational parameters that may reduce some of the inconsis-

tendencies between the computational results. The recommendations that the definition of the CNT length should include the length of the heat bath regions in NEMD simulations with uni-directional heat flux, and that the length of the heat bath regions should be short relative to the overall CNT length, have implications not only for reducing the variability in MD results, but for the mechanisms of ballistic thermal transport in NEMD simulations of other systems as well.

The results of investigations of the intrinsic k of CNTs have implications for increasing the overall thermal transport in aligned CNT bundles. Due to the absence of any reduction in k from van der Waals inter-tube interactions, the overall thermal transport can be increased by increasing the direct number of CNT channels in the bundle. Furthermore, the intrinsic k of each individual CNT will have a strong length dependence for CNTs shorter than ~ 200 nm. The results of investigations of CNT-CNT conductance provide guidance for optimizing the thermal performance of CNT-based materials. Overall CNT-CNT conductance can be improved by increasing CNT length, and density and area of CNT-CNT contacts.

7.3 Future Directions

While significant conclusions have been formulated as a result of this work, there are several topics of interest that could be addressed in further detail:

- *Investigation of the Effects of the Size and Location of Heat Bath Regions in General NEMD Simulations:* Variations in the definition of sample length in NEMD simulations are not unique to investigations of CNTs. Therefore, the observed effects of the size and location of heat bath regions may cause discrepancies in the results of MD studies of the thermal conductivity of other materials when the sample length is comparable to the length of ballistic transport. The parametric study outlined in Section 3.2.3 can be extended to NEMD simulations of other materials to determine

if the recommendations should be generalized for all systems.

- *Experimental Validation of the Effect of the Local Density of Interatomic Interactions Adjacent to the Interface:* The sensitivity of interfacial conductance to the local density of interatomic interactions adjacent to the interface is a significant finding. Results presented in Chapter 5 suggest this dependence may not be restricted to CNT-CNT conductance. This effect should result in greater conductance per area in the periphery of a contact region as compared to the conductance per area in the isotropic center of a contact region. Experimental methods such as the time domain thermoreflectance (TDTR) method may be able to resolve differences in the conductance per area for different areas of an interface. Determination of a higher conductance per area at the periphery of the interface would support the observed finding. In addition, a decrease in conductance per area with increasing contact area may be experimentally resolved for interfaces with small contact areas, which would also support the finding. However, in all series of simulations for which the effect of the local density of interatomic interactions adjacent to the interface was observed, the interactions across the interface were much weaker than the interactions within the same material. Therefore, this effect may not be present in systems with chemical bonding between materials adjacent to the interface.
- *Extension of the Predictive Model to Additional Systems:* The basic formulation of the predictive model is based on the results of MD simulations of CNT-CNT conductance. However, the results of Chapter 5 suggest the sensitivity of conductance to the local density of interatomic interactions adjacent to the interface may be present in other systems. Therefore, it may be possible to parameterize the predictive model to predict the interfacial conductance between additional materials. The basic procedure described in Chapter 6 can be applied to MD simulation results of other systems. Agreement between the results of the predictive model and MD results of more gen-

eralized interfacial systems would support the finding of the effect of the local density of interatomic interactions adjacent to the interface.

Publications and Presentations

Publications

In Preparation

- Salaway, R. N., Zhigilei, L. V. “A generalized formulation of thermal conductance between carbon nanotubes and the effect of local structure”. *In Preparation*.

In Print

- Salaway, R. N., Zhigilei, L. V. “Molecular dynamics simulations of thermal conductivity of carbon nanotubes: Resolving the effects of computational parameters”. *International Journal of Heat and Mass Transfer*, **70**, 954-964, (2014).
- Volkov, A. N., Salaway, R. N., Zhigilei, L. V. “Atomistic simulations, mesoscopic modeling, and theoretical analysis of thermal conductivity of bundles composed of carbon nanotubes”. *Journal of Applied Physics*, **114**, 104301 (2013). A figure from this paper is used for cover art for the journal issue.
- Baker, C. H., Wu, C., Salaway, R. N., Zhigilei, L. V., Norris, P. M., “Resolving the vibrational and electronic contributions to thermal conductivity of silicon near the solid-liquid transition: molecular dynamics study”. *International Journal of Transport Phenomena*, **13**, 143-150 (2013).
- Baker, C. H., Wu, C., Salaway, R. N., Zhigilei, L. V., Norris, P. M., “Vibrational contribution to thermal conductivity of silicon near solid-liquid transition”. *In Proceedings of the IMECE2011*, 64064 (2011).

- Hopkins, P. E., Duda, J. C., Salaway, R. N., Smoyer, J. L., Norris, P. M. “Effects of intra- and interband transitions on electron-phonon coupling and electron heat capacity after short-pulsed laser heating”. *Nanoscale and Microscale Thermophysical Engineering*, **12**, 320-333 (2008).
- Salaway, R. N., Hopkins, P. E., Norris, P. M., Stevens, R. J. “Phonon contribution to thermal boundary conductance at metal interfaces using embedded atom method simulations”. *International Journal of Thermophysics*, **29**, 1987-1996 (2008).
- Hopkins, P. E., Salaway, R. N., Stevens, R. J., Norris, P. M. “Temperature dependent thermal boundary conductance at Al/Al₂O₃ and Pt/Al₂O₃ interfaces”. *International Journal of Thermophysics*, **28**, 947-957 (2007).

Presentations

- Volkov, A. N., Wittmaack, B. K., Salaway, R. N., Zhigilei, L. V., “Effect of conductivity of individual nanotubes and structural parameters of nanotube networks on the heat transfer in carbon nanotube films and vertically aligned arrays”. *2013 Material Research Society Spring Meeting and Exhibit*, San Francisco, CA, USA. April 2013
- Salaway, R. N., Volkov, A. N., Zhigilei, L. V., “The effects of local structure on thermal transport in carbon nanotube materials”. *2013 Material Research Society Spring Meeting and Exhibit*, San Francisco, CA, USA, oral presentation. April 2013.
- Salaway, R. N., Volkov, A. N., Zhigilei, L. V., “Molecular dynamics simulations of thermal transport in carbon nanotube structures: Effect of computational procedures and parameters”. *2013 Material Research Society Spring Meeting and Exhibit*, San Francisco, CA, USA, poster presentation. April 2013.
- Salaway, R. N., Volkov, A. N., and Zhigilei, L. V., “Thermal conductance at carbon nanotube junctions and the effect of local structure”. *2012 ASME International*

Mechanical Engineering Congress and Exposition, Houston, TX, USA, poster presentation. November 2012.

- Salaway, R. N., Volkov, A. N., and Zhigilei, L. V., “Thermal conductance at carbon nanotube junctions and the effect of local structure”. *2012 ASME International Mechanical Engineering Congress and Exposition*, Houston, TX, USA, oral presentation. November 2012.
- Zhigilei, L. V., Volkov, A. N., Salaway, R. N., Wittmaack, B. K., “Mesoscopic modeling of carbon nanotube materials: Computational model and applications to structural, thermal and mechanical properties”. *64th Southeastern Regional Meeting of the American Chemical Society (SERMACS 2012)*, Raleigh, NC, USA. November 2012 (invited).
- Salaway, R. N., Volkov, A. N., and Zhigilei, L. V., “Thermal conductance at CNT-CNT contacts: Influence of contact density and local structure”. *2012 ASME Summer Heat Transfer Conference*, Rio Grande, Puerto Rico, oral presentation. July 2012.
- Zhigilei, L. V., Volkov, A. N., Salaway, R. N., Jacobs, W. M., Nicholson, D. A., Zemer, H., “Computational study of thermal transport in carbon nanotube materials”. *NSF 2012 CBET Grantee Conference*, Baltimore, MD, USA. June 2012.
- Salaway, R. N., Volkov, A. N., and Zhigilei, L. V., “Thermal properties of carbon nanotubes and the effects of interacting neighbors”. *2012 Pan-American Advanced Studies Institute*, Santiago, Chile, oral presentation. January 2012. **NSF Travel Grant awarded.**
- Salaway, R. N., Volkov, A. N., and Zhigilei, L. V., “Thermal conductivity and interfacial conductance of carbon nanotubes: The effect of inter-nanotube interactions”. *2011 ASME International Mechanical Engineering Congress and Exposition*, Denver, CO, USA, poster presentation. November 2011. **NSF Student Travel Grant**

awarded.

- Salaway, R. N., Volkov, A. N., and Zhigilei, L. V., “Thermal properties of carbon nanotubes and the effects of interacting neighbors: Atomistic molecular dynamics simulations”. *2011 ASME International Mechanical Engineering Congress and Exposition*, Denver, CO, USA, oral presentation. November 2011.
- Zhigilei, L. V., Volkov, A. N., Salaway, R., Nicholson, D., Jacobs, W., “Thermal conductivity of carbon nanotube materials: Atomic-level simulations, mesoscopic modeling and scaling laws”. *AFOSR Thermal Sciences Grantees’ Meeting*, Arlington, VA, USA. September 2011.
- Salaway, R., Volkov, A. N., Zhigilei, L. V., “Thermal conductivity of carbon nanotubes: The effect of inter-nanotube interactions”. *AFOSR Thermal Sciences Grantees’ Meeting*, Arlington, VA, USA, poster presentation. September 2011.
- Zhigilei, L. V., Volkov, A. N., Jacobs, W., Nicholson, D., Salaway, R., “Multiscale computational study of carbon nanotube materials”. *2011 Joint Annual conference of the National Society of Black Physicists and National Society of Hispanic Physicists*, Austin, TX, USA. September 2011.
- Volkov, A. N., Salaway, R., Nicholson, D., Jacobs, W., Zhigilei, L. V., “Thermal conductivity of carbon nanotube materials: Mesoscopic modeling and scaling laws”. *2011 Material Research Society Spring Meeting and Exhibit*, San Francisco, CA, USA. April 2011.

Appendix A

A sample of the LAMMPS input script used for the simulation of thermal conductance between two-dimensional Lennard-Jones materials is provided in this appendix, to detail the general setup and computational procedure used in the series of simulations summarized in Section 5.3.2. This example script is for a simulated system of 3 Lennard-Jones materials consisting of 2 interfaces ($I = 2$).

```
# Non-equilibrium Molecular dynamics simulation of thermal conductance
# between two-dimensional Lennard-Jones materials
# Richard N. Salaway
# June 2014

##### DATA VARIABLES #####
variable R equal 6000000      # Simulation run in timesteps
variable AVG1 equal 10000    # Thermo output and averaging
                              # frequency
variable AVG2 equal 500000    # Interval for averaging
                              # temperature profile
variable rst equal 1000000    # Frequency to write restart
variable D equal 1000000      # Frequency of coordinate output

##### SIMULATION VARIABLES #####
variable flux1 equal 6.0      # Heat flow rate (Q_HB)
variable flux2 equal 3.0      # Heat flow rate (Q_HB/I)
variable sep equal 0.964992   # Separation distance
                              # between lattice planes
variable halfsep equal ${sep}/2 # Half separation distance
                              # between lattice planes

# Global setup
dimension      2
boundary       s s p
atom_style     atomic
neighbor       0.3 bin
neigh_modify   delay 5
```

```
# Create lattice and Type 1 atoms
lattice      hex 0.93
region      box block 0 40 0 99 -0.25 0.25
create_box   3 box
create_atoms 1 box
mass         * 1.0

# Change all atoms in 'slice' region to Type 2
region      slice block INF INF 50 99 INF INF
set         region slice type 2

# Duplicate all atoms in 'slice' region and set as Type 3 atoms
create_atoms 3 region slice

# Distribute initial velocities
velocity     all create 0.45 87287 rot yes mom yes

# Define default interatomic potential
pair_style   lj/cut 2.5
pair_coeff    * * 4.0 1.0

# Define interatomic potential among specific types
pair_coeff    1 2* 1.0 1.0
neigh_modify  exclude type 2 3
neigh_modify  delay 0 every 1

# Define Lennard-Jones materials based on atom type
group        TYPE1 type 1
group        TYPE2 type 2
group        TYPE3 type 3

# Define regions to be used for heat baths
region      cool block INF INF 0 9 INF INF
group       COLD region cool
region      warm block INF INF 90 99 INF INF
group       HOT region warm
group       HOT2 intersect HOT TYPE2
group       HOT3 intersect HOT TYPE3

# Output for visualization
dump MyDump all xyz $D dump.*.flux

# Define thermo output frequency
thermo ${AVG1}
```



```

##### TEMPERATURE CALCULATION AND OUTPUT #####
# These temperature computes are useful for determing steady-state
compute      TEMPALL all temp/com
compute      TEMP1 TYPE1 temp/com
compute      TEMP2 TYPE2 temp/com
compute      TEMP3 TYPE3 temp/com

# Define kinetic energy per atom for spatial profiling
compute      KE1 TYPE1 ke/atom
compute      KE2 TYPE2 ke/atom
compute      KE3 TYPE3 ke/atom

# Use fix ave/spatial for temperature profiling
fix          PROF1 TYPE1 ave/spatial 1 ${AVG2} ${AVG2} y -${halfsep} &
            ${sep} c_KE1 units box file temp1.profile
fix          PROF2 TYPE2 ave/spatial 1 ${AVG2} ${AVG2} y -${halfsep} &
            ${sep} c_KE2 units box file temp2.profile
fix          PROF3 TYPE3 ave/spatial 1 ${AVG2} ${AVG2} y -${halfsep} &
            ${sep} c_KE3 units box file temp3.profile

# Average these values over time to obtain a moving average
fix          avgTEMPALL all ave/time 1 ${AVG1} ${AVG1} c_TEMPALL
fix          avgTEMP1 TYPE1 ave/time 1 ${AVG1} ${AVG1} c_TEMP1
fix          avgTEMP2 TYPE2 ave/time 1 ${AVG1} ${AVG1} c_TEMP2
fix          avgTEMP3 TYPE3 ave/time 1 ${AVG1} ${AVG1} c_TEMP3

# Output the moving average temperatures to monitor the system
thermo_style custom step etotal ke pe f_avgTEMPALL f_avgTEMP1 &
            f_avgTEMP2 f_avgTEMP3

##### FLUX IMPLEMENTATION #####
fix          MD all nve

# Remove heat from Type 1 atoms
fix          Qout COLD heat 1 -${flux1}
# Apply heat to Type 2 atoms
fix          Qin2 HOT2 heat 1 ${flux2}
# Apply heat to Type 3 atoms
fix          Qin3 HOT3 heat 1 ${flux2}

restart      ${rst} restart.*.3GRAD
fix          SECOND all enforce2d
run          $R
write_restart restart.*.3GRAD

```

Bibliography

- [1] J. R. Lukes, H. Zhong, Thermal conductivity of individual single-wall carbon nanotubes, *J. Heat Transfer* 129 (2007) 705–716.
- [2] J. A. Thomas, R. M. Iutzi, A. J. H. McGaughey, Thermal conductivity and phonon transport in empty and water-filled carbon nanotubes, *Phys. Rev. B* 81 (2010) 045413.
- [3] J. Shiomi, S. Maruyama, Molecular dynamics of diffusive-ballistic heat conduction in single-walled carbon nanotubes, *Jpn. J. Appl. Phys.* 47 (2008) 2005–2009.
- [4] C. W. Padgett, D. W. Brenner, Influence of chemisorption on the thermal conductivity of single-wall carbon nanotubes, *Nano Lett.* 4 (2004) 1051–1053.
- [5] H. L. Zhong, J. R. Lukes, Interfacial thermal resistance between carbon nanotubes: Molecular dynamics simulations and analytical thermal modeling, *Phys. Rev. B* 74 (2006) 125403.
- [6] Z. Xu, M. J. Buehler, Nanoengineering heat transfer performance at carbon nanotube interfaces, *ACS Nano* 3 (2009) 2767–2775.
- [7] W. J. Evans, M. Shen, P. Keblinski, Inter-tube thermal conductance in carbon nanotubes arrays and bundles: Effects of contact area and pressure, *Appl. Phys. Lett.* 100 (2012) 261908.
- [8] R. S. Prasher, X. J. Hu, Y. Chalopin, N. Mingo, K. Lofgreen, S. Volz, F. Cleri, P. Keblinski, Turning carbon nanotubes from exceptional heat conductors into insulators, *Phys. Rev. Lett.* 102 (2009) 105901.
- [9] R. J. Stevens, L. V. Zhigilei, P. M. Norris, Effects of temperature and disorder on thermal boundary conductance at solidsolid interfaces: Nonequilibrium molecular dynamics simulations, *Int. J. Heat Mass Transfer* 50 (2007) 3977–3989.
- [10] C. Yu, L. Shi, Z. Yao, D. Li, A. Majumdar, Thermal conductance and thermopower of an individual single-wall carbon nanotube, *Nano Lett.* 5 (2005) 1842–1846.
- [11] M. Fujii, X. Zhang, H. Xie, H. Ago, K. Takahashi, T. Ikuta, H. Abe, T. Shimizu, Measuring the thermal conductivity of a single carbon nanotube, *Phys. Rev. Lett.* 95 (2005) 065502.

- [12] H.-Y. Chiu, V. V. Deshpande, H. W. C. Postma, C. N. Lau, C. Miko, L. Forro, M. Bockrath, Ballistic phonon thermal transport in multiwalled carbon nanotubes, *Phys. Rev. Lett.* 95 (2005) 226101.
- [13] E. Pop, D. Mann, Q. Wang, K. Goodson, H. Dai, Thermal conductance of an individual single-wall carbon nanotube above room temperature, *Nano Lett.* 6 (2006) 96–100.
- [14] S. Wang, Z. Liang, B. Wang, C. Zhang, High-strength and multifunctional macroscopic fabric of single-walled carbon nanotubes, *Adv. Mater.* 19 (2007) 1257–1261.
- [15] I.-K. Hsu, R. Kumar, A. Bushmaker, S. B. Cronin, M. T. Pettes, L. Shi, T. Brintlinger, M. S. Fuhrer, J. Cumings, Optical measurement of thermal transport in suspended carbon nanotubes, *Appl. Phys. Lett.* 92 (2008) 063119.
- [16] M. T. Pettes, L. Shi, Thermal and structural characterizations of individual single-, double-, and multi-walled carbon nanotubes, *Adv. Funct. Mater.* 19 (2009) 3918–3925.
- [17] Q. Li, C. Liu, X. Wang, S. Fan, Measuring the thermal conductivity of individual carbon nanotubes by the raman shift method, *Nanotechnology* 20 (2009) 145702.
- [18] S. Berber, Y.-K. Kwon, D. Tomanek, Unusually high thermal conductivity of carbon nanotubes, *Phys. Rev. Lett.* 84 (2000) 4613–4616.
- [19] J. Che, T. Cagin, W. A. Goddard III, Thermal conductivity of carbon nanotubes, *Nanotechnology* 11 (2000) 65–69.
- [20] M. A. Osman, D. Srivastava, Temperature dependence of the thermal conductivity of single-wall carbon nanotubes, *Nanotechnology* 12 (2001) 21–24.
- [21] S. Maruyama, A molecular dynamics simulation of heat conduction in finite length swnts, *Physica B* 323 (2002) 193–195.
- [22] S. Maruyama, A molecular dynamics simulation of heat conduction of a finite length single-walled carbon nanotube, *Microscale Thermophys. Eng.* 7 (2003) 41–50.
- [23] J. F. Moreland, J. B. Freund, G. Chen, The disparate thermal conductivity of carbon nanotubes and diamond nanowires studied by atomistic simulation, *Microscale Thermophys. Eng.* 8 (2004) 61–69.
- [24] M. Grujicic, G. Cao, B. Gersten, Atomic-scale computations of the lattice contribution to thermal conductivity of single-walled carbon nanotubes, *Materials Science and Engineering B* 107 (2004) 204–216.
- [25] M. Grujicic, G. Cao, W. N. Roy, Computational analysis of the lattice contribution to thermal conductivity of single-walled carbon nanotubes, *J. Mater. Sci.* 40 (2005) 1943–1952.

- [26] G. Zhang, B. Li, Thermal conductivity of nanotubes revisited: effects of chirality, isotope impurity, tube length, and temperature, *J. Chem. Phys.* 123 (2005) 114714.
- [27] K. Zhang, H. Fan, M. M. F. Yuen, Molecular dynamics study on thermal performance of cnt-array-thermal interface material, in: *International Symposium on Electronic Materials and Packaging*, IEEE, Kowloon, China, 2006, pp. 1–4.
- [28] K. Bi, Y. Chen, J. Yang, Y. Wang, M. Chen, Molecular dynamics simulation of thermal conductivity of single-wall carbon nanotubes, *Phys. Lett. A* 350 (2006) 150–153.
- [29] R.-Q. Pan, Z.-J. Xu, Z.-Y. Zhu, Length dependence of thermal conductivity of single-walled carbon nanotubes, *Chin. Phys. Lett.* 24 (2007) 1321–1323.
- [30] M. Alaghemandi, E. Algaer, M. C. Bohm, F. Muller-Plathe, The thermal conductivity and thermal rectification of carbon nanotubes studied using reverse non-equilibrium molecular dynamics simulations, *Nanotechnology* 20 (2009) 115704.
- [31] C. Ren, W. Zhang, Z. Xu, Z. Zhu, P. Huai, Thermal conductivity of single-walled carbon nanotubes under axial stress, *J. Phys. Chem. C* 114 (2010) 5786–5791.
- [32] B. Qiu, Y. Wang, Q. Zhao, X. Ruan, The effects of diameter and chirality on the thermal transport in free-standing and supported carbon-nanotubes, *Appl. Phys. Lett.* 100 (2012) 233105.
- [33] A. Cao, J. Qu, Size dependent thermal conductivity of single-walled carbon nanotubes, *J. Appl. Phys.* 112 (2012) 013503.
- [34] A. N. Imtani, Thermal conductivity for single-walled carbon nanotubes from einstein relation in molecular dynamics, *J. Phys. Chem. Solids* 74 (2013) 1599–1603.
- [35] J. Hone, M. C. Llaguno, N. M. Nemes, A. T. Johnson, J. E. Fischer, D. A. Walters, M. J. Casavant, J. Schmidt, R. E. Smalley, Electrical and thermal transport properties of magnetically aligned single wall carbon nanotube films, *Appl. Phys. Lett.* 77 (2000) 666–668.
- [36] J. Hone, M. C. Llaguno, M. J. Biercuk, A. T. Johnson, B. Batlogg, Z. Benes, J. E. Fischer, Thermal properties of carbon nanotubes and nanotube-based materials, *Appl. Phys. A* 74 (2002) 339–343.
- [37] S. Sinha, S. Barjami, G. Iannacchione, A. Schwab, G. Muench, Off-axis thermal properties of carbon nanotube films, *J. Nanopart. Res.* 7 (2005) 651–657.
- [38] Y. Yamada, T. Nishiyama, T. Yasuhara, K. Takahashi, Thermal boundary conductance between multi-walled carbon nanotubes, *J. Therm. Sci. Technol.* 7 (2012) 190–198.
- [39] M. E. Itkis, F. Borondics, A. Yu, R. C. Haddon, Thermal conductivity measurements of semitransparent single-walled carbon nanotube films by a bolometric technique, *Nano Letters* 7 (2007) 900–904.

- [40] I. Ivanov, A. Puretzky, G. Eres, H. Wang, Z. Pan, H. Cui, R. Jin, J. Howe, D. B. Geohegan, Fast and highly anisotropic thermal transport through vertically aligned carbon nanotube arrays, *Appl. Phys. Lett.* 89 (2006) 223110.
- [41] P. Gonnet, Z. Liang, E. S. Choi, R. S. Kadambala, C. Zhang, J. S. Brooks, B. Wang, L. Kramer, Thermal conductivity of magnetically aligned carbon nanotube buckypapers and nanocomposites, *Curr. Appl. Phys.* 6 (2006) 119 – 122.
- [42] B. A. Cola, J. Xu, C. Chang, X. Xu, T. S. Fisher, Photoacoustic characterization of carbon nanotube array thermal interfaces, *J. Appl. Phys.* 101 (2007) 054313.
- [43] J. Yang, S. Waltermire, Y. Chen, A. A. Zinn, T. T. Xu, D. Li, Contact thermal resistance between individual multiwall carbon nanotubes, *Appl. Phys. Lett.* 96 (2010) 023109.
- [44] S. Maruyama, Y. Igarashi, Y. Taniguchi, J. Shiomi, Anisotropic heat transfer of single-walled carbon nanotubes, *J. Therm. Sci. Technol.* 1 (2006) 138–148.
- [45] V. Varshney, S. S. Patnaik, A. K. Roy, B. L. Farmer, Modeling of thermal conductance at transverse cnt-cnt interfaces, *J. Phys. Chem. C* 114 (2010) 16223.
- [46] Y. Chalopin, S. Volz, N. Mingo, Upper bound to the thermal conductivity of carbon nanotube pellets, *J. Appl. Phys.* 105 (2009) 084301.
- [47] A. N. Volkov, L. V. Zhigilei, Heat conduction in carbon nanotube materials: Strong effect of intrinsic thermal conductivity of carbon nanotubes, *Appl. Phys. Lett.* 101 (2012) 043113.
- [48] A. Thess, R. Lee, P. Nikolaev, H. Dai, P. Petit, J. Robert, C. Xu, Y. H. Lee, S. G. Kim, A. G. Rinzler, G. E. Colbert, Daniel T. and Scuseria, D. Tomanek, J. E. Fischer, R. E. Smalley, Crystalline ropes of metallic carbon nanotubes, *Science* 273 (1996) 483–487.
- [49] A. G. Rinzler, J. Liu, H. Dai, P. Nikolaev, C. B. Huffman, F. J. Rodriguez-Macias, P. J. Boul, A. H. Lu, D. Heymann, D. T. Colbert, R. S. Lee, J. Fischer, A. M. Rao, P. C. Eklund, R. E. Smalley, Large-scale purification of single-wall carbon nanotubes: Process, product, and characterization, *Appl. Phys. A* 67 (1998) 29–37.
- [50] W. Ma, L. Song, R. Yang, T. Zhang, Y. Zhao, L. Sun, Y. Ren, D. Liu, L. Liu, J. Shen, Z. Zhang, Y. Xiang, W. Zhou, S. Xie, Directly synthesized strong, highly conducting, transparent single-walled carbon nanotube films, *Nano Lett.* 7 (2007) 2307–2311.
- [51] F. Hennrich, S. Lebedkina, S. Malika, J. Tracy, M. Barczewski, H. Rosner, M. Kappes, Preparation, characterization and applications of free-standing single walled carbon nanotube thin films, *Phys. Chem. Chem. Phys.* 11 (2002) 2273–2277.

- [52] H. Chen, M. Chen, J. Di, G. Xu, H. Li, Q. Li, Architecting three-dimensional networks in carbon nanotube buckypapers for thermal interface materials, *J. Phys. Chem. C* 116 (2012) 3903–3909.
- [53] L. Shi, D. Y. Li, C. H. Yu, W. Y. Jang, D. Kim, Z. Yao, P. Kim, A. Majumdar, Measuring thermal and thermoelectric properties of one-dimensional nanostructures using a microfabricated device, *J. Heat Transfer* 125 (2003) 881–888.
- [54] A. Aliev, M. Lima, E. Silverman, R. Baughman, Thermal conductivity of multi-walled carbon nanotube sheets: radiation losses and quenching of phonon modes, *Nanotechnology* 21 (2010) 035709.
- [55] W. Lin, J. Shang, W. Gu, C. Wong, Parametric study of intrinsic thermal transport in vertically multi-walled carbon nanotubes using a laser flash technique, *Carbon* 50 (2012) 1591–1603.
- [56] T.-Y. Choi, D. Poulikakos, J. Tharian, U. Sennhauser, Measurement of the thermal conductivity of individual carbon nanotubes by the four-point three-w method, *Nano Lett.* 6 (2006) 1589–1593.
- [57] V. Datsyuk, I. Firkowska, K. Gharagozloo-Hubmann, M. Lisunova, A. Vogt, A. Boden, M. Kasimir, S. Trotsenko, G. Czempel, S. Reich, Carbon nanotubes based engineering materials for thermal management applications, in: 2011 27th Annual Semiconductor Thermal Measurement and Management Symposium (SEMI-THERM), IEEE, San Jose, CA, USA, 2011, pp. 325–332.
- [58] K. Kordas, G. Toth, P. Moilanen, M. Kumpumaki, J. Vahakangas, A. Uusimaki, R. Vajtai, P. M. Ajayan, Chip cooling with integrated carbon nanotube microfin architectures, *Appl. Phys. Lett.* 90 (2007) 123105.
- [59] L. Ekstrand, Z. Mo, Y. Zhang, J. Liu, Modelling of carbon nanotubes as heat sink fins in microchannels for microelectronics cooling, in: Polytronic 2005 - 5th International Conference on Polymers and Adhesives in Microelectronics and Photonics, IEEE, Wroclaw, Poland, 2005, pp. 185–187.
- [60] T. Iwai, Y. Awano, Carbon nanotube bumps for thermal and electric conduction in transistor, *FUJITSU Sci. Tech. J.* 43 (2007) 508–515.
- [61] Y. Xu, C.-K. Leong, D. Chung, Carbon nanotube thermal pastes for improving thermal contacts, *J. Electron. Mater.* 36 (2007) 1181–1187.
- [62] H. Huang, C. H. Liu, Y. Wu, S. Fan, Aligned carbon nanotube composite films for thermal management, *Adv. Mater.* 17 (2005) 1652–1656.
- [63] Y. Wu, C. H. Liu, H. Huang, S. S. Fan, Effects of surface metal layer on the thermal contact resistance of carbon nanotube arrays, *Appl. Phys. Lett.* 87 (2005) 213108.

- [64] T. Tong, Y. Zhao, L. Delzeit, A. Kashani, M. Meyyappan, A. Majumdar, Dense vertically aligned multiwalled carbon nanotube arrays as thermal interface materials, *IEEE Trans. Compon. Packag. Technol.* 30 (2007) 92–100.
- [65] X. Liu, Y. Zhang, A. M. Cassell, B. A. Cruden, Implications of catalyst control for carbon nanotube based thermal interface materials, *J. Appl. Phys.* 104 (2008) 084310.
- [66] A. A. Balandin, Thermal properties of graphene and nanostructured carbon materials, *Nat. Mater.* 10 (2011) 569–581.
- [67] R. Prasher, Thermal interface materials: Historical perspective, status, and future directions, *Proceedings of the IEEE* 94 (2006) 1571–1586.
- [68] K. Zhang, M. Yuen, N. Wang, J. MIAO, D. Xiao, H. Fan, Thermal interface material with aligned CNT and its application in HB-LED packaging, in: 2006 IEEE Electronic Components and Technology Conference, IEEE, San Diego, CA, USA, 2006, pp. 177–182.
- [69] L. Xu, N. Wei, Y. Zheng, Z. Fan, H.-Q. Wang, J.-C. Zheng, Graphene-nanotube 3D networks: Intriguing thermal and mechanical properties, *J. Mater. Chem.* 22 (2012) 1435–1444.
- [70] M. P. Gupta, L. Chen, D. Estrada, A. Behnam, E. Pop, S. Kumar, Impact of thermal boundary conductances on power dissipation and electrical breakdown of carbon nanotube network transistors, *J. Appl. Phys.* 112 (2012) 124506.
- [71] T. Kashiwagi, E. Grulke, J. Hilding, K. Groth, R. Harris, K. Butler, J. Shields, S. Kharchenko, J. Douglas, Thermal and flammability properties of polypropylene/carbon nanotube nanocomposites, *Polymer* 45 (2004) 4227 – 4239.
- [72] R. A. Shelly, K. Toprak, Y. Bayazitoglu, Nosehoover thermostat length effect on thermal conductivity of single wall carbon nanotubes, *Int. J. Heat Mass Transfer* 53 (2010) 5884–5887.
- [73] M. C. H. Wu, J.-Y. Hsu, Thermal conductivity of carbon nanotubes with quantum correction via heat capacity, *Nanotechnology* 20 (2009) 145401.
- [74] H. Zhong, J. R. Lukes, Thermal conductivity of single-wall carbon nanotubes, in: *Proc. IMECE04, Electronic and Photonic Packaging, Electrical Systems Design and Photonics, and Nanotechnology*, ASME, Anaheim, CA, USA, 2004, pp. 65–73.
- [75] D.-L. Feng, Y.-H. Feng, Y. Chen, W. Li, X.-X. Zhang, Effects of doping, stone-wales and vacancy defects on thermal conductivity of single-wall carbon nanotubes, *Chin. Phys. B.* 22 (2013) 016501.
- [76] A. N. Volkov, R. N. Salaway, L. V. Zhigilei, Atomistic simulations, mesoscopic modeling, and theoretical analysis of thermal conductivity of bundles composed of carbon nanotubes, *J. Appl. Phys.* 114 (2013) 104301.

- [77] R.-Q. Pan, Diameter and temperature dependence of thermal conductivity of single-walled carbon nanotubes, *Chin. Phys. Lett.* 28 (2011) 066104.
- [78] Z. Xu, M. J. Buehler, Strain controlled thermomutability of single-walled carbon nanotubes, *Nanotechnology* 20 (2009) 185701.
- [79] N. Wei, L. Xu, H.-Q. Wang, J.-C. Zheng, Strain engineering of thermal conductivity in graphene sheets and nanoribbons: A demonstration of magic flexibility, *Nanotechnology* 22 (2011) 105705.
- [80] F. Nishimura, T. Takahashi, K. Watanabe, T. Yamamoto, Bending robustness of thermal conductance of carbon nanotubes: Nonequilibrium molecular dynamics simulation, *Appl. Phys. Express* 2 (2009) 035003.
- [81] Z. Xu, M. J. Buehler, Hierarchical nanostructures are crucial to mitigate ultrasmall thermal point loads, *Nano Lett.* 9 (2009) 2065–2072.
- [82] C. Lin, H. Wang, W. Yang, The thermomutability of single-walled carbon nanotubes by constrained mechanical folding, *Nanotechnology* 21 (2010) 365708.
- [83] A. N. Volkov, T. Shiga, D. Nicholson, J. Shiomi, L. V. Zhigilei, Effect of bending buckling of carbon nanotubes on thermal conductivity of carbon nanotube materials, *J. Appl. Phys.* 111 (2012) 053501.
- [84] J. E. Jones, On the determination of molecular fields. II. From the equation of state of a gas, *Proc. R. Soc. Lon. Ser-A* 106 (1924) 463–477.
- [85] D. Yin, A. D. MacKerell, Combined ab initio/empirical approach for optimization of Lennard-Jones parameters, *J. Comput. Chem.* 19 (1998) 334–348.
- [86] L. Verlet, Computer “experiments” on classical fluids. I. Thermodynamical properties of Lennard-Jones molecules, *Phys. Rev.* 159 (1967) 98–103.
- [87] M. Kaukonen, A. Gulans, P. Havu, E. Kauppinen, Lennard-Jones parameters for small diameter carbon nanotubes and water for molecular mechanics simulations from van der Waals density functional calculations, *J. Comput. Chem.* 33 (2012) 652–658.
- [88] J. Duda, T. English, E. Piekos, T. Beechem, T. Kenny, Bidirectionally tuning kapitza conductance through the inclusion of substitutional impurities, *J. Appl. Phys.* 112 (2012) 073519.
- [89] L. A. Girifalco, M. Hodak, R. S. Lee, Carbon nanotubes, buckyballs, ropes, and a universal graphitic potential, *Phys. Rev. B* 62 (2000) 13104–13110.
- [90] M. Hodak, L. Girifalco, Cohesive properties of fullerene-filled nanotube ropes, *Chem. Phys. Lett.* 363 (2002) 93–98.
- [91] R. Prasher, Acoustic mismatch model for thermal contact resistance of van der waals contacts, *Appl. Phys. Lett.* 94 (2009) 3075065.

- [92] W. J. Evans, P. Keblinski, Thermal conductivity of carbon nanotube cross-bar structures, *Nanotechnology* 21 (2010) 475704.
- [93] M. L. Falk, Molecular-dynamics study of ductile and brittle fracture in model non-crystalline solids, *Phys. Rev. B* 60 (1999) 7062–7070.
- [94] A. J. H. McGaughey, M. I. Hussein, E. S. Landry, M. Kaviani, G. M. Hulbert, Phonon band structure and thermal transport correlation in a layered diatomic crystal, *Phys. Rev. B* 74 (2006) 104304.
- [95] J. C. Duda, T. S. English, D. A. Jordan, P. M. Norris, W. A. Soffa, Reducing thermal conductivity of binary alloys below the alloy limit via chemical ordering, *J. Phys.: Condens. Matter* 23 (2011) 205401.
- [96] M. B. Sweatman, Weighted density-functional theory for simple fluids: Prewetting of a Lennard-Jones fluid, *Phys. Rev. E* 65 (2001) 011102.
- [97] E. S. Landry, M. I. Hussein, A. J. H. McGaughey, Complex superlattice unit cell designs for reduced thermal conductivity, *Phys. Rev. B* 77 (2008) 184302.
- [98] F. Turci, T. Schilling, M. Yamani, M. Oettel, Solid phase properties and crystallization in simple model systems, *Eur. Phys. J. Special Topics* 223 (2014) 421–438.
- [99] J. Tersoff, New empirical approach for the structure and energy of covalent systems, *Phys. Rev. B* 37 (1988) 6991–7000.
- [100] J. Tersoff, Empirical interatomic potential for carbon, with applications to amorphous carbon, *Phys. Rev. Lett.* 61 (1988) 2879–2882.
- [101] G. C. Abell, Empirical chemical pseudopotential theory of molecular and metallic bonding, *Phys. Rev. B* 31 (1985) 6184–6196.
- [102] D. W. Brenner, Empirical potential for hydrocarbons for use in simulating the chemical vapor deposition of diamond films, *Phys. Rev. B* 42 (1990) 9458–9471.
- [103] D. W. Brenner, O. A. Shenderova, J. A. Harrison, S. J. Stuart, B. Ni, S. B. Sinnott, A second-generation reactive empirical bond order (rebo) potential energy expression for hydrocarbons, *J. Phys.: Condens. Matter* 14 (2002) 783–802.
- [104] V. K. Tewary, B. Yang, Parametric interatomic potential for graphene, *Phys. Rev. B* 79 (2009) 075442.
- [105] L. Lindsay, D. A. Broido, Optimized tersoff and brenner empirical potential parameters for lattice dynamics and phonon thermal transport in carbon nanotubes and graphene, *Phys. Rev. B* 81 (2010) 205441.
- [106] S. Kumar, J. Y. Murthy, Interfacial thermal transport between nanotubes, *J. Appl. Phys.* 106 (2009) 084302.

- [107] S. Plimpton, Fast parallel algorithms for short-range molecular dynamics, *J. Comput. Phys.* 117 (1995) 1–19.
- [108] W. M. Brown, P. Wang, S. J. Plimpton, A. N. Tharrington, Implementing molecular dynamics on hybrid high performance computers - short range forces, *Comput. Phys. Commun.* 182 (2011) 898 – 911.
- [109] J. Shiomi, private communication, 2010.
- [110] A. M. Marconnet, M. A. Panzer, K. E. Goodson, Thermal conduction phenomena in carbon nanotubes and related nanostructured materials, *Rev. Mod. Phys.* 85 (2013) 1295–1326.
- [111] S. J. Stuart, A. B. Tutein, J. A. Harrison, A reactive potential for hydrocarbons with intermolecular interactions, *J. Chem. Phys.* 112 (2000) 6472–6486.
- [112] W. Zhang, Z. Zhu, F. Wang, T. Wang, L. Sun, Z. Wang, Chirality dependence of the thermal conductivity of carbon nanotubes, *Nanotechnology* 15 (2004) 936–939.
- [113] Y. Yamaguchi, S. Maruyama, A molecular dynamics simulation of the fullerene formation process, *Chem. Phys. Lett.* 286 (1998) 336–342.
- [114] J. Zhang, M. Tanaka, T. Matsumoto, A simplified approach for heat conduction analysis of CNT-based nano-composites, *Comput. Methods Appl. Mech. Engrg.* 193 (2004) 5597–5609.
- [115] C. Ren, Z. Xu, W. Zhang, Y. Li, Z. Zhu, P. Huai, Theoretical study of heat conduction in carbon nanotube hetero-junctions, *Phys. Lett. A* 374 (2010) 1860–1865.
- [116] J. B. Hou, X. W. Wang, P. Vellelacheruvu, J. Q. Guo, C. Liu, H. M. Cheng, Thermal characterization of single-wall carbon nanotube bundles using the self-heating 3 omega technique, *J. Appl. Phys.* 100 (2006) 124314.
- [117] X. Huang, J. Wang, G. Eres, X. Wang, Thermophysical properties of multi-wall carbon nanotube bundles at elevated temperatures up to 830 K, *Carbon* 49 (2011) 1680–1691.
- [118] P. Kim, L. Shi, A. Majumdar, P. McEuen, Thermal transport measurements of individual multiwalled nanotubes, *Phys. Rev. Lett.* 87 (2001) 215502.
- [119] I.-K. Hsu, M. T. Pettes, A. Bushmaker, M. Aykol, L. Shi, S. B. Cronin, Optical absorption and thermal transport of individual suspended carbon nanotube bundles, *Nano Lett.* 9 (2009) 590–594.
- [120] I.-K. Hsu, M. T. Pettes, M. Aykol, C. C. Chang, W. H. Hung, J. Theiss, L. Shi, S. B. Cronin, Direct observation of heat dissipation in individual suspended carbon nanotubes using a two-laser technique, *J. Appl. Phys.* 110 (2011) 044328.

- [121] J. Yang, Y. Yang, S. Waltermire, X. Wu, H. Zhang, T. Gutu, Y. Jiang, Y. Chen, A. A. Zinn, R. Prasher, T. Xu, D. Li, Enhanced and switchable nanoscale thermal conduction due to van der Waals interfaces, *Nat. Nanotechnol.* 7 (2012) 91–95.
- [122] X. H. Yan, Y. Xiao, Z. M. Li, Effects of intertube coupling and tube chirality on thermal transport of carbon nanotubes, *J. Appl. Phys.* 99 (2006) 124305.
- [123] T. Schneider, E. Stoll, Molecular-dynamics study of a three-dimensional one-component model for distortive phase transitions, *Phys. Rev. B* 17 (1978) 1302–1322.
- [124] H.-C. Cheng, C.-H. Wu, W.-H. Chen, Low-temperature thermal conductivity of short single-walled carbon nanotubes using a modified nose-hoover thermostat, *Nanoscale Microscale Thermophys. Eng.* 16 (2012) 242–259.
- [125] A. V. Savin, B. Hu, Y. S. Kivshar, Thermal conductivity of single-walled carbon nanotubes, *Phys. Rev. B* 80 (2009) 195423.
- [126] J. Wang, J.-S. Wang, Carbon nanotube thermal transport: Ballistic to diffusive, *Appl. Phys. Lett.* 88 (2006) 111909.
- [127] D. Donadio, G. Galli, Thermal conductivity of isolated and interacting carbon nanotubes: Comparing results from molecular dynamics and the boltzmann transport equation, *Phys. Rev. Lett.* 99 (2007) 255502.
- [128] N. Mingo, D. A. Broido, Length dependence of carbon nanotube thermal conductivity and the “problem of long waves”, *Nano Lett.* 5 (2005) 1221–1225.
- [129] N. Mingo, D. A. Broido, Carbon nanotube ballistic thermal conductance and its limits, *Phys. Rev. Lett.* 95 (2005) 096105.
- [130] H.-Y. Cao, H. Xiang, X.-G. Gong, Unexpected large thermal rectification in asymmetric grain boundary of graphene, *Solid State Commun.* 152 (2012) 1807 – 1810.
- [131] J. E. Turney, E. S. Landry, A. J. H. McGaughey, C. H. Amon, Predicting phonon properties and thermal conductivity from anharmonic lattice dynamics calculations and molecular dynamics simulations, *Phys. Rev. B* 79 (2009) 064301.
- [132] D. P. Sellan, E. S. Landry, J. E. Turney, A. J. H. McGaughey, C. H. Amon, Size effects in molecular dynamics thermal conductivity predictions, *Phys. Rev. B* 81 (2010) 214305.
- [133] Z. Yao, J.-S. Wang, B. Li, G.-R. Liu, Thermal conduction of carbon nanotubes using molecular dynamics, *Phys. Rev. B* 71 (2005) 085417.
- [134] P. K. Schelling, S. R. Phillpot, P. Keblinski, Comparison of atomic-level simulation methods for computing thermal conductivity, *Phys. Rev. B* 65 (2002) 144306.

- [135] T. Watanabe, S. B. Sinnott, J. S. Tulenko, R. W. Grimes, P. K. Schelling, S. R. Phillpot, Thermal transport properties of uranium dioxide by molecular dynamics simulations, *J. Nucl. Mater.* 375 (2008) 388–396.
- [136] X. Ni, G. Zhang, B. Li, Thermal conductivity and thermal rectification in unzipped carbon nanotubes, *J. Phys.: Condens. Matter* 23 (2011) 215301.
- [137] J.-W. Jiang, J. Chen, J.-S. Wang, B. Li, Edge states induce boundary temperature jump in molecular dynamics simulation of heat conduction, *Phys. Rev. B* 80 (2009) 052301.
- [138] D. J. Evans, Homogeneous NEMD algorithm for thermal conductivity - Application of non-canonical linear response theory, *Phys. Lett. A* 91 (1982) 457–460.
- [139] M. S. Dresselhaus, P. C. Eklund, Phonons in carbon nanotubes, *Adv. Phys.* 49 (2000) 705–814.
- [140] S. Shenogin, L. Xue, R. Ozisik, P. Keblinski, Role of thermal boundary resistance on the heat flow in carbon-nanotube composites, *J. Appl. Phys.* 95 (2004) 8136–8144.
- [141] S. Huxtable, D. Cahill, S. a. Shenogin, Interfacial heat flow in carbon nanotube suspensions, *Nat. Mater.* 2 (2003) 731–734.
- [142] C. F. Carlborg, J. Shiomi, S. Maruyama, Thermal boundary resistance between single-walled carbon nanotubes and surrounding matrices, *Phys. Rev. B* 78 (2008) 205406.
- [143] P. Keblinski, F. Cleri, Contact resistance in percolating networks, *Phys. Rev. B* 69 (2004) 184201.
- [144] E. Pop, D. A. Mann, K. E. Goodson, H. Dai, Electrical and thermal transport in metallic single-wall carbon nanotubes on insulating substrates, *J. Appl. Phys.* 101 (2007) 093710.
- [145] R. N. Salaway, L. V. Zhigilei, Molecular dynamics simulations of thermal conductivity of carbon nanotubes: Resolving the effects of computational parameters, *Int. J. Heat Mass Transfer* 70 (2014) 954 – 964.
- [146] Y. Wang, P. Keblinski, Role of wetting and nanoscale roughness on thermal conductance at liquid-solid interface, *Appl. Phys. Lett.* 99 (2011) 073112.
- [147] J. C. Duda, T. S. English, E. S. Piekos, W. A. Soffa, L. V. Zhigilei, P. E. Hopkins, Implications of cross-species interactions on the temperature dependence of kapitza conductance, *Phys. Rev. B* 84 (2011) 193301.
- [148] Z.-Y. Ong, E. Pop, Molecular dynamics simulation of thermal boundary conductance between carbon nanotubes and SiO₂, *Phys. Rev. B* 81 (2010) 155408.

- [149] M. Hu, P. Keblinski, P. K. Schelling, Kapitza conductance of siliconamorphous polyethylene interfaces by molecular dynamics simulations, *Phys. Rev. B* 79 (2009) 104305.
- [150] P. D. Welch, The use of fast fourier transform for the estimation of power spectra: A method based on time averaging over short, modified periodograms, *IEEE Trans. Audio Electroacoust.* 15 (1967) 70–73.
- [151] T. English, J. Duda, J. Smoyer, D. Jordan, P. Norris, L. Zhigilei, Enhancing and tuning phonon transport at vibrationally mismatched solid-solid interfaces, *Phys. Rev. B* 85 (2012) 035438.
- [152] H. Zhu, Y. Xu, B.-L. Gu, W. Duan, Robust linear dependence of thermal conductance on radial strain in carbon nanotubes, *New J. Phys.* 14 (2012) 013053.
- [153] M. Shen, W. J. Evans, D. Cahill, P. Keblinski, Bonding and pressure-tunable interfacial thermal conductance, *Phys. Rev. B* 84 (2011) 195432.